

PROJECT INFORMATION

1. What constitutes a project?

Any combination of analytical, numerical, and experimental investigations into a nonlinear system can be selected to be a part of the project. The investigations can be tailored to carry out one or more of the following: a) uncover nonlinear phenomena and/or explain observed nonlinear phenomena, b) analyze stability of motions in detail (for example, stability analyses of equilibrium and/or periodic motions of the considered nonlinear system, c) catalog nonlinear characteristics and nonlinear behavior of the considered nonlinear system for different parameter ranges, d) go beyond what is covered in the classroom and understand a topic in more depth (for example, global analyses, dimension calculations, quasiperiodic motions, time series analyses), and e) develop a simplified reduced-order model (a map or a set of ODEs) of a complex system that captures same physics as that observed in experiments.

2. What are some possible project topics?

A partial list of examples includes the following: i) experimental investigations into nonlinear oscillations of mechanical, electrical, or structural systems, ii) study of instabilities in micro-scale and nano-scale systems, iii) study of bifurcations of solutions of nonsmooth systems (such as systems with friction and impact), and iv) study of phenomena such as solitons, chatter, and so forth.

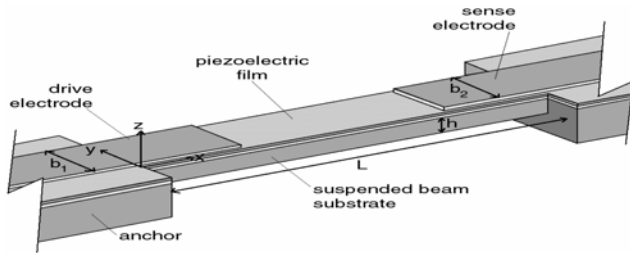
3. What should the project report have in it?

The essential elements of the project report include an introduction to the problem studied, problem description, study undertaken, results obtained, conclusions/inferences from the study, and a list of references.

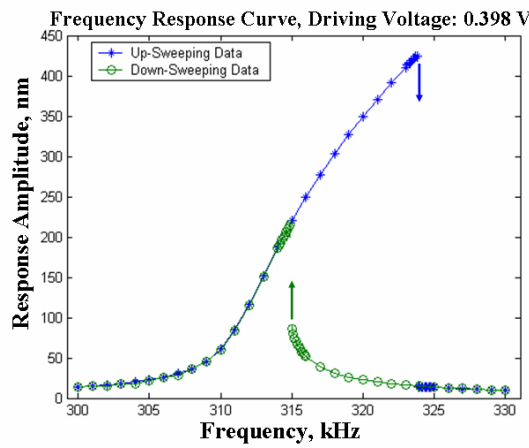
4. Project Description Due Date: March 28, 2017 Final Project Report Due Date: May 9, 2017

5. Representative final reports and project descriptions from the previous years are included in the following pages.

Through studying identified parameter trends of a piezoelectric micro-scale resonator, it would appear that additional terms may be



necessary to describe the behavior of this device. Within this project, I intend to explore a number of possible terms that may be added to the Duffing oscillator equation currently

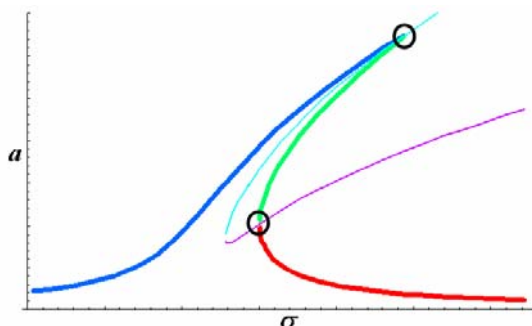


being used to model the frequency-response behavior of the resonators. Additional terms that will be examined include a quadratic term, higher order damping terms, and addition higher order stiffness terms. Following the addition of these different terms, the approximate response of the system

to a sinusoidal excitation will be determined using perturbation methods. Frequency-amplitude relationships will be examined as well as the stability of the system's fixed points. As the new frequency-response equations are derived, the influence of each of the

parameters on the structure of the frequency-response curve will be examined.

If a revised model can be derived that appears to explain some of the parameter trends previously observed, preliminary



parametric identification will be conducted using frequency-response data previously gathered from a PZT micro-scale resonator.

Nonlinear Oscillations of Piezoelectric Micro-Scale Resonators with Aerodynamic Damping

Andrew Dick
Department of Mechanical Engineering,
University of Maryland
College Park, Maryland, USA

Abstract:

Within the paper, the nonlinear dynamic behavior of piezoelectric micro-scale resonators is examined. Based on previous work done modeling the dynamics of these devices, aerodynamic damping may play a significant role in the system's behavior. A model is developed by adding this dissipative term to an existing model. The newly defined system is thoroughly studied and an approximate solution is obtained. A previously existing parametric identification scheme, modified to include the new term, is used to analyze frequency-response data collected from the micro-scale resonators.

Introduction:

Piezoelectric micro-scale resonators are currently being developed to serve as filters for communication and signal processing applications [DeVoe, 2001]. The resonators examined within this study utilize the piezoelectric material lead zirconate titanate (PZT) to both drive and sense the motion of the resonator. Figure 1 shows the structure of the devices studied in this work.

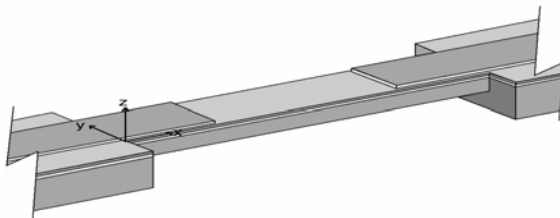


Figure 1: Structure of piezoelectric micro-scale clamped-clamped beam resonator.

The signal to be filtered is applied across the piezoelectric material producing an electric field to actuate the resonator. The deformation at the other end of the resonator results in a strain within the piezoelectric material that produces an output current. Using MicroElectroMechanical Systems (MEMS) fabrication technology, these devices are manufactured with dimensions of $200 \mu\text{m} \times 20 \mu\text{m} \times 2 \mu\text{m}$. As a result, the effective amount of damping is extremely small. This enables MEMS devices to experience nonlinear behavior that equivalent macro-scale devices would not. This study investigates the presences and affect of aerodynamic damping on the nonlinear behavior as seen in Figure 2.

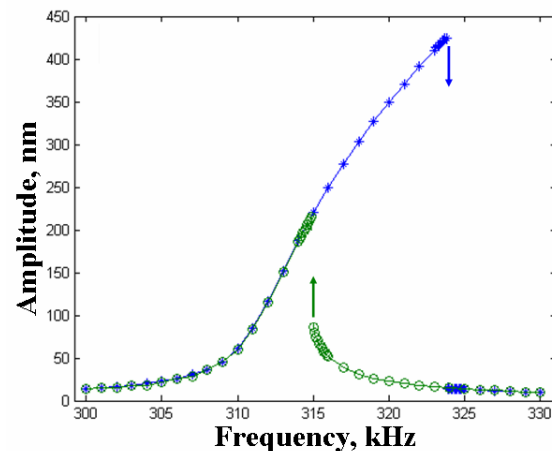


Figure 2: Experimental frequency-response of piezoelectric micro-scale resonator.

To study the presence of this type of damping, a nonlinear Euler-Bernoulli beam model is proposed to model the dynamic behavior of the piezoelectric micro-scale resonators. Using a single-mode approximation, the Galerkin procedure is used to reduce the partial differential equation into an ordinary differential equation of the displacement at a single point with respect to time. With this equation, a linear stability analysis is conducted on the unforced system as well as a stability analysis using a Lyapunov function [Nayfeh & Balachandran, 1995]. The dynamic behavior of the full forced system is examined to gain some insight into the influence of each the parameters. Following these studies, the method of multiple scales is applied to obtain a first order approximation of the solution to this system. The modulation equations from this perturbation method are used to produce a frequency-response equation and an equation for the critical points is acquired from a stability analysis. These equations are then used to modify a parametric identification scheme which is applied to experimental data. The results of this parametric identification study reveal how well the aerodynamic damping term describes the behavior of the system.

System Model:

Since the length to width ratio of these devices is about ten to one, they are represented using an Euler-Bernoulli beam model [Preidikman, et al., 2003]. This equation consists of an inertial term, a bending stiffness term, a stiffness term caused by an axial force, a stiffness term cause by axial stretching, a viscous damping term, an aerodynamic damping term, and the excitation term caused by a distributed moment. This equation is presented as equation (1.1).

$$\begin{aligned}
& \rho A_n \frac{\partial^2 W_n(x,t)}{\partial t^2} + EI_n \frac{\partial^4 W_n(x,t)}{\partial x^4} \\
& + P_{0,n} \frac{\partial^2 W_n(x,t)}{\partial x^2} \\
& + \left(\frac{EA_n}{2L} \int_0^L \left(\frac{\partial W_n(\hat{x},t)}{\partial x} \right)^2 d\hat{x} \right) \frac{\partial^2 W_n(x,t)}{\partial x^2} \\
& + c_{1,n} \frac{\partial W_n(x,t)}{\partial t} \\
& + c_{2,n} \frac{\partial W_n(x,t)}{\partial t} \left| \frac{\partial W_n(x,t)}{\partial t} \right| \\
& = M_0 \cos(\omega t) \frac{d^2}{dx^2} (u(x) - u(x-x_1))
\end{aligned} \tag{1.1}$$

Within this equation, ρ is the density of the material, A is the cross-sectional area, E is the Young's modulus, I is the moment of inertia, P is the axial force, L is the length, W is the transverse deflection, x is the position along the length and t represents time. The subscript n in this equation corresponds to the three section of the resonator differentiated by the presence or absence of the top electrode layer. Because the resonators are composite structures, the Euler Method must be used to determine the effective parameter values. The parameter c_1 is the viscous damping coefficient, the parameter c_2 is the aerodynamic damping coefficient, and M_0 is the magnitude of the distributed moment produced by the excited portion of the piezoelectric material. Clamped-clamped beam boundary conditions are employed.

To study this system, it is necessary to simplify this partial differential equation into an ordinary differential equation. Using a single-mode approximation, the transverse deflection of the resonator is separated into the product of the mode shape and the deflection at the center of the resonator as a function of time. With the aid of the

Galerkin procedure, the position dependence of the equation is removed. This new equation is shown as equation (1.2) with the variables defined in equations (1.3) through (1.8). Within equation (1.2), z is a function of time and the overdot symbol indicates a derivative with respect to time.

$$\begin{aligned} \bar{m}\ddot{z}(t) + \bar{c}_1\dot{z}(t) + k z(t) \\ + \bar{c}_2\dot{z}(t)|\dot{z}(t)| + \alpha_3 z^3(t) = F \cos(\omega t) \end{aligned} \quad (1.2)$$

$$\bar{m} = \rho A_n \int_0^L \phi^2(x) dx \quad (1.3)$$

$$\bar{c}_1 = c_{1,n} \int_0^L \phi^2(x) dx \quad (1.4)$$

$$k = \int_0^L (EI_n \phi^{(4)}(x) + P_{0,n} \phi''(x)) \phi(x) dx \quad (1.5)$$

$$\bar{c}_2 = c_{2,n} \int_0^L \phi^3(x) dx \quad (1.6)$$

$$\begin{aligned} \alpha_3 = \int_0^L (EI_n \phi^{(4)}(x)) \phi(x) dx \\ + \int_0^L (P_{0,n} \phi''(x)) \phi(x) dx \end{aligned} \quad (1.7)$$

$$F = M_0 \int_0^L \left(\frac{d^2}{dx^2} \begin{pmatrix} u(x) \\ -u(x-x_1) \end{pmatrix} \right) \phi(x) dx \quad (1.8)$$

In order for these parameters to be calculated, an equation for the mode shape of the resonator must be obtained. Because it can not be obtained from the nonlinear differential equation, a linear approximation of the mode shape is used. The linear approximation is determined by removing the nonlinear term, damping terms, and excitation. Assuming harmonic oscillations, the mode shape and natural frequency of the linearized model are determined. The mode shape and amount of axial force are determined by matching the natural

frequency with what is observed in experimental data.

In order to simplify the differential equation, it was redefined with new variables and a nondimensional time. This enabled the equation to be normalized with respect to the natural frequency of the resonator. The new equation is listed as equation (1.9). The new variables are defined by equations (1.10) through (1.15). Within equation (1.9), u is a function of the nondimensional time, τ , and the prime symbol indicates a derivative with respect to this nondimensional time.

$$\begin{aligned} u'' + 2\mu_1 u' + u + \mu_2 u' |u'| + \alpha u^3 \\ = 2K \cos(\Omega \tau) \end{aligned} \quad (1.9)$$

$$\tau = \omega_n t \quad (1.10)$$

$$\Omega \approx \frac{\omega}{\omega_n} \quad (1.11)$$

$$\mu_1 = \frac{\bar{c}_1}{2\bar{m}\omega_n} \quad (1.12)$$

$$\mu_2 = \frac{\bar{c}_2}{\bar{m}} \quad (1.13)$$

$$\alpha = \frac{\alpha_3}{k} \quad (1.14)$$

$$K = \frac{F}{2k} \quad (1.15)$$

Equation (1.9) was then analyzed to study the stability of the unforced system and the dynamic behavior of the system.

System Analyses:

The first analysis performed on the system was a linear stability analysis of the fixed point of the unforced system. This was done by separating the differential equation into two first-order differential equations shown as equation (1.16) and (1.17). The system's fixed point is located at the origin. The Jacobian matrix is

calculated from these equations and the eigenvalues are determined. The Jacobian matrix and eigenvalue function are shown as equation (1.18) and equation (1.19), respectively.

$$u'_1(\tau) = u_2(\tau) \quad (1.16)$$

$$\begin{aligned} u'_2(\tau) &= -u_1(\tau) - 2\mu_1 u_2(\tau) \\ &\quad - \mu_2 u_2(\tau) |u_2(\tau)| - \alpha u_1^3(\tau) \end{aligned} \quad (1.17)$$

$$\left[D_U F \Big|_{(0,0)} \right] = \begin{bmatrix} 0 & 1 \\ -1 & -2\mu_1 \end{bmatrix} \quad (1.18)$$

$$\lambda_{1,2} = -\mu_1 \pm \sqrt{\mu_1^2 - 1} \quad (1.19)$$

Because the damping of the system is assumed to be very small, the equation for the eigenvalues can be rewritten as equation (1.20). This indicates that the eigenvalues are a complex conjugate pairs. The values of the eigenvalues of this system are shown in Figure 3 as a function of the linear damping parameter μ_1 . As the value of μ_1 increases from zero, the fixed point changes from a center to a stable spiral. After the value of μ_1 has increased beyond one, the fixed point becomes a stable node.

$$\lambda_{1,2} = -\mu_1 \pm i\sqrt{1-\mu_1^2} \quad (1.20)$$

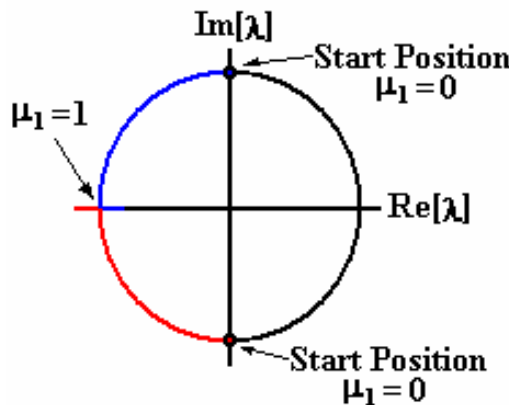


Figure 3: Eigenvalues from linear analysis.

Due to the linearization, the effects of the nonlinear terms are not accounted for within this analysis. As a result, the stability of this fixed point can not accurately be determined using this linear analysis.

In order to gain information concerning the stability of the fixed point of the nonlinear system, a stability analysis is conducted using a Lyapunov function. For this system, a Lyapunov function is designed that will expedite the analysis. The Lyapunov function is greater than zero for all state values not equal to the fixed point and it is equal to zero at the fixed point. This function is shown as equation (1.21).

$$V(u_1, u_2) = \frac{1}{2}u_1^2 + \frac{1}{2}u_2^2 + \frac{1}{4}\alpha u_1^4 \quad (1.21)$$

The next step in this analysis is to examine the time derivative of the Lyapunov function. The equation for this derivative is presented as equation (1.22). Because both μ_1 and μ_2 have positive values, the value of the time derivative of the Lyapunov function is less than zero for all values of u_1 and all values of u_2 except zero.

$$\begin{aligned} \frac{d}{d\tau} V(u_1(\tau), u_2(\tau)) &= \\ &- (2\mu_1 + \mu_2 |u_2(\tau)|) u_2^2(\tau) \end{aligned} \quad (1.22)$$

The next step is to ensure that the solution will not remain within region E at any point other than the fixed point forever. E is defined as the region where the time derivative of the Lyapunov function is equal to zero. This region, characterized by function G being equal to zero, is defined in equation (1.24). To determine if the solution will remain at any point forever, the dot product of the time derivative of the state vector, U , and the gradient of this space

is computed. When the value is equal to zero, the solution will remain.

$$U = \{u_1(\tau), u_2(\tau)\} \quad (1.23)$$

$$G(U) = u_2(\tau) \quad (1.24)$$

$$U'(\tau) \cdot \nabla G(U) = -u_1(\tau) - \alpha u_1^3(\tau) \quad (1.25)$$

The resulting equation is given by equation (1.25). The only location where the calculation produces a zero is at the fixed point. This verifies that solutions will converge to the fixed point and no other location.

The final step in proving that the fixed point is globally, asymptotically stable is to ensure that the limit of the Lyapunov function is equal to infinity as the magnitude of the state vector approaches infinity. This relation is shown in equation (1.26).

$$\lim_{\|U\| \rightarrow \infty} (V(u_1(\tau), u_2(\tau))) = \infty \quad (1.26)$$

Because all of the terms have even exponents and positive coefficients, this is true for the Lyapunov function that was used within this analysis. Thus, the fixed point of this system is globally, asymptotically stable.

To further study the system's fixed point at the origin, a number of phase portraits are examined. The first phase portrait is that of the unforced, undamped system. Without the damping, the fixed point becomes a center and the cubic term causes the orbits to have increasingly larger velocities as the amplitude increases. A phase portrait of this type is shown as Figure 4.

When damping is applied to the system, trajectories will converge to the fixed point at a rate dependent on the magnitude and style of the damping. Figure 5 is a phase portrait of the system when linear damping

is present. The trajectories within this phase portrait converge to the fixed point at the origin with a constant rate.

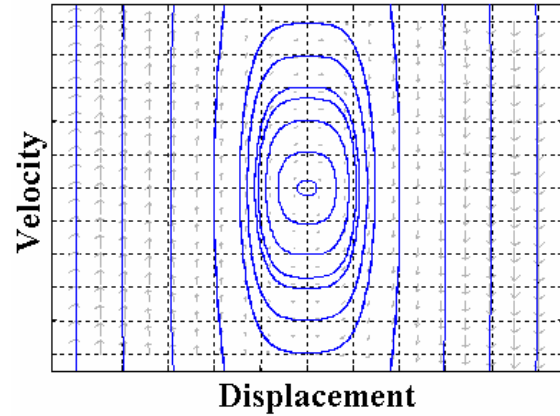


Figure 4: Phase portrait of undamped, unforced system.

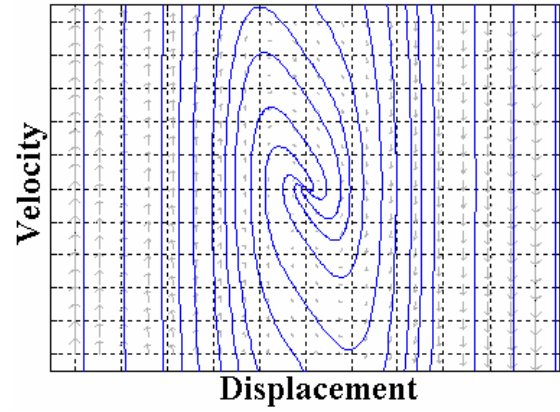


Figure 5: Phase portrait of system with linear damping.

The effects of only nonlinear damping on the phase portrait are shown in Figure 6. In a fashion similar to the linear damping, the center fixed point has become a stable spiral. The difference between the two damping styles also appears within the figure. The trajectories of the phase portrait with nonlinear damping approach the fixed point with a rate that decreases as the trajectory becomes closer to the fixed point. Once a trajectory is sufficiently close to the

fixed point, its convergence rate decreases to a very slow spiral.

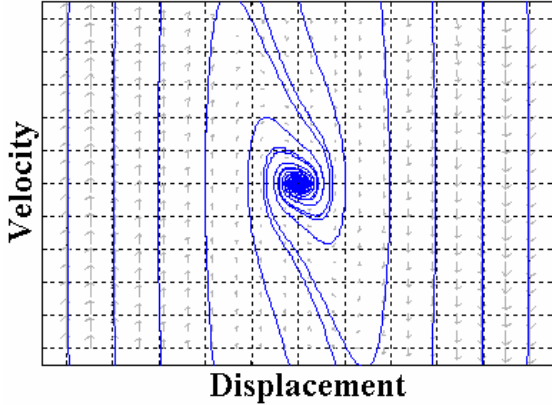


Figure 6: Phase portrait of system with quadratic damping.

When the two types of damping, linear and quadratic, are combined, the resulting phase portrait shows how each affects the behavior of the system. Figure 7 shows that for larger velocities, the quadratic damping term has a dominant affect on the system. As the trajectory approaches the fixed point, the linear damping has the dominant influence of the system's behavior.

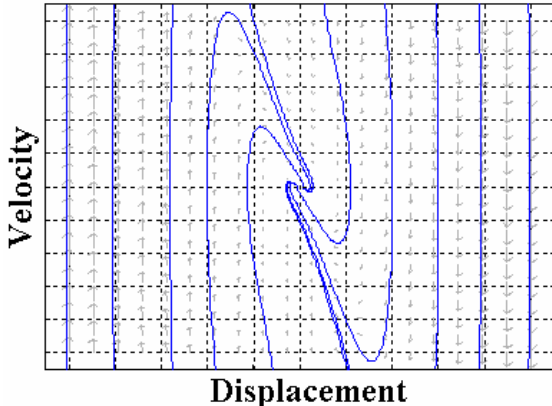


Figure 7: Phase portrait of system with linear and quadratic damping.

After thoroughly studying the unforced system, the dynamic behavior of the forced system is studied. Because the total

conservative energy of this system, which was chosen to be the Lyapunov function, has a limit equal to infinity as the magnitude of the state vector increased to infinity, the behavior of the damped, forced system will not diverge to infinity. This would suggest that the majority of the solutions produced by the system will consist of isolated periodic orbits. The structures of these stable limit cycles will be dependent on the values of all the system's parameters. To explore what type of influence the different parameters have on the system, a number of different numerical simulations were conducted. The base set of parameter values used for these simulations is listed in Table 1.

	μ_1	μ_2	α	F	Ω
Base	0.5	0.1	10	1	1

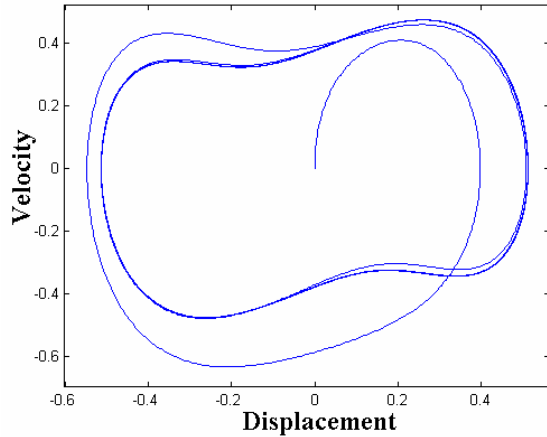


Figure 8: State space of simulation with base parameter values.

These parameter values were chosen to serve as a baseline to which slight modification of each of the parameters are made. The behavior produced by these values shows evidence of the nonlinearity and damping when viewed in a state space representation but they do not produce overly complex dynamics. The time series

of the two state vectors converge to periodic behavior following a short period of transient behavior. A frequency distribution of the displacement signal produces a component with a large magnitude at the system's natural frequency which coincides with the excitation frequency for this simulation. There is also a component with a smaller component at three times the natural frequency, caused by the cubic term.

The first parameter that was examined was the linear damping coefficient. To gain some insight into how it influences the dynamic behavior of the system, the base value in first doubled then halved. Doubling the coefficient causes the trajectory to converge to the limit cycle more quickly. It also results in a decrease in the nonlinearity of the behavior. The time series of the two state variables more closely approximate harmonic oscillations and the second peak in the frequency distribution of the displacement time series is decreased in magnitude. The state space representation of the system, shown as Figure 9, reveals behavior that more closely represents harmonic oscillations. When the value of the linear damping coefficient is decreased, the opposite effects are produced. A longer amount of time is required for the system to converge to the limit cycle and the time series of the two state vectors contain more anharmonic characteristics than the simulation for the base values. The magnitude of the secondary peak of the frequency distribution is also greater for the decreased linear damping coefficient. More nonlinearity can be seen in the state space representation for a smaller linear damping coefficient, shown as Figure 10.

The second parameter to be examined is the nonlinear damping coefficient. When the value of this parameter is doubled, there is very little change to the behavior of the system. Similarly, decreasing the value by half also results in little change to the

dynamics of the system. When the nonlinear damping coefficient is changed by significantly larger amounts, its affect on the system appear to be similar to changes to the linear damping coefficient.

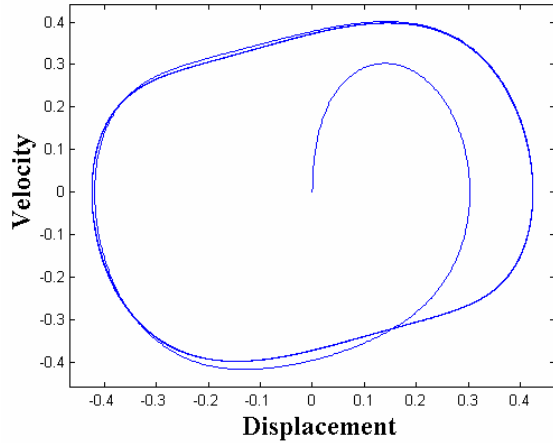


Figure 9: State space for double linear stiffness.

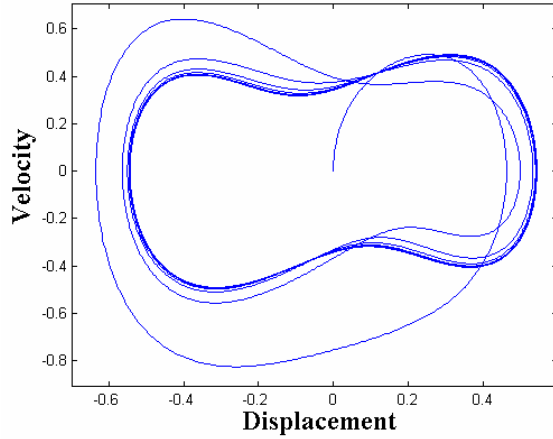


Figure 10: State space for half linear stiffness.

When the value of the nonlinear stiffness coefficient is varied, its affects on the nonlinearity of the system are opposite the affects of changes in the linear damping coefficient. When the value of the nonlinear stiffness coefficient is increased, the behavior is more strongly nonlinear while the convergence of the trajectory to the limit cycle remains unchanged. Decreasing the nonlinear stiffness coefficient has the expected effect of diminishing the amount of

nonlinearity in the system's behavior while not affecting the convergence rate of the trajectory to the limit cycle.

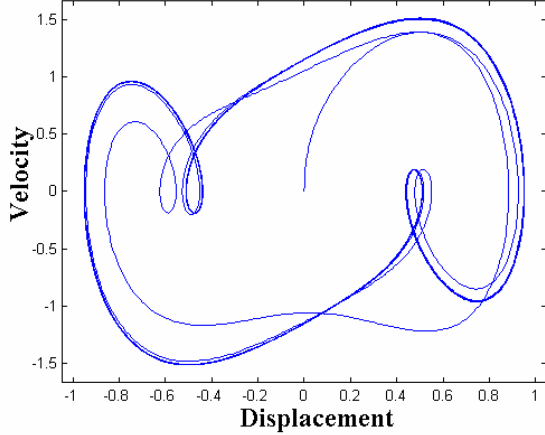


Figure 11: State space for four times the excitation magnitude.

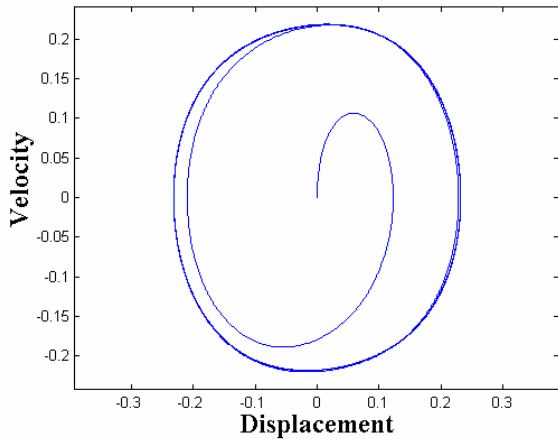


Figure 12: State space for $\frac{1}{4}$ excitation magnitude.

Changes to the magnitude of the excitation also appear to affect the nonlinearity of the behavior of the system. Increasing this value indicates that it has a stronger influence on the dynamics than equivalent variations of the other terms. Increasing this term also causes the range to motion to vary. In addition to adding more complexity to the time series of the two state variables, the second peak of the frequency distribution increases significantly and a third peak is noticeable at about five times

the natural frequency. The state space representation of this system for a larger magnitude of excitation is shown in Figure 11. Again, decreasing the value has the opposite effect on the behavior. When the magnitude of excitation is decreased, the nonlinearity of the system's behavior is significantly diminished. Both time series of the state variables very closely approximate harmonic behavior and the second and third peak of the frequency distribution become negligible. Figure 12 is the state space representation of the system's behavior when the magnitude of excitation is decreased

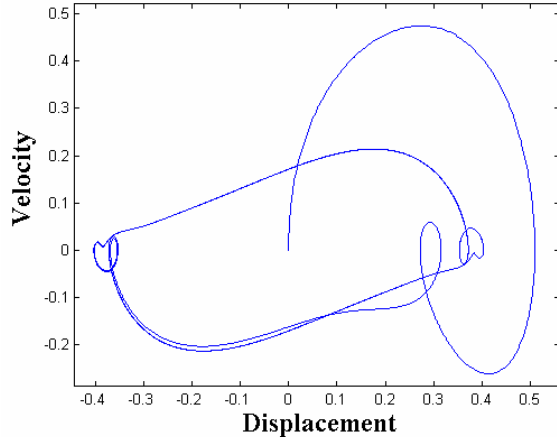


Figure 13: State space for one-quarter of excitation frequency.

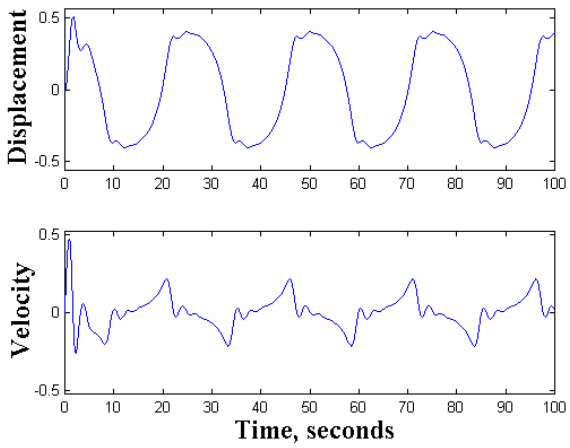


Figure 14: Time series for one-quarter of excitation frequency.

The final parameter value to be examined is the excitation frequency. Increasing the excitation frequency has the effect of causing the system to behave in a more linear fashion while decreasing the frequency causes the system's behavior to exhibit more nonlinearity. When the excitation frequency is increased, the state space view of the system's behavior will be very similar to that shown in Figure 12. When the excitation frequency is decreased, the system displays very strong nonlinear behavior, shown in the state space representation in Figure 13. The time series of the two state variables show very unique periodic behavior, as seen in Figure 14, and the frequency distribution begins to develop peaks at odd multiples of the excitation frequency.

Approximation Solution:

After studying the stability of the unforced system's fixed point and the influence of the parameters on the system's dynamic behavior, an analytical study is conducted to determine an approximate solution to the nonlinear system. The method of multiple scales is used to determine a first order approximation of the system's response [Nayfeh & Mook, 1979]. The method of multiple scales also produces modulation equations describing changes in the response amplitude and phase. The method of multiple scales separates the system's behavior into different time and length scales as shown in equations (1.27), (1.28) and (1.29). This is done using a dimensionless scaling parameter ε , which is considered to have a positive value much less than one.

$$T_n = \varepsilon^n \tau \quad (1.27)$$

$$\frac{d}{d\tau} = \frac{dT_0}{d\tau} \frac{\partial}{\partial T_0} + \frac{dT_1}{d\tau} \frac{\partial}{\partial T_1} + \dots \quad (1.28)$$

$$u(\tau; \varepsilon) = u_0(T_0, T_1, \dots) + \varepsilon u_1(T_0, T_1, \dots) + \dots \quad (1.29)$$

$$u'' + u + \varepsilon (2\mu_1 u' + \mu_2 u' |u'|) + \varepsilon (-2K \cos(\Omega \tau) + \alpha u^3) = 0 \quad (1.30)$$

Before these three equations are used to redefine equation (1.9), the scaling parameter is used to separate the damping, excitation, and nonlinear terms from the rest of the equation. Equation (1.30) is the equation of motion of the system modified with the scaling parameter. This equation can then be separated based on the order of the scaling parameter multiplying each term. To determine the first-order approximation of the system's response, the largest two orders of ε are solved. These two equations are listed below as equation (1.31) and equation (1.32). Equation (1.31) can easily be solved as a harmonic oscillator in time scale T_0 with an amplitude and phase that vary in time scale T_1 as shown in equation (1.33).

$$D_0^2 u_0 + u_0 = 0 \quad (1.31)$$

$$\begin{aligned} D_0^2 u_0 + u_0 &= -2D_0 D_1 u_0 \\ &\quad - 2\mu_1 D_0 u_0 \\ &\quad - \mu_2 D_0 u_0 |D_0 u_0| \\ &\quad - \alpha u_0^3 \\ &\quad + 2K \cos(\Omega T_0) \end{aligned} \quad (1.32)$$

$$u_0(T_0, T_1) = a(T_1) \cos(T_0 + \beta(T_1)) \quad (1.33)$$

$$\Omega = 1 + \varepsilon \sigma \quad (1.34)$$

Using the solution to u_0 , equation (1.32) can be rewritten. To obtain the modulation

equations from equation (1.32), it is necessary to define the nondimensional excitation frequency Ω . The excitation frequency is defined as system's natural frequency plus a small detuning parameter σ , as shown in equation (1.34). The terms on the right hand side of equation (1.32) are then separated into the terms multiplied by a cosine term with the system's natural frequency and the terms multiplied by a sine term with the system's natural frequency. Using trigonometric identities, the cubic term and the excitation term are manipulated into usable forms. A Fourier expansion of the terms resulting from the quadratic damping produces the Fourier components of the desired frequencies. Equation (1.35) shows the relation obtained from the Fourier expansion.

$$\sin(T_0 + \beta(T_1)) - \sin(T_0 + \beta(T_1)) = \frac{8}{3\pi} \sin(T_0 + \beta(T_1)) + \dots \quad (1.35)$$

$$\gamma(T_1) = \sigma T_1 - \beta(T_1) \quad (1.36)$$

$$a'(T_1) = -\mu_1 a(T_1) - \frac{4\mu_2}{3\pi} a^2(T_1) + K \sin(\gamma(T_1)) \quad (1.37)$$

$$a(T_1) \gamma'(T_1) = \sigma a(T_1) - \frac{3}{8} \alpha a^3(T_1) + K \cos(\gamma(T_1)) \quad (1.38)$$

To eliminate the secular term, the coefficients of all the terms multiplied by cosine of the system's natural frequency are set equal to zero. This is also done to the coefficients of the sine terms. These two equations yield the two modulation equations of the system. Using the variable γ defined in equation (1.36), the modulation equations are simplified to produce equations (1.37) and (1.38). With the approximation complete, the transverse

deflection of the resonator can be defined by equation (1.39) where the nondimensional time τ is replaced by the product of the natural frequency and the dimensional time.

$$W(x, t) = a(\omega_n t) \cos(\omega_n t + \beta(\omega_n t)) \phi(x) + \dots \quad (1.39)$$

The modulation equations obtained from this perturbation analysis are used to gain further insight into the behavior of the resonators. By defining the two equations for the fixed points of the system, the change in the amplitude and the change in the phase are equal to zero. The resulting equations are combined to eliminate their dependence on the value of the phase and produce an equation that can be used to explore the relationship between the excitation frequency and the response amplitude. The frequency-response equation for this system is given as equation (1.40).

$$\left(\left(\mu_1 + \frac{4\mu_2}{3\pi} a_0 \right)^2 + \left(\sigma - \frac{3}{8} \alpha a_0^2 \right)^2 \right) a_0^2 = K^2 \quad (1.40)$$

By solving this equation for the detuning parameter σ , two equations are produced that provide the two halves of the frequency-response curve. These equations are given as equation (1.41). For selected values of μ_1 , μ_2 , α , and K this curve can be plotted for a range of values of the detuning parameter. An example of this curve is shown in Figure 15.

$$\sigma_{1,2} = \frac{3}{8} a_0^2 \alpha \pm \frac{1}{3 a_0 \pi} \left(\sqrt{9K^2 \pi^2 - a_0^2 (3\pi\mu_1 + 4a_0\mu_2)^2} \right) \quad (1.41)$$

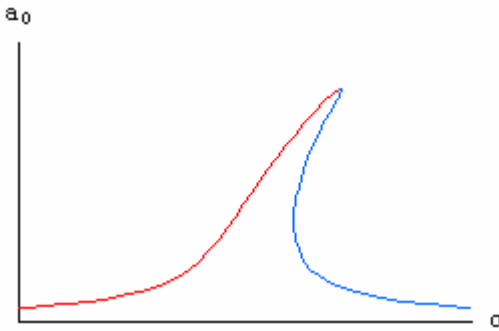


Figure 15: Frequency-response curve.

From the previous equation, the exact location of the maximum response amplitude is calculated. This location is where the two equations of equation (1.41) are equal and it is defined by equation (1.42) and equation (1.43). By examining a close-up view of the maximum response amplitude in Figure 16, it can be seen that this point does not coincide with tip of the response amplitude. As a result, this location does not provide any information concerning the stability of the system. In order to gain information about the stability of the system, a stability analysis is conducted on the modulation equations.

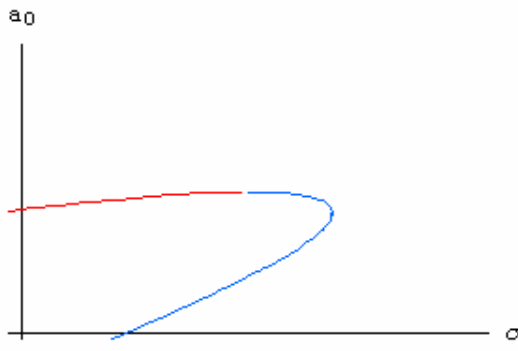


Figure 16: Close-up view of maximum response amplitude.

$$a_{\max} = \frac{-3\pi\mu_1 + \sqrt{9\pi^2\mu_1^2 + 54K\pi\mu_2}}{8\mu_2} \quad (1.42)$$

$$\sigma_{\max} = \frac{3\alpha}{512\mu_2^2} \left(-3\pi\mu_1 + \sqrt{9\pi^2\mu_1^2 + 54K\pi\mu_2} \right)^2 \quad (1.43)$$

The Jacobian matrix is constructed from the modulation equations solved for the fixed points. Using the modulation equations, substitutions are made to remove the phase, γ_0 , from the matrix. The eigenvalues can then be calculated to determine the stability of the fixed point as a function of the system parameters. The boundary between the stable and unstable behavior will exist where one of the eigenvalues is equal to zero. For this case, the characteristic equation indicates that the determinant of the Jacobian matrix is equal to zero. The determinant of the Jacobian matrix provides a relation between excitation frequency and the response amplitude where the critical points exist and a change in the stability of the frequency-response curve occurs. This critical points equation is presented as equation (1.44). Similar to the frequency-response equation, the critical points equation can be solved for the detuning parameter to produce two equations to plot the two halves of the critical points curve.

$$\begin{aligned} & \left(\mu_1 + \frac{8\mu_2}{3\pi} a_0 \right) \left(\mu_1 + \frac{4\mu_2}{3\pi} a_0 \right) \\ & + \left(\sigma - \frac{3}{8}\alpha a_0^2 \right) \left(\sigma - \frac{9}{8}\alpha a_0^2 \right) = 0 \end{aligned} \quad (1.44)$$

$$\begin{aligned} \sigma_{3,4} = & \frac{3}{4} a^2 \alpha \\ & \pm \frac{1}{24\pi} \sqrt{\begin{matrix} 81a^4\pi^2\alpha^2 \\ -576\pi^2\mu_1^2 \\ -2304a\pi\mu_1\mu_2 \\ -2048a^2\mu_2^2 \end{matrix}} \end{aligned} \quad (1.45)$$

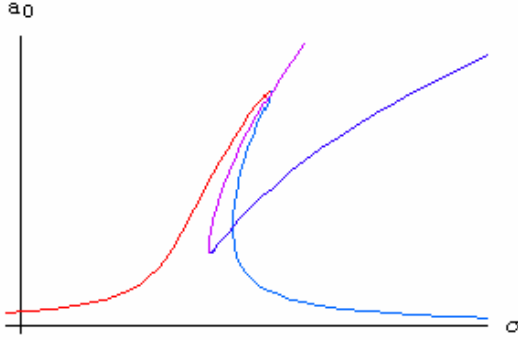


Figure 17: Frequency-response curve with the critical points curve.

In order to determine the exact locations where the critical points curve intersect the frequency-response curve, the equations for the two curves are set equal to each other. One point is located by setting σ_2 equal to σ_3 and the other point comes from σ_2 equal to σ_4 . Due to the complexity of the equations, a general solution is extremely complicated. For a given set of parameter values, the amplitude and detuning parameter values corresponding to the bifurcations can be obtained. With this information, it is possible to identify the stable and unstable portions of the frequency-response curve. Figure 18 is the frequency-response curve with stability information from the critical points curve. The dashed portion of the frequency-response curve is unstable while the solid lines represent the stable portion.

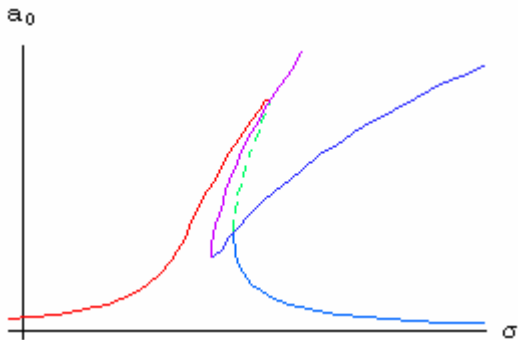


Figure 18: Frequency-response curve with stability information.

The stability information gained from this analysis can be verified by numerically simulating the amplitude of the oscillator while the value of the detuning parameter is varied. This is done using the modulation equations and running the simulation for a given detuning parameter value until the amplitude and phase of the response converge to a steady-state solution. After the values have converged, the final values are used as the initial values for the next simulation where the detuning parameter has been incremented. By starting at a detuning parameter corresponding to a frequency below the system's natural frequency and sweeping up to a frequency above the system's natural frequency, a frequency-response curve is produced. This is done by plotting the steady-state amplitude against the corresponding detuning parameter values. This frequency-response curve will behave in a similar fashion as the resonators with respect to the unstable portion of the frequency-response curve. A second, unique frequency-response curve can be produced by starting above the system's natural frequency and sweeping downward. The simulated frequency-response curves are shown in Figure 19.

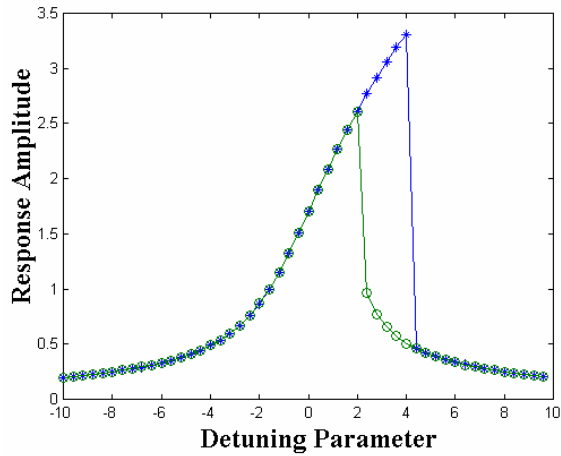


Figure 19: Simulated frequency-response curve.

This figure contains the frequency-response curve for both forward and backward sweeps. The figure reveals how jumps will exist in the frequency-response curve when the detuning parameter approaches the two bifurcation points on the frequency-response curve.

Parameter Identification:

The parametric identification scheme that will be used to study the data from the micro-scale resonators utilizes both the frequency-response equation and the critical points equation to identify the location of the upper bifurcation. To determine the order to which the parameters should be optimized, the influence of each of the parameters is recognized. With this information, the parameter with the most influence on the structure of the frequency-response curve can be optimized first followed by the parameters with less influence. The linear stiffness parameter is found to have the most influence on the frequency-response curve. Increasing the linear stiffness parameter causes the first linear natural frequency of the system to increase shifting the frequency-response curve to higher frequencies. Figure 20 shows a dashed frequency-response curve with a higher linear stiffness parameter relative to the solid frequency-response curve.

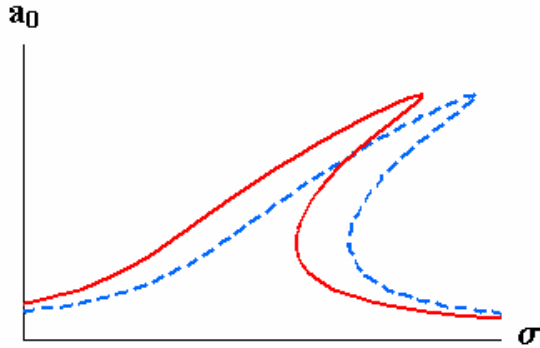


Figure 20: Change in linear stiffness coefficient.

The next most influential parameter is the excitation magnitude. Similar to any other driven system, the magnitude of the excitation is directly related to the level of the response amplitude. The dashed curve in Figure 21 differs from the solid curve by an increase in the excitation magnitude.

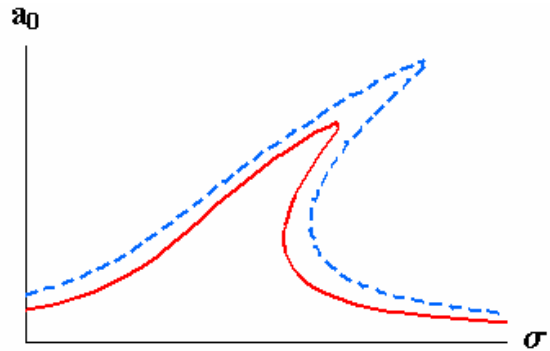


Figure 21: Change in excitation magnitude.

The parameter that has the third most influence on the response is the nonlinear stiffness parameter. This parameter directly affects the nonlinearity of the response which is defined as the deviation of the response from the symmetric linear response. An increase in the positive coefficient causes the hardening type nonlinearity to lean further to the right as seen in Figure 22. The dashed curve corresponds to a larger positive nonlinear stiffness value than the solid curve.

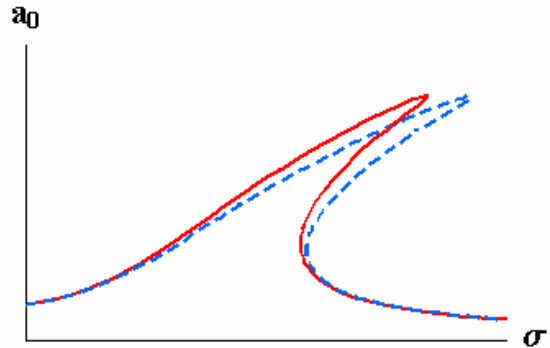


Figure 22: Change in nonlinear stiffness coefficient.

The last two parameters to be examined are the linear and quadratic damping coefficients. Each of these coefficients characterizes the energy dissipation resulting from the two different types of damping. As a result, changing the value of this coefficient alters the response amplitude of the system. The change of the response amplitude is most notable around the system's linear natural frequencies. Figure 23 and Figure 24 contain frequency-response curves where the dashed curve shows an increase in the linear damping coefficient and quadratic damping coefficients, respectively. Although these represent different types of damping, the effect of changing these parameters appears to be very similar.

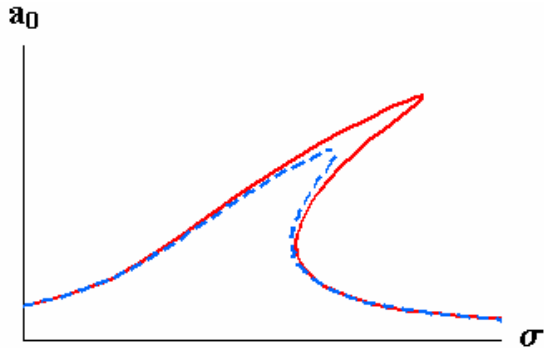


Figure 23: Change in linear damping coefficient.

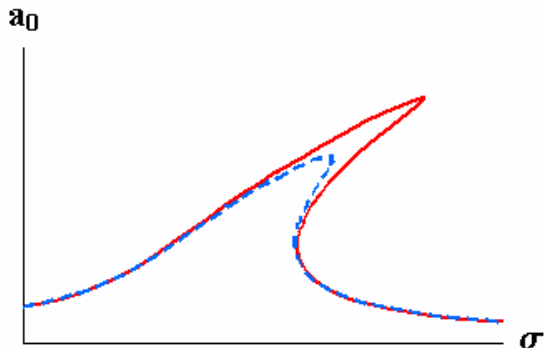


Figure 24: Change in quadratic damping coefficient.

In order to identify the difference in how the two damping types affect the structure of

the frequency response curve, two linear curves are plotted in Figure 25. With the nonlinear stiffness coefficient set equal to zero, the solid curve is plotted with only linear damping and the dashed line is plotted with only quadratic damping. The values of the coefficients are adjusted to produce matching peak amplitudes. This figure shows that in addition to influencing the value of the peak amplitude, these parameters affect the bandwidth of the frequency response curve. Using this information, it will be possible for a parametric identification scheme to determine a combination of the linear damping coefficient and the quadratic damping coefficients that provides the necessary maximum response amplitude as well as the appropriate bandwidth of the frequency-response curve.

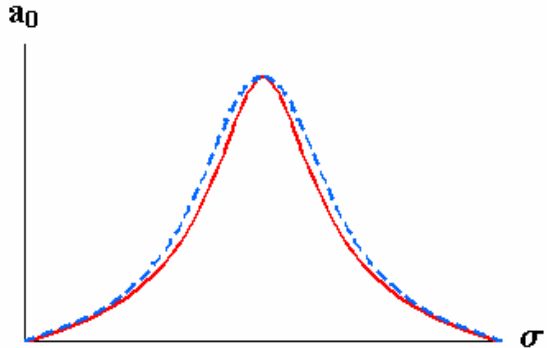


Figure 25: Linear and quadratic damping.

The first step in the parameter identification scheme is to optimize the parameters that affect the structure of the frequency response curve. This is done by tuning the first four parameters to minimize the amount of error calculated from equation (1.46). This equation calculates the sum squared error of the N data points from the experimental frequency response curve. While minimizing this error, the linear stiffness coefficient, excitation magnitude, nonlinear stiffness coefficient, and quadratic damping coefficient are optimized.

$$\sum_{n=1}^N \left(\left(\left(\mu_1 + \frac{4\mu_2}{3\pi} a(n) \right)^2 + \left(\sigma(n) - \frac{3\alpha}{8} a^2(n) \right)^2 \right) a^2(n) - K^2 \right)^2 \quad (1.46)$$

As these parameters are optimized, the process does not take into account changes in the maximum amplitude. Tuning of the excitation magnitude and quadratic damping coefficient can cause the peak of the analytical curve to vary greatly from the experimental data. In order to correct this, the next step in the parametric identification process tunes the linear damping coefficient to minimize the amplitude difference between the last data point before the amplitude jump and the location of the upper bifurcation point. This is done using equation (1.47).

$$\text{Error} = (a_{\text{bifurcation}} - a_{\text{jump}})^2 \quad (1.47)$$

The theoretical amplitude value is defined by the location where the right-hand side of the frequency-response curve intersects the upper half of the critical points curve. In order to determine the location of this point, the identification scheme calculates the difference between these equations and locates the amplitude where the difference is equal to zero. In order to chose an effective starting point, the maximum amplitude of the response is used because this point can be calculated explicitly using equation (1.42).

In the final step of the parametric identification scheme, a linear model is used to determine the level of axial force within the resonator and refine the value of the modal mass. This is done using a finite-element model of the linearized system previously mentioned and shown as equation (1.48). By assuming harmonic oscillations, the natural frequencies and mode shapes of the linear model can be

calculated. Tuning the value of the axial force enables the first natural frequency of the linear model to be adjusted to be equal to the linear natural frequencies identified from the experimental data. The mode shape obtained from this analysis, which corresponds to the identified linear natural frequency, is then used to recalculate the modal mass of the vibrating structure.

$$\rho A_n \frac{\partial^2 W_n(x,t)}{\partial t^2} + EI_n \frac{\partial^4 W_n(x,t)}{\partial x^4} + P_{0,n} \frac{\partial^2 W_n(x,t)}{\partial x^2} = 0 \quad (1.48)$$

Since there are multiple parameters being optimized, each parameter is no long optimal once one of the other parameters has been changed. Because of this, these three steps must be carried out multiple times to allow the entire set of parameters to converge to the optimal set. With each iteration of the process, the parameters move closer to providing the unique set which describes the experimental data of the piezoelectric micro-scale resonator. After the values have sufficiently converged, the parameter values can be studied.

To study how well the aerodynamic damping model describes the behavior of the micro-scale resonators three different sets of data are examined. The first data set was collected from a piezoelectric resonator while the driving voltage was incrementally increased. The second data set was collected at a constant driving voltage but with an incrementally increasing DC bias. The final data set was collected from a resonator with a constant driving voltage and no DC bias but decreasing pressure levels.

The changes in the damping coefficients for the first data set indicate that the aerodynamic damping does indeed have a significant influence on the system. While

the results in Figure 26 show the linear damping coefficient, the upper set, has greater values than the quadratic damping coefficient, the coefficient of the nonlinear term experiences a much larger relative change. The coefficients have units of Ns/m and Ns^2/m for the linear damping coefficient and the quadratic damping coefficient, respectively. Both the linear and quadratic damping coefficients increase as the driving voltage increases. This would indicate that the larger motions affect both the structural damping of the resonators as well as their interactions with the air around them.

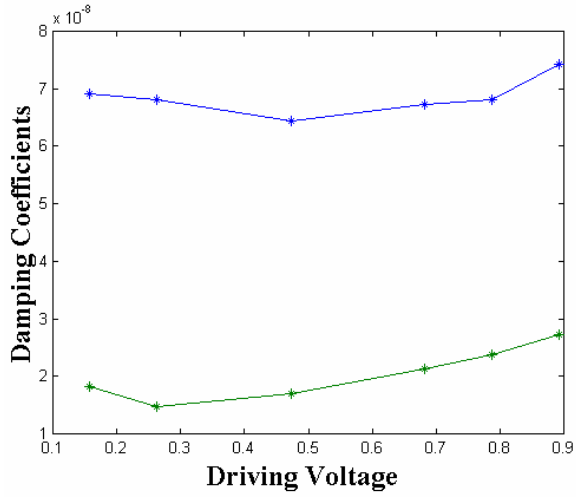


Figure 26: Damping coefficients versus driving voltage.

The data set corresponding to the steady increase in the level of DC bias added to the signal also shows that the linear damping coefficient has values greater than the quadratic damping coefficient. The identified damping values are shown in Figure 27. There appears to be a decrease in the values of the coefficients for the linear damping. This may be a result of changes to the internal structure caused by the additional axial force. As the DC bias increases, the quadratic damping coefficient increases significantly from its initial value.

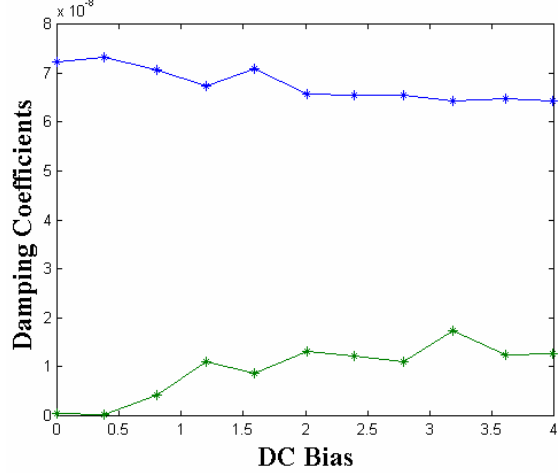


Figure 27: Damping coefficients versus DC bias.

The final data set produced results that vary from the previous two. For the third data set, the values of the quadratic damping coefficients were greater than the linear damping coefficients. These trends are shown in Figure 28 where it can be seen that both of the damping coefficients have a general decreasing trend as the pressure level decreases. While the decrease in the pressure would result in a decrease in the amount of aerodynamic damping, it is expected that the larger amplitude motions would result in increased linear damping. These results bring the effectiveness of the parameter identification scheme into question.

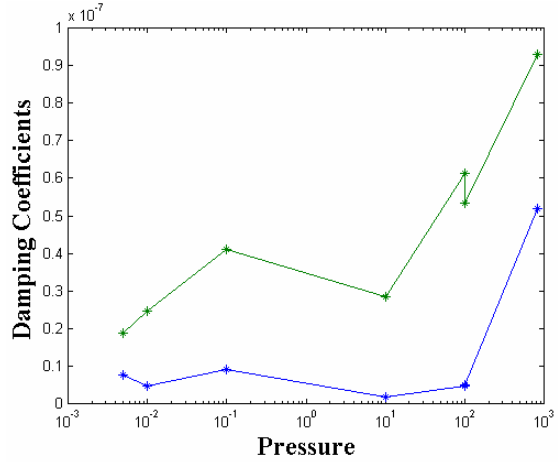


Figure 28: Damping coefficients versus pressure.

Conclusion:

The initial analysis of the model that includes aerodynamic damping would suggest that it may serve as a suitable representation of the piezoelectric micro-scale resonators. The model is globally, asymptotically stable and its dynamic behavior is found to converge to a stable periodic solution. The frequency-response equation obtained from a first-order approximation can produce the structure of the frequency-response curve seen in experimental data. Investigations of the frequency-response curve revealed how each of the parameters influences the curve. The two damping terms are found to affect the analytical frequency-response in a very similar manner with only a small difference. While the difference is noticeable when examining a linear system, the presence of the nonlinearity may reduce this variation. Trends of the two damping parameters were examined for changes in three conditions: driving voltage, DC bias, and pressure. While the behavior of some of the identified trends is what would be expected, other trends are observed that contradict to what is anticipated. It may be possible that when applied to experimental data, the slight difference in how the two damping

parameters influence the curve is not significant enough to produce a unique set of values for a given set of experimental data. In order to locate the optimal set of parameter values, it may be necessary to devise a means to select the initial guesses to allow the parameters to converge to their optimal values.

References:

- DeVoe, D.L. (2001) Piezoelectric thin film micromachined beam resonators. *Sensors and Actuators A(Physical)*, **A88**(3), pp.263-272.
- Dick, A.J., Balachandran, B., DeVoe, D.L., Mote, C.D., (2005) Parametric Identification of Piezoelectric Micro-Scale Resonators. In *Proc. EUROMECH Nonlinear Oscillations Conference*. Eindhoven, The Netherlands, Aug. 2005.
- Hyvarinen, J., Soderkvist, J., (2001) Aeroelasticity – the interplay between fluids and solids. *J. Micromech. and Microeng.*, **11**, pp. 416-422.
- Nayfeh, A.H., Balachandran, B. (1995) *Applied Nonlinear Dynamics: Analytical, Computational, and Experimental Methods*. Wiley, New York.
- Nayfeh, A.H., Mook, D.T., (1979) *Nonlinear Oscillations*. Wiley, New York.
- Preidikman, S., Li, H., Balachandran, B. (2003) Forced oscillations of microelectromechanical resonators. In *Proc. ASME Inter. Mech Eng. Cong.* Washington, D.C., USA, Nov. 15-21, pp. 1-7.

ENME 665 Project:
Biologically Inspired Algorithms for Flocking

Xiaorui Xi
Dept. of Electrical and Computer Engineering
& the Institute for Systems Research
University of Maryland, College Park, MD 20742

Instructor: B. Balachandran,
Professor of Mechanical Engineering

May 16, 2005

1 Introduction

A flock is a group of mobile autonomous agents in which, while each agent follows certain simple rules based on local information, at the group level the agents are enabled to move together in formation and to perform desired tasks. The idea of flocking in multi-agent systems is inspired by observations in biology [2, 3]. Animal and insect behaviors such as swarming of ants, flocking of birds, schooling of fishes and herding of land animals are some examples of flocking in nature. Flocking can be applied in many different areas including moving in formation for fleets of unmanned aerial vehicles (UAVs), autonomous underwater vehicles (AUVs), cooperating robots, and satellite clusters.

In 1987, Reynolds [1] introduced three local rules for agents he named “boids,” and implemented these in a computer program that simulated the flocking of birds. The three rules are: *separation*, avoiding collisions with neighboring boids, *alignment*, matching velocity with neighboring boids, and *cohesion*, staying close to the neighboring boids. Since then, many researchers followed in applying these three rules of flocking to design the behavior of individual agents interacting with their neighbors (e.g., [4]-[10]). In [6]-[10], use was made of a local *attractive/repulsive potential* to set the interactive force between neighboring agents to implement the separation and cohesion rules. The *tracking* problem that appears in flocking arises when the group of agents needs to follow a desired path. This is addressed by the (virtual) leader/follower approach in [5]-[7], [11], and the non-leader approach in [8].

In this project, we introduce a pre-specified formation design for flocking based on virtual leaders and two different interactive forces. One is the *attractive* force, which is imposed on each agent by its virtual leader to achieve the goals of *tracking*, *alignment* and *cohesion*. The other is the *repulsive* force, which is imposed on each agent by its neighboring agents to solve the *separation* problem. The *repulsive* force between agents is assumed to vanish outside the immediate neighborhood of any agent.

The remainder of the report proceeds as follows. In Section 2, we introduce the pre-specified formation design. Analytical results are presented in Section 3. Section 4 provides some simulation results, and conclusions are summarized in Section 5.

2 Problem Formulation

Consider a group of N identical mobile agents, modelled as point particles, moving in a plane with the following dynamics:

$$\begin{aligned}\dot{r}_i &= v_i \\ \dot{v}_i &= a_i\end{aligned}\tag{1}$$

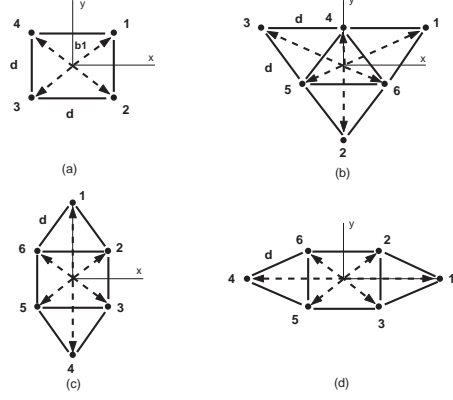


Figure 1: Four specified desired formations

where r_i , v_i and $a_i \in \mathbb{R}^2$ are the position, velocity and acceleration of agent i . The relative displacement of agents i from j is denoted by $r_{ij} = r_i - r_j$. The neighborhood of agent i is defined as a circle of radius d around agent i .

In this design, we introduce a desired path given by the trajectory of $r_0(t)$ and N virtual leaders at r_{id} , $i = 1, \dots, N$, one for each agent. The trajectory of r_{id} is given by $r_{id}(t) = r_0(t) + b_i$, where $b_i \in \mathbb{R}^2$ is a constant vector. The values of the b_i s are predefined to specify the desired formation.

Fig. 1. shows four possible desired formations, where the solid dots denote the agents and any two agents linked by a solid line are neighbors. Fig. 1. (a) is a square formation for a 4-agent group. Fig. 1. (b), (c) and (d) are examples for a 6-agent group, where all neighboring agents are equally spaced. In each figure, the distance between any two neighbors is equal to d , the *sensing radius*. The geometric center of each desired formation is taken to be the origin. So, for example, the values of b_i s in Fig. 1. (a) can be set as $b_1 = (a, a)^T$, $b_2 = (a, -a)^T$, $b_3 = -b_1$ and $b_4 = -b_2$, where $a = d/2$ is a scalar constant.

In this design, formation *translation* and *rotation* can be implemented by changing the values of b_i s at the instant of translation or rotation. However the change in b_i s needs not to be abrupt, since a relaxation period can be allowed for this change.

In this design, the values of b_i s must satisfy the following two conditions:

1. $\frac{1}{N} \sum_{i=1}^N b_i = 0$;
2. If agent i and j are neighbors, then $\|b_j - b_i\| = d$.

In equation (1), a_i consists of three parts as follows

$$a_i = F_{\mathcal{A}_i} + F_{\mathcal{R}_i} + F_{\mathcal{D}_i} \quad (2)$$

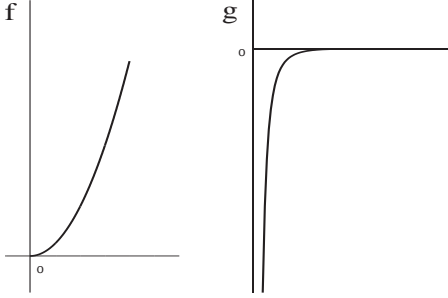


Figure 2: The functions f and g

where $F_{\mathcal{A}_i}$ represents the *attractive* force that drives agent i to track its virtual leader, hence making the group to approach the desired formation, $F_{\mathcal{R}_i}$ is the *repulsive* force that controls the distances between agent i and all its neighbors and $F_{\mathcal{D}_i}$ represents the controlled dissipative force, which is designed to be zeros when the agent i is moving at its virtual leader's velocity $\dot{r}_0(t) = q(t)$. Note that all the virtual leaders have the same velocities.

In equation (2), $F_{\mathcal{A}_i}$ can be expressed in the following form:

$$F_{\mathcal{A}_i} = f(\|r_{id} - r_i\|) \frac{r_{id} - r_i}{\|r_{id} - r_i\|} \quad (3)$$

where $f : R_{\geq 0} \rightarrow R_{\geq 0}$ is a continuous, monotonously increasing function, which represents the magnitude of the *attractive* force imposed on agent i by its virtual leader. The form of f is illustrated in Fig. 2 (left). As can be seen, when $\|r_{id} - r_i\| = 0$, $f = 0$, indicating that agent i has met its virtual leader at r_{id} and no tracking. When $\|r_{id} - r_i\| > 0$, $f > 0$, meaning that agent i is being attracted toward its virtual leader. We define $f(\|0\|)/(\|0\|) = 0$.

The form of $F_{\mathcal{R}_i}$ is taken to be as follows

$$F_{\mathcal{R}_i} = \sum_{j \in N_i(t)} g(\|r_j - r_i\|) \frac{r_j - r_i}{\|r_j - r_i\|} \quad (4)$$

where $N_i(t)$ denotes the label set of agent i 's neighbors at time t and $g : R_{\geq 0} \rightarrow R_{\geq 0}$ is a continuous function. The function g represents the magnitude of a short-range force exerted on an agent by its neighbors, whose general form is illustrated in Fig. 2 (right). As can be seen, if $\|r_j - r_i\| \geq d$, then $g = 0$ and there is no g -force on agent i . If $0 < \|r_j - r_i\| < d$, $g < 0$, which drives agent i to move away from agent j . We also constraint the function g as a monotonously increasing function when $0 < \|r_j - r_i\| < d$. Note that agent collisions are avoided by the fact that $g(\|r_j - r_i\|)$ goes to infinity as $\|r_j - r_i\|$ approaches zero.

The form of the dissipative force $F_{\mathcal{D}_i}$ can be expressed as follows

$$F_{\mathcal{D}_i} = -a(v_i - q(t)) \quad (5)$$

where a is a positive constant.

We summarize the pre-specified formation design as

$$\begin{aligned}\dot{r}_i &= v_i \\ \dot{v}_i &= f(\|r_{id} - r_i\|) \frac{r_{id} - r_i}{\|r_{id} - r_i\|} + \sum_{j \in N_i(t)} g(\|r_j - r_i\|) \frac{r_j - r_i}{\|r_j - r_i\|} - a(v_i - q(t))\end{aligned}\quad (6)$$

3 Analysis

In this project, we only consider a simple system by specifying system (6) as following:

1. $r_0(t) = q$, where $q \in \mathbb{R}^2$ is a constant vector, which means that the velocities of the virtual leaders do not change;
2. f is a linear function, i.e. $f(\|\cdot\|) = k\|\cdot\|$, where k is a positive constant;
3. The dissipative force parameter $a = 1$.
4. The desired formation is pre-specified by setting $b_1 = (b_{1x}, b_{1y})^T = (d/2, 0)^T$ and $b_2 = (b_{2x}, b_{2y})^T = (-d/2, 0)^T$. Note that we always can rotate any other desired formation to this one around the original.

So the dynamics of the simple system is as follows:

$$\begin{aligned}\dot{r}_i &= v_i \\ \dot{v}_i &= -k(r_i - r_{id}) + \sum_{j \in N_i(t)} g(\|r_j - r_i\|) \frac{r_j - r_i}{\|r_j - r_i\|} - v_i + q(t)\end{aligned}\quad (7)$$

Denoting $\tilde{r}_i = r_i - r_0$ and $\tilde{v}_i = v_i - q$, equation (7) becomes

$$\begin{aligned}\dot{\tilde{r}}_i &= \tilde{v}_i \\ \dot{\tilde{v}}_i &= -k(\tilde{r}_i - b_i) + \sum_{j \in N_i(t)} g(\|\tilde{r}_j - \tilde{r}_i\|) \frac{\tilde{r}_j - \tilde{r}_i}{\|\tilde{r}_j - \tilde{r}_i\|} - \tilde{v}_i\end{aligned}\quad (8)$$

3.1 Two-agent group ($N = 2$)

In this section, we consider the case when $N = 2$. We define the states of system (8) as $\tilde{r}_1 = (\tilde{x}_1, \tilde{y}_1)^T$, $\tilde{r}_2 = (\tilde{x}_2, \tilde{y}_2)^T$, $\tilde{v}_1 = (\tilde{v}_{1x}, \tilde{v}_{1y})^T$ and $\tilde{v}_2 = (\tilde{v}_{2x}, \tilde{v}_{2y})^T$, so we have

$$\begin{aligned}
\dot{\tilde{x}}_1 &= \tilde{v}_{1x} \\
\dot{\tilde{y}}_1 &= \tilde{v}_{1y} \\
\dot{\tilde{x}}_2 &= \tilde{v}_{2x} \\
\dot{\tilde{y}}_2 &= \tilde{v}_{2y} \\
\dot{\tilde{v}}_{1x} &= -k(\tilde{x}_1 - b_{1x}) + g(\tilde{\rho}) \frac{\tilde{x}_2 - \tilde{x}_1}{\tilde{\rho}} - \tilde{v}_{1x} \\
\dot{\tilde{v}}_{1y} &= -k(\tilde{y}_1 - b_{1y}) + g(\tilde{\rho}) \frac{\tilde{y}_2 - \tilde{y}_1}{\tilde{\rho}} - \tilde{v}_{1y} \\
\dot{\tilde{v}}_{2x} &= -k(\tilde{x}_2 - b_{2x}) + g(\tilde{\rho}) \frac{\tilde{x}_1 - \tilde{x}_2}{\tilde{\rho}} - \tilde{v}_{2x} \\
\dot{\tilde{v}}_{2y} &= -k(\tilde{y}_2 - b_{2y}) + g(\tilde{\rho}) \frac{\tilde{y}_1 - \tilde{y}_2}{\tilde{\rho}} - \tilde{v}_{2y}
\end{aligned} \tag{9}$$

where $\tilde{\rho} = \sqrt{(\tilde{x}_1 - \tilde{x}_2)^2 + (\tilde{y}_1 - \tilde{y}_2)^2}$, b_{ix} is the first component of b_i and b_{iy} is the second component of b_i , for $i = 1, 2$.

Note that if we introduce $\tilde{x} = \tilde{x}_1 - \tilde{x}_2$, $\tilde{y} = \tilde{y}_1 - \tilde{y}_2$, $\tilde{v}_x = \tilde{v}_{1x} - \tilde{v}_{2x}$ and $\tilde{v}_y = \tilde{v}_{1y} - \tilde{v}_{2y}$, we can reduce system (9) to a new system (10):

$$\begin{aligned}
\dot{\tilde{x}} &= \tilde{v}_x \\
\dot{\tilde{y}} &= \tilde{v}_y \\
\dot{\tilde{v}}_x &= -k(\tilde{x} - b_{12x}) - g(\rho) \frac{\tilde{x}}{\rho} - \tilde{v}_x \\
\dot{\tilde{v}}_y &= -k(\tilde{y} - b_{12y}) - g(\rho) \frac{\tilde{y}}{\rho} - \tilde{v}_y
\end{aligned} \tag{10}$$

where $b_{12x} = b_{1x} - b_{2x}$ and $b_{12y} = b_{1y} - b_{2y}$.

From equation (10), we get the matrix of first partial derivatives of this system, denoted as J , as following

$$J_1 = \begin{pmatrix} 0 & 0 & 1 & 0 \\ 0 & 0 & 0 & 1 \\ a_{11} & a_{12} & -1 & 0 \\ a_{12} & a_{22} & 0 & -1 \end{pmatrix}$$

where

$$\begin{aligned}
a_{11} &= -k - g'(\tilde{\rho}) \frac{\tilde{x}^2}{\tilde{\rho}^2} - g(\tilde{\rho}) \frac{1}{\tilde{\rho}} + g(\tilde{\rho}) \frac{\tilde{x}^2}{\tilde{\rho}^3} \\
a_{12} &= -g'(\tilde{\rho}) \frac{\tilde{x}\tilde{y}}{\tilde{\rho}^2} + g(\tilde{\rho}) \frac{\tilde{x}\tilde{y}}{\tilde{\rho}^3} \\
a_{22} &= -k - g'(\tilde{\rho}) \frac{\tilde{y}^2}{\tilde{\rho}^2} - g(\tilde{\rho}) \frac{1}{\tilde{\rho}} + g(\tilde{\rho}) \frac{\tilde{y}^2}{\tilde{\rho}^3}
\end{aligned}$$

where $\tilde{\rho} = \sqrt{\tilde{x}^2 + \tilde{y}^2}$.

By using the software "Mathematica 5.0", we can get the eigenvalues of J as following

$$\begin{aligned}\lambda_J^1 &= -\frac{1}{2} - \frac{1}{2}\sqrt{1 + 2a_{11} + 2a_{22} - 2\sqrt{a_{11}^2 + 4a_{12}^4 - 2a_{11}a_{22} + a_{22}^2}} \\ \lambda_J^2 &= -\frac{1}{2} + \frac{1}{2}\sqrt{1 + 2a_{11} + 2a_{22} - 2\sqrt{a_{11}^2 + 4a_{12}^4 - 2a_{11}a_{22} + a_{22}^2}} \\ \lambda_J^3 &= -\frac{1}{2} - \frac{1}{2}\sqrt{1 + 2a_{11} + 2a_{22} + 2\sqrt{a_{11}^2 + 4a_{12}^4 - 2a_{11}a_{22} + a_{22}^2}} \\ \lambda_J^4 &= -\frac{1}{2} + \frac{1}{2}\sqrt{1 + 2a_{11} + 2a_{22} + 2\sqrt{a_{11}^2 + 4a_{12}^4 - 2a_{11}a_{22} + a_{22}^2}}\end{aligned}$$

It is very hard to find the fixed points of system (10), even though we can find them, it is also very difficult to analyze their stabilities.

We define a matrix A as following:

$$A = \begin{pmatrix} a_{11} & a_{12} \\ a_{12} & a_{22} \end{pmatrix}$$

and find its eigenvalues:

$$\begin{aligned}\lambda_A^1 &= \frac{a_{11} + a_{22} - \sqrt{a_{11}^2 + 4a_{12}^4 - 2a_{11}a_{22} + a_{22}^2}}{2} \\ \lambda_A^2 &= \frac{a_{11} + a_{22} + \sqrt{a_{11}^2 + 4a_{12}^4 - 2a_{11}a_{22} + a_{22}^2}}{2}\end{aligned}$$

Since A is a real, symmetric matrix, λ_A^1 and λ_A^2 are real. The relationship between the eigenvalues of J and the eigenvalues of A can be found as following:

$$\begin{aligned}\lambda_J^1 &= -\frac{1}{2} - \frac{1}{2}\sqrt{1 + 4\lambda_A^1} \\ \lambda_J^2 &= -\frac{1}{2} + \frac{1}{2}\sqrt{1 + 4\lambda_A^1} \\ \lambda_J^3 &= -\frac{1}{2} - \frac{1}{2}\sqrt{1 + 4\lambda_A^2} \\ \lambda_J^4 &= -\frac{1}{2} + \frac{1}{2}\sqrt{1 + 4\lambda_A^2}\end{aligned}$$

It is easy to see that the real parts of λ_J^1 and λ_J^3 are always negative regardless of the values of λ_A^1 and λ_A^2 . About the signs of the real parts of λ_J^2 and λ_J^4 , we have the following four cases:

Case 1: $\lambda_A^1 > -\frac{1}{4}$, i.e. $(1 + 4\lambda_A^1) > 0$.

Then λ_J^2 is real. We have

$$\begin{aligned}\lambda_J^2 > 0 &\iff \sqrt{1 + 4\lambda_A^1} > 1 \iff \lambda_A^1 > 0 \\ \lambda_J^2 < 0 &\iff \sqrt{1 + 4\lambda_A^1} < 1 \iff \lambda_A^1 < 0 \\ \lambda_J^2 = 0 &\iff \sqrt{1 + 4\lambda_A^1} = 1 \iff \lambda_A^1 = 0\end{aligned}$$

Case 2: $\lambda_A^1 \leq -\frac{1}{4}$, i.e. $(1 + 4\lambda_A^1) \leq 0$.

Then λ_J^2 is complex, and has negative real part.

Case 3: $\lambda_A^2 > -\frac{1}{4}$, i.e. $(1 + 4\lambda_A^2) > 0$.

Then λ_J^4 is real. We have

$$\begin{aligned}\lambda_J^4 > 0 &\iff \sqrt{1 + 4\lambda_A^2} > 1 \iff \lambda_A^2 > 0 \\ \lambda_J^4 < 0 &\iff \sqrt{1 + 4\lambda_A^2} < 1 \iff \lambda_A^2 < 0 \\ \lambda_J^4 = 0 &\iff \sqrt{1 + 4\lambda_A^2} = 1 \iff \lambda_A^2 = 0\end{aligned}$$

Case 4: $\lambda_A^2 \leq -\frac{1}{4}$, i.e. $(1 + 4\lambda_A^2) \leq 0$.

Then λ_J^4 is complex, and has negative real part.

We summarize the above four cases to get the following conclusions:

Conclusion 1:

1. If A is a *stable* matrix (i.e., $\lambda_A^1 < 0$ and $\lambda_A^2 < 0$), J is also a *stable* matrix (i.e., all the eigenvalues of J have negative real parts);
2. If both eigenvalues of A are positive (i.e., $\lambda_A^1 > 0$ and $\lambda_A^2 > 0$), then two eigenvalues of J have positive real parts, and the other two eigenvalues of J have negative real parts.;
3. If one eigenvalue of A is negative and the other one is positive, then three eigenvalues of J have negative real parts and the other one has positive real part.
4. If one (both) eigenvalues of A equal(s) to zero(s), then one (two) eigenvalues of J equal(s) to zero(s).

Now we introduce a new system that has only two states \hat{x} and \hat{y} with

$$\begin{aligned}\dot{\hat{x}} &= -k(\hat{x} - b_{12x}) - g(\hat{\rho})\frac{\hat{x}}{\hat{\rho}} \\ \dot{\hat{y}} &= -k(\hat{y} - b_{12y}) - g(\hat{\rho})\frac{\hat{y}}{\hat{\rho}}\end{aligned}\tag{11}$$

It is easy to see that if equation (11) has m fixed points, say $\hat{R}_{0i}^* = (\hat{x}_{0i}^*, \hat{y}_{0i}^*)^T$, for $i = 1, \dots, m$, then equation (10) also has m fixed points, and these fixed points can be denoted as $\tilde{R}_{0i}^* = (\hat{x}_{0i}^*, \hat{y}_{0i}^*, 0, 0)^T$, for $i = 1, \dots, m$.

Furthermore, we can find that A is the stability matrix of system (11). So if we know the stabilities of all the fixed points of system (11), we can derive the stabilities of all the fixed points of system (10) by using the following two propositions.

Proposition 3.1. *The fixed point of system (10), say, $(x^*, y^*, 0, 0)$, is stable if and only if the fixed point of system (11), (x^*, y^*) , is stable.*

Proof. See Conclusion 1.

Proposition 3.2. *The fixed point of system (10), say, $(x^*, y^*, 0, 0)$, is a saddle point if and only if the fixed point of system (11), (x^*, y^*) , is an unstable node or a saddle point.*

Proof. See Conclusion 1.

Next, in section 3.1.1, we analyze the stabilities of all the fixed points of system (11), and in section 3.1.2, we use the results of section 3.1.1 and the above two propositions to derive the stabilities of all the fixed points of system (10). In section 3.1.3, we use the results of section 3.1.2 to analyze the fixed points and their stabilities of the “original” system (9).

3.1.1 Analysis of system (11)

We rewrite equation (11) in the Polar Coordinate as following

$$\begin{aligned}\dot{\hat{\rho}} &= -k\hat{\rho} + k(b_{12x} \cos \hat{\theta} + b_{12y} \sin \hat{\theta}) - g(\hat{\rho}) \\ \dot{\hat{\theta}} &= \frac{k}{\hat{\rho}}(b_{12y} \cos \hat{\theta} - b_{12x} \sin \hat{\theta})\end{aligned}\tag{12}$$

where $\hat{\rho} = \sqrt{\hat{x}^2 + \hat{y}^2}$, $\hat{\theta} \in [-\pi, \pi]$ and $\tan \hat{\theta} = \hat{y}/\hat{x}$.

We define the fixed points of (12) as $(\hat{\rho}^*, \hat{\theta}^*)^T$. Note that $\hat{\rho}^* > 0$, since $\hat{\rho}^*$ represents the relative distance between the two agents. Then the second equation of (12) gives us:

$$b_{12y} \cos \hat{\theta}^* = b_{12x} \sin \hat{\theta}^*$$

Since $b_{12x} = d$ and $b_{12y} = 0$, we have

$$\hat{\theta}^* = 0 \quad \text{or} \quad \hat{\theta}^* = -\pi$$

Case 1: $\hat{\theta}^* = 0$

In this case, the first equation of (12) tells us

$$k(d - \hat{\rho}^*) = g(\hat{\rho}^*)\tag{13}$$

Since

$$\begin{aligned}g(\rho) &= 0 \quad \text{if} \quad \rho \geq d \\ g(\rho) &< 0 \quad \text{if} \quad \rho < d\end{aligned}$$

Equation (13) has only one solution, which is $\hat{\rho}^* = d$.

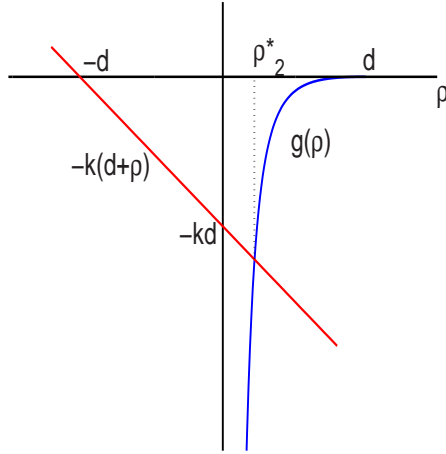


Figure 3:

Case 2: $\hat{\theta}^* = -\pi$

In this case, the first equation of (12) tells us

$$g(\hat{\rho}^*) = -k(d + \hat{\rho}^*) \quad (14)$$

Fig. 3. tells us equation (14) has only one solution, which is defined as $\hat{\rho}^* = \hat{\rho}_2^*$. So $g(\hat{\rho}_2^*) = -k(d + \hat{\rho}_2^*)$.

Summarizing both cases, we conclude that equation (12) has totally two fixed points, they are

$$(\hat{\rho}_{01}^*, \hat{\theta}_{01}^*) = (d, 0) \quad \text{and} \quad (\hat{\rho}_{02}^*, \hat{\theta}_{02}^*) = (\hat{\rho}_2^*, -\pi)$$

Next, we will check the stabilities of these two fixed points.

1. Fixed point $(\hat{\rho}_{01}^*, \hat{\theta}_{01}^*)$:

From equation (12), we get the Jacobian matrix A_1 of this fixed point as following

$$A_1 = \begin{pmatrix} -k & 0 \\ 0 & -k \end{pmatrix}$$

The eigenvalues of A_1 are $\lambda_{A_1}^1 = \lambda_{A_1}^2 = -k$. Since k is a positive constant, we conclude that the fixed point $(\hat{\rho}_{01}^*, \hat{\theta}_{01}^*)$ is a *stable node* of system (12).

2. Fixed point $(\hat{\rho}_{02}^*, \hat{\theta}_{02}^*)$:

From equation (12), we get the Jacobian matrix A_2 of this fixed point as following

$$A_1 = \begin{pmatrix} -k - g'(\hat{\rho}_2^*) & 0 \\ 0 & -k - \frac{g(\hat{\rho}_2^*)}{\hat{\rho}_2^*} \end{pmatrix}$$

where $g' = \frac{dg(\rho)}{d\rho}$. The eigenvalues of A_2 are $\lambda_{A_2}^1 = -k - g'(\hat{\rho}_2^*)$ and $\lambda_{A_2}^2 = -k - g(\hat{\rho}_2^*)/\hat{\rho}_2^*$. We know that $0 < \hat{\rho}_2^* < d$ and $g(\rho)$ is a monotonously increasing function when $0 < \rho < d$, so $g'(\hat{\rho}_2^*) > 0$ and $\lambda_2^1 < 0$. We also know that $g(\hat{\rho}_2^*) = -k(d + \hat{\rho}_2^*)$, so

$$\lambda_2^2 = k \frac{d}{\hat{\rho}_2^*} > 0$$

we conclude that the fixed point $(\hat{\rho}_{02}^*, \hat{\theta}_{02}^*)$ is a *saddle point* of system (12). The normalized stable eigenvector of A_2 is $v_{A_2}^1 = [1, 0]^T$ and the normalized unstable eigenvector of A_2 is $v_{A_2}^2 = [0, 1]^T$.

We change back to the Cartesian coordinate (equation (11)) and get

Conclusion 2:

1. The system (11) has two fixed points: $(\hat{x}_{01}^*, \hat{y}_{01}^*) = (d, 0)$ and $(\hat{x}_{02}^*, \hat{y}_{02}^*) = (-\hat{\rho}_2^*, 0)$;
2. The fixed point $(\hat{x}_{01}^*, \hat{y}_{01}^*)$ is a *stable node*;
3. The fixed point $(\hat{x}_{02}^*, \hat{y}_{02}^*)$ is a *saddle point*.

Example 1:

In this example, we set $d = 10$, $k = 1$ and define the function g as following

$$g(\rho) = \begin{cases} -k_2 \left(\frac{1}{d} - \frac{1}{\rho} \right) & \text{if } 0 < \rho < d \\ 0 & \text{if } \rho \geq d \end{cases} \quad (15)$$

where $k_2 = 100$. The two fixed points of system (12) in this example are

$$(\hat{\rho}_{01}^*, \hat{\theta}_{01}^*) = (10, 0) \quad \text{and} \quad (\hat{\rho}_{02}^*, \hat{\theta}_{02}^*) = (2.2241, -\pi)$$

The Fixed point $(10, 0)$ is a stable node since $A_1 = -I$ and $\lambda_{A_1}^1 = \lambda_{A_1}^2 = -1$. The fixed point $(2.2241, -\pi)$ is a saddle point since $\lambda_{A_2}^1 = -15.1367$ and $\lambda_{A_2}^2 = 4.4963$.

Fig. 4 shows us the phase portrait of the nonlinear system in this example. It can be seen that the stable manifold of the saddle point $(2.2241, -\pi)$ is just a line defined by $\hat{\theta} = -\pi$.

We change back to the Cartesian coordinate (equation (11)) and conclude that

1. The system (11) has two fixed points, $(\hat{x}_{01}^*, \hat{y}_{01}^*) = (10, 0)$ and $(\hat{x}_{02}^*, \hat{y}_{02}^*) = (-2.2241, 0)$;

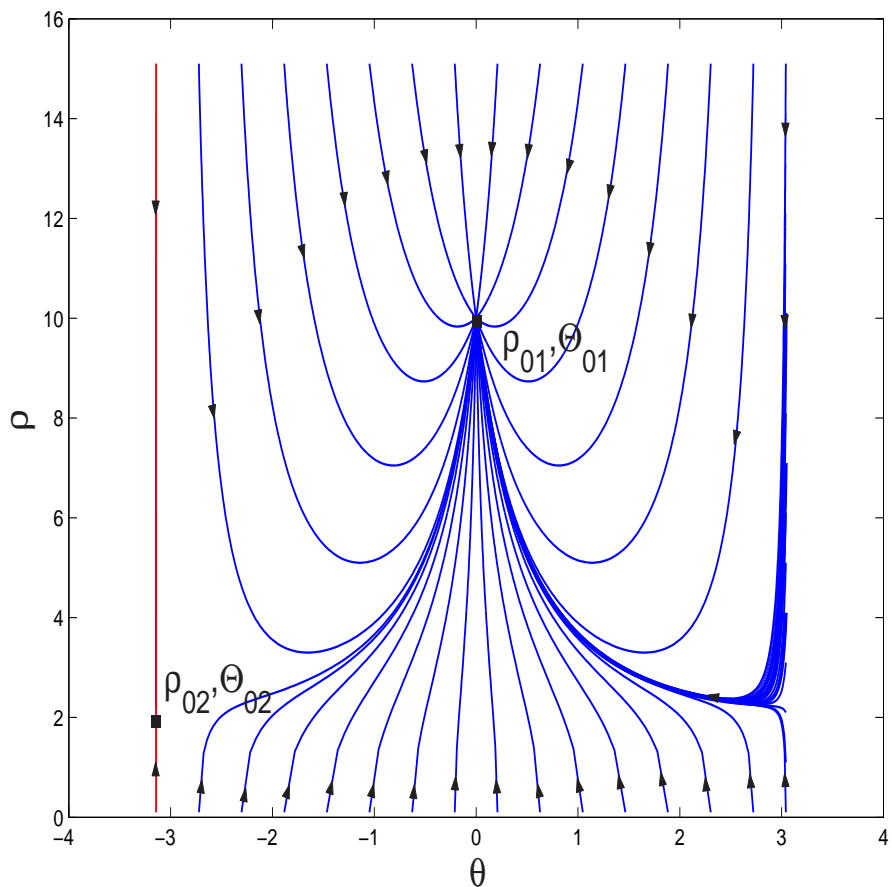


Figure 4: The phase portrait of system (12)

2. The fixed point $(\hat{x}_{01}^*, \hat{y}_{01}^*)$ is a *stable node*;
3. The fixed point $(\hat{x}_{02}^*, \hat{y}_{02}^*)$ is a *saddle point*. The stable manifold of this saddle point is the half-line defined by $\hat{y} = 0$ and $\hat{x} < 0$.

Next, we will use “Bendixson’s criterion” to check whether the system (11) has periodic solutions or not in this example. In fact, from the phase portrait (Fig. 4), we can guess that the answer is “no”.

The divergence of the vector field of system (11) is

$$\frac{\partial \dot{x}}{\partial \hat{x}} + \frac{\partial \dot{y}}{\partial \hat{y}} = -2k - g'(\hat{\rho}) - \frac{g(\hat{\rho})}{\hat{\rho}}$$

Since in this example, we have

$$\begin{aligned} g'(\hat{\rho}) &= \begin{cases} 2k_2 \frac{d - \rho}{d\rho^3} & \text{if } 0 < \rho < d \\ 0 & \text{if } \rho \geq d \end{cases} \\ g(\hat{\rho}) &= \begin{cases} -k_2 \frac{(d - \rho)^2}{d^2 \rho^2} & \text{if } 0 < \rho < d \\ 0 & \text{if } \rho \geq d \end{cases} \end{aligned}$$

So

$$\frac{\partial \dot{x}}{\partial \hat{x}} + \frac{\partial \dot{y}}{\partial \hat{y}} = \begin{cases} -2k - k_2 \frac{d^2 - \hat{\rho}^2}{d^2 \hat{\rho}^3} & \text{if } 0 < \rho < d \\ -2k & \text{if } \rho \geq d \end{cases}$$

The periodic solutions are not possible for the system (11) in this example, since the divergence of the vector field is always negative.

3.1.2 Analysis of system (10)

From Conclusion 2, Proposition 3.1 and 3.2, we have the following results about the fixed points of system (10):

Conclusion 3:

1. The system (10) has two fixed points: $(\tilde{x}_{01}^*, \tilde{y}_{01}^*, \tilde{v}_{x01}^*, \tilde{v}_{y01}^*) = (d, 0, 0, 0)$ and $(\tilde{x}_{02}^*, \tilde{y}_{02}^*, \tilde{v}_{x02}^*, \tilde{v}_{y02}^*) = (-\hat{\rho}_2^*, 0, 0, 0)$;
2. The fixed point $(\tilde{x}_{01}^*, \tilde{y}_{01}^*, \tilde{v}_{x01}^*, \tilde{v}_{y01}^*)$ is stable;
3. The fixed point $((\tilde{x}_{02}^*, \tilde{y}_{02}^*, \tilde{v}_{x02}^*, \tilde{v}_{y02}^*))$ is a *saddle point*.

Furthermore, we know that three of the four eigenvalues of the Jacobian matrix of the fixed point $(\tilde{x}_{02}^*, \tilde{y}_{02}^*, \tilde{v}_{x02}^*, \tilde{v}_{y02}^*)$ have negative real parts, so the stable manifold of this saddle point are three dimensional, and hard to calculate.

However in the real world, we do not need to care about this saddle point if we assume that this system always has some small 4-dimensional perturbations, which is a reasonable assumption for this system.

Since system (10) is a 4-dimensional system, it is difficult to check the existence of its periodic solutions analytically. However by doing a lots of simulations, we conclude that system (10) has no periodic solutions.

3.1.3 Analysis of system (9)

In this section, we analyze the fixed points and their stabilities of the “original” system (9) by using some results of section 3.1.2.

We look at the system (9) again:

$$\begin{aligned}\dot{\tilde{x}}_1 &= \tilde{v}_{1x} \\ \dot{\tilde{y}}_1 &= \tilde{v}_{1y} \\ \dot{\tilde{x}}_2 &= \tilde{v}_{2x} \\ \dot{\tilde{y}}_2 &= \tilde{v}_{2y} \\ \dot{\tilde{v}}_{1x} &= -k(\tilde{x}_1 - b_{1x}) + g(\tilde{\rho}) \frac{\tilde{x}_2 - \tilde{x}_1}{\tilde{\rho}} - \tilde{v}_{1x} \\ \dot{\tilde{v}}_{1y} &= -k(\tilde{y}_1 - b_{1y}) + g(\tilde{\rho}) \frac{\tilde{y}_2 - \tilde{y}_1}{\tilde{\rho}} - \tilde{v}_{1y} \\ \dot{\tilde{v}}_{2x} &= -k(\tilde{x}_2 - b_{2x}) + g(\tilde{\rho}) \frac{\tilde{x}_1 - \tilde{x}_2}{\tilde{\rho}} - \tilde{v}_{2x} \\ \dot{\tilde{v}}_{2y} &= -k(\tilde{y}_2 - b_{2y}) + g(\tilde{\rho}) \frac{\tilde{y}_1 - \tilde{y}_2}{\tilde{\rho}} - \tilde{v}_{2y}\end{aligned}$$

Defining $\bar{x} = \frac{\tilde{x}_1 + \tilde{x}_2}{2}$, $\bar{y} = \frac{\tilde{y}_1 + \tilde{y}_2}{2}$, $\bar{v}_x = \frac{\tilde{v}_{1x} + \tilde{v}_{2x}}{2}$ and $\bar{v}_y = \frac{\tilde{v}_{1y} + \tilde{v}_{2y}}{2}$, we have

$$\begin{aligned}\dot{\bar{x}} &= \bar{v}_x \\ \dot{\bar{y}} &= \bar{v}_y \\ \dot{\bar{v}}_x &= -k\bar{x} - \bar{v}_x \\ \dot{\bar{v}}_y &= -k\bar{y} - \bar{v}_y\end{aligned}\tag{16}$$

System (16) is a linear system and its only one fixed point is $(\bar{x}^*, \bar{y}^*) = (0, 0)$. The stability

matrix of this system is

$$A_3 = \begin{pmatrix} 0 & 0 & 1 & 0 \\ 0 & 0 & 0 & 1 \\ -k & 0 & -1 & 0 \\ 0 & -k & 0 & -1 \end{pmatrix}$$

We can find the eigenvalues of A_3 are

$$\begin{aligned} \lambda_{A_3}^1 = \lambda_{A_3}^3 &= -\frac{1}{2} - \frac{1}{2}\sqrt{1-4k} \\ \lambda_{A_3}^2 = \lambda_{A_3}^4 &= -\frac{1}{2} + \frac{1}{2}\sqrt{1-4k} \end{aligned}$$

It is easy to show that all the eigenvalues of A_3 have negative real parts, since $k > 0$. This shows that the only one fixed point $(\bar{x}^*, \bar{y}^*) = (0, 0)$ of system (16) is globally, asymptotically stable.

Since, from (16), we have

$$\begin{cases} \dot{\tilde{x}}_1^* + \dot{\tilde{x}}_2^* = 0 \\ \dot{\tilde{y}}_1^* + \dot{\tilde{y}}_2^* = 0 \\ \dot{\tilde{v}}_{1x}^* + \dot{\tilde{v}}_{2x}^* = 0 \\ \dot{\tilde{v}}_{1y}^* + \dot{\tilde{v}}_{2y}^* = 0 \end{cases} \iff \begin{cases} \tilde{x}_1^* + \tilde{x}_2^* = 0 \\ \tilde{y}_1^* + \tilde{y}_2^* = 0 \\ \tilde{v}_{1x}^* + \tilde{v}_{2x}^* = 0 \\ \tilde{v}_{1y}^* + \tilde{v}_{2y}^* = 0 \end{cases}$$

and, from (10), we have

$$\begin{cases} \dot{\tilde{x}}_1^* - \dot{\tilde{x}}_2^* = 0 \\ \dot{\tilde{y}}_1^* - \dot{\tilde{y}}_2^* = 0 \\ \dot{\tilde{v}}_{1x}^* - \dot{\tilde{v}}_{2x}^* = 0 \\ \dot{\tilde{v}}_{1y}^* - \dot{\tilde{v}}_{2y}^* = 0 \end{cases} \iff \begin{cases} \tilde{x}_1^* - \tilde{x}_2^* = d \\ \tilde{y}_1^* - \tilde{y}_2^* = 0 \\ \tilde{v}_{1x}^* - \tilde{v}_{2x}^* = 0 \\ \tilde{v}_{1y}^* - \tilde{v}_{2y}^* = 0 \end{cases}$$

or

$$\begin{cases} \dot{\tilde{x}}_1^* - \dot{\tilde{x}}_2^* = 0 \\ \dot{\tilde{y}}_1^* - \dot{\tilde{y}}_2^* = 0 \\ \dot{\tilde{v}}_{1x}^* - \dot{\tilde{v}}_{2x}^* = 0 \\ \dot{\tilde{v}}_{1y}^* - \dot{\tilde{v}}_{2y}^* = 0 \end{cases} \iff \begin{cases} \tilde{x}_1^* - \tilde{x}_2^* = -\hat{\rho}_2^* \\ \tilde{y}_1^* - \tilde{y}_2^* = 0 \\ \tilde{v}_{1x}^* - \tilde{v}_{2x}^* = 0 \\ \tilde{v}_{1y}^* - \tilde{v}_{2y}^* = 0 \end{cases}$$

So we have

$$\begin{cases} \dot{\tilde{x}}_1^* = 0 \\ \dot{\tilde{x}}_2^* = 0 \\ \dot{\tilde{y}}_1^* = 0 \\ \dot{\tilde{y}}_2^* = 0 \\ \dot{\tilde{v}}_{1x}^* = 0 \\ \dot{\tilde{v}}_{2x}^* = 0 \\ \dot{\tilde{v}}_{1y}^* = 0 \\ \dot{\tilde{v}}_{2y}^* = 0 \end{cases} \iff \begin{cases} \tilde{x}_1^* = \frac{d}{2} \\ \tilde{x}_2^* = -\frac{d}{2} \\ \tilde{y}_1^* = 0 \\ \tilde{y}_2^* = 0 \\ \tilde{v}_{1x}^* = 0 \\ \tilde{v}_{2x}^* = 0 \\ \tilde{v}_{1y}^* = 0 \\ \tilde{v}_{2y}^* = 0 \end{cases}$$

or

$$\begin{cases} \dot{\tilde{x}}_1^* = 0 \\ \dot{\tilde{x}}_2^* = 0 \\ \dot{\tilde{y}}_1^* = 0 \\ \dot{\tilde{y}}_2^* = 0 \\ \dot{\tilde{v}}_{1x}^* = 0 \\ \dot{\tilde{v}}_{2x}^* = 0 \\ \dot{\tilde{v}}_{1y}^* = 0 \\ \dot{\tilde{v}}_{2y}^* = 0 \end{cases} \iff \begin{cases} \tilde{x}_1^* = -\frac{\hat{\rho}_2^*}{2} \\ \tilde{x}_2^* = \frac{\hat{\rho}_2^*}{2} \\ \tilde{y}_1^* = 0 \\ \tilde{y}_2^* = 0 \\ \tilde{v}_{1x}^* = 0 \\ \tilde{v}_{2x}^* = 0 \\ \tilde{v}_{1y}^* = 0 \\ \tilde{v}_{2y}^* = 0 \end{cases}$$

i.e. system (9) has only two fixed points, $R_1^* = (\tilde{x}_1^*, \tilde{x}_2^*, \tilde{y}_1^*, \tilde{y}_2^*, \tilde{v}_{1x}^*, \tilde{v}_{2x}^*, \tilde{v}_{1y}^*, \tilde{v}_{2y}^*)^T = (\frac{d}{2}, -\frac{d}{2}, 0, 0, 0, 0, 0, 0)^T$ and $R_2^* = (\tilde{x}_1^*, \tilde{x}_2^*, \tilde{y}_1^*, \tilde{y}_2^*, \tilde{v}_{1x}^*, \tilde{v}_{2x}^*, \tilde{v}_{1y}^*, \tilde{v}_{2y}^*)^T = (-\frac{\hat{\rho}_2^*}{2}, \frac{\hat{\rho}_2^*}{2}, 0, 0, 0, 0, 0, 0)^T$. From the results of section 3.1.2, we know that the fixed point $(\frac{d}{2}, -\frac{d}{2}, 0, 0, 0, 0, 0, 0)^T$ is stable and the fixed point $(-\frac{\hat{\rho}_2^*}{2}, \frac{\hat{\rho}_2^*}{2}, 0, 0, 0, 0, 0, 0)^T$ is unstable (a saddle point).

Next, assuming the system (9) always has some small 4-dimensional perturbations, we use a Lyapunov function to show that every solution of this system converges to its stable fixed point.

Denoting the state of system (9) as $R = (\tilde{r}_1, \tilde{r}_2, \tilde{v}_1, \tilde{v}_2)^T$, we define a Lyapunov function $V(R)$ for the stable fixed point R_1^* as following

$$V(R) = \frac{1}{2} \sum_{i=1}^2 \left(\tilde{v}_i^T \tilde{v}_i + 2 \int_0^{\|\tilde{r}_i - b_i\|} f(\sigma) d\sigma + \sum_{j \in N_i(t)} \int_d^{\|\tilde{r}_j - \tilde{r}_i\|} g(\sigma) d\sigma \right) \quad (17)$$

It is known that $V(R_1^*) = 0$ and $V(R) > 0$, for $R \neq R_1^*$. The derivative of V with respect to time is

$$\begin{aligned} \dot{V}(R) &= \sum_{i=1}^2 \left(\tilde{v}_i^T \dot{\tilde{v}}_i + f(\|\tilde{r}_i - b_i\|) \frac{(\tilde{r}_i - b_i)^T}{\|\tilde{r}_i - b_i\|} \tilde{v}_i + \frac{1}{2} \sum_{j \in N_i} g(\|\tilde{r}_j - \tilde{r}_i\|) \frac{(\tilde{r}_j - \tilde{r}_i)^T}{\|\tilde{r}_j - \tilde{r}_i\|} (\tilde{v}_j - \tilde{v}_i) \right) \\ &= \sum_{i=1}^2 \tilde{v}_i^T \left(\dot{\tilde{v}}_i + f(\|\tilde{r}_i - b_i\|) \frac{\tilde{r}_i - b_i}{\|\tilde{r}_i - b_i\|} - \sum_{j \in N_i} g(\|\tilde{r}_j - \tilde{r}_i\|) \frac{(\tilde{r}_j - \tilde{r}_i)^T}{\|\tilde{r}_j - \tilde{r}_i\|} \right) \\ &= \sum_{i=1}^2 \tilde{v}_i^T (-\tilde{v}_i) \\ &= -\sum_{i=1}^2 \|\tilde{v}_i\|^2 \end{aligned} \quad (18)$$

where in the second step, we use the fact that

$$\begin{aligned}
& g(\|\tilde{r}_j - \tilde{r}_i\|) \frac{(\tilde{r}_j - \tilde{r}_i)^T}{\|\tilde{r}_j - \tilde{r}_i\|} (\dot{\tilde{r}}_j - \dot{\tilde{r}}_i) \\
&= -g(\|\tilde{r}_j - \tilde{r}_i\|) \frac{(\tilde{r}_j - \tilde{r}_i)^T}{\|\tilde{r}_j - \tilde{r}_i\|} \dot{\tilde{r}}_i + g(\|\tilde{r}_j - \tilde{r}_i\|) \frac{(\tilde{r}_j - \tilde{r}_i)^T}{\|\tilde{r}_j - \tilde{r}_i\|} \dot{\tilde{r}}_j \\
&= -g(\|\tilde{r}_j - \tilde{r}_i\|) \frac{(\tilde{r}_j - \tilde{r}_i)^T}{\|\tilde{r}_j - \tilde{r}_i\|} \dot{\tilde{r}}_i - g(\|\tilde{r}_i - \tilde{r}_j\|) \frac{(\tilde{r}_i - \tilde{r}_j)^T}{\|\tilde{r}_i - \tilde{r}_j\|} \dot{\tilde{r}}_j
\end{aligned}$$

From equation (18), we know that $\dot{V}(R) \leq 0$ and $\dot{V}(R) = 0$ if and only if $\tilde{v}_i = 0$, $i = 1, 2$. Defining $E = \left\{ R \in \mathbb{R}^8 \mid \dot{V}(R) = 0 \right\}$ and assuming that the system (9) always has some small 4-dimensional perturbations, then we can say that E does not contain any other solutions, other than R_1^* , that remain forever in E . Note that $V(R) \rightarrow \infty$ as $R \rightarrow \infty$. From the Krasovskii's theorem, we can say that every solution of the system (9) converges asymptotically to R_1^* .

Since $\tilde{r}_i = r_i - r_0$ and $\tilde{v}_i = v_i - q$, $i = 1, 2$, we have $r_1 \rightarrow (\frac{d}{2}, 0)^T + r_0 = r_{1d}$, $r_2 \rightarrow (-\frac{d}{2}, 0)^T + r_0 = r_{2d}$, $v_1 \rightarrow q$ and $v_2 \rightarrow q$, i.e. under the influence of the *attractive* and *repulsive* forces, each agent will move asymptotically close to its virtual leader. After each agent “catches” its virtual leader, the formation of this agent group becomes the desired formation and will not change, the velocities of these agents are same and equal to q , i.e. the velocity of the virtual leaders.

3.2 Simulation result

In this section, we use the setting in Example 1, i.e. $N = 2$, $b_1 = (d/2, 0)^T$, $b_2 = (-d/2, 0)^T$, $d = 10$, $k = 1$, $k_2 = 100$ and

$$g(\rho) = \begin{cases} -k_2 \left(\frac{1}{d} - \frac{1}{\rho} \right) & \text{if } 0 < \rho < d \\ 0 & \text{if } \rho \geq d \end{cases}$$

to simulate system (9). We also set $q = (2, 3)^T$.

In each one of the first two simulations, the initial condition of the agents is given by a set of N random initial positions, (uniform distributions in the area 30×30), and zero initial velocities. In each figure, the stars denote the agents, the circle denotes the virtual leader, the dash-dot line denotes the desired path, the red (blue) solid line denotes the trajectory or speed of agent 1(agent 2).

In the first simulation, the initial condition is

$$(x_{10}, x_{20}, y_{10}, y_{20}, v_{1x0}, v_{2x0}, v_{1y0}, v_{2y0}) = (1.7367, 10.5860, 24.3950, 0.2958, 0, 0, 0, 0)$$

Fig. 5 shows the trajectories of both agents and the desired path. Fig. 6 shows the speeds of both agents.

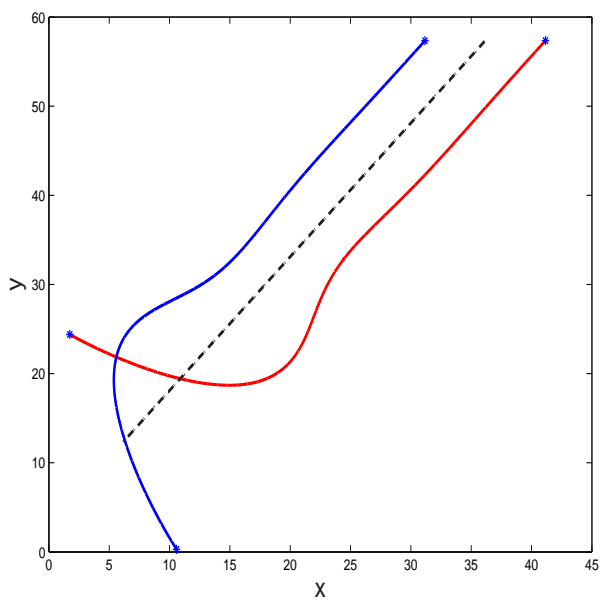


Figure 5:

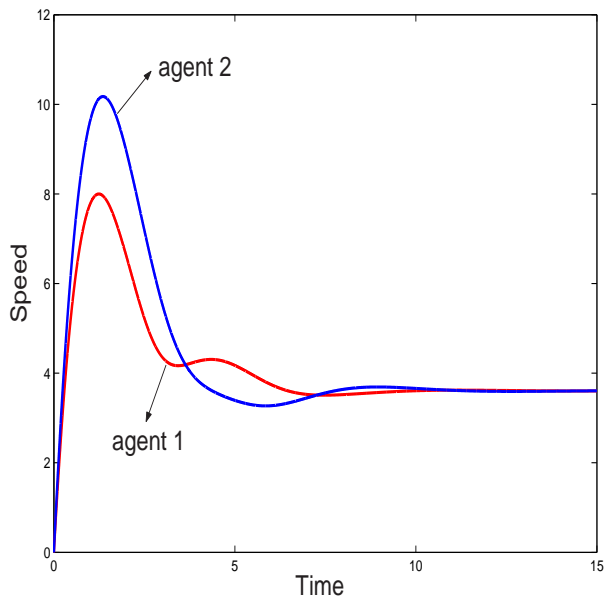


Figure 6:

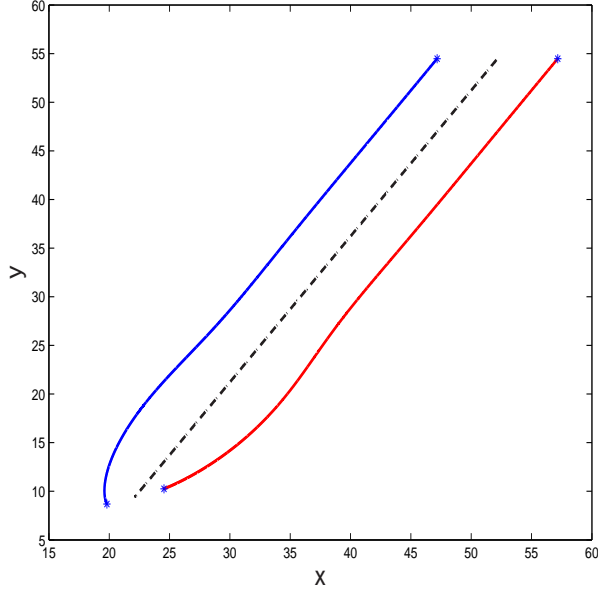


Figure 7:

In the second simulation, the initial condition is

$$(x_{10}, x_{20}, y_{10}, y_{20}, v_{1x0}, v_{2x0}, v_{1y0}, v_{2y0}) = (24.5392, 19.8068, 10.2591, 8.6918, 0, 0, 0, 0)$$

Fig. 7 shows the trajectories of both agents and the desired path. Fig. 8 shows the speeds of both agents.

In the third simulation, the initial condition is

$$(x_{10}, x_{20}, y_{10}, y_{20}, v_{1x0}, v_{2x0}, v_{1y0}, v_{2y0}) = (15, 40, 30, 40, 0, 0, 0, 0)$$

which is on the stable manifold of the saddle point, since $(x_{10} - x_{20}) < 0$ and $y_{10} - y_{20} = 0$. Fig. 9 shows the trajectories of both agents and the desired path. Fig. 10 shows the speeds of both agents. Since there is some numerical error in computation (I used “ode45” in “Matlab”), though the agents start from the stable manifold of the saddle point, they still converge to the stable fixed point.

References

- [1] C. Reynolds, “Flocks, herds, and schools: A distributed behavioral model,” in *Computer Graphics*, 21(4) (SIGGRAPH ’87 Conference Proceedings), pp. 25-34.
- [2] A. Okubo, “Dynamical aspects of animal grouping: swarms, schools, flocks, and herds,” *Advances in Biophysics*, vol. 22, 1986, pp 1-94.

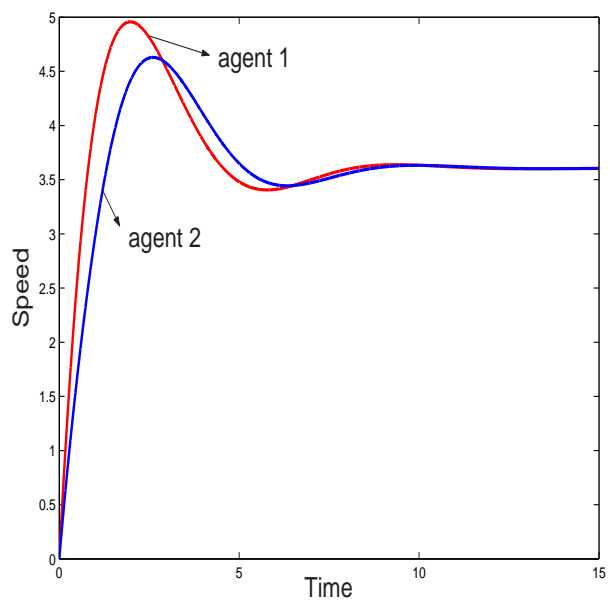


Figure 8:

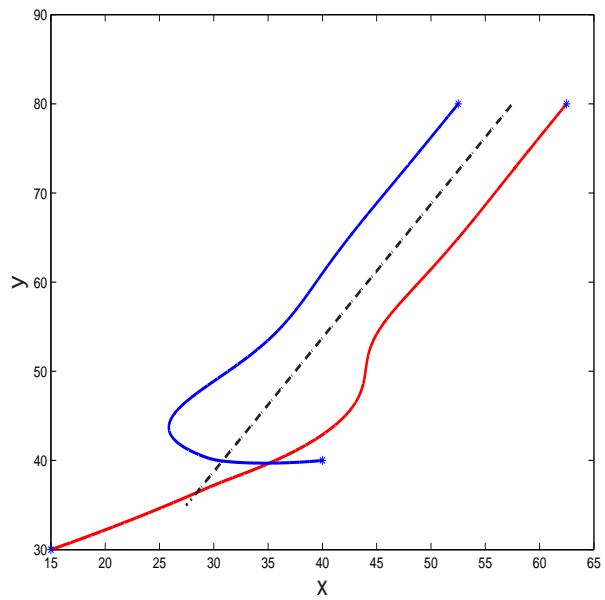


Figure 9:

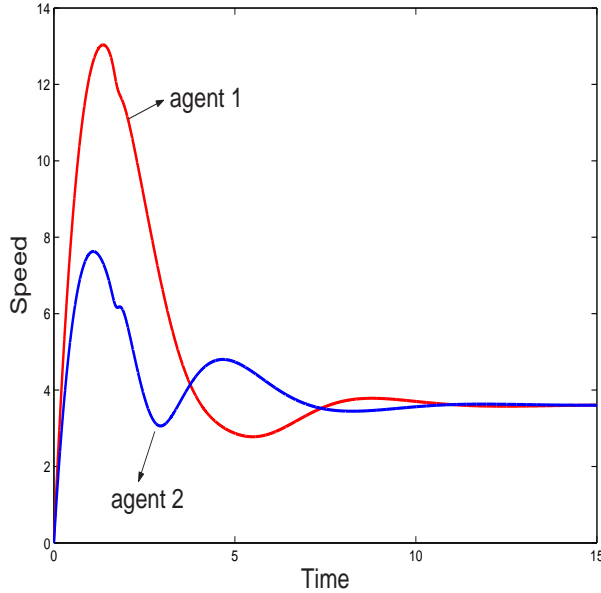


Figure 10:

- [3] G. Flierl, D. Grunbaum, S. Levin and D. Olson, “From individuals to aggregations: the interplay between behavior and physics,” *Journal of Theoretical Biology*, vol. 196(4), 1999, pp 397-454.
- [4] T. Vicsek, A. Czirok, E. Ben-Jacob, I. Cohen and O. Shochet, “Novel type of phase transition in a system of self-driven particles,” *Physical Review Letters*, vol. 75, 1995, pp 1226-1229.
- [5] A. Jadbabaie, J. Lin and A. S. Morse, “Coordination of groups of mobile autonomous agents using nearest neighbor rules,” *IEEE Trans. on Automatic Control*, vol. 48(6), 2003, pp 988-1001.
- [6] N. Leonard and E. Fiorelli, “Virtual leaders, artificial potentials and coordinated control of groups,” *Proc. of the 40th IEEE Conference on Decision and Control*, Orlando, Florida, 2001, pp 2968-2973.
- [7] P. Ogren, E. Fiorelli and N. Leonard, “Formations with a mission: stable coordination of vehicle group maneuvers,” *Proc. 15th International Symposium on Mathematical Theory of Networks and Systems*, Indiana, 2002.
- [8] R. Olfati-Saber and R. M. Murray, “Consensus problems in networks of agents with switching topology and time-delays,” *The IEEE Trans. on Automatic Control*, vol. 49, 2004, pp 1520-1533.

- [9] V. Gazi and K.M. Passino, "Stability analysis of swarms," *IEEE Transactions on Automatic Control*, vol. 48(4), 2003, pp 692-697.
- [10] V. Gazi and K.M. Passino, "Stability analysis of social foraging swarms," *IEEE Transactions on Systems, Man, and Cybernetics-Part B: Cybernetics*, vol. 34(1), 2004, pp 539-557.
- [11] M. Egerstedt and X. Hu, "Formation constrained multi-agent control," *IEEE Transactions on Robotics and Automation*, vol. 17(6), 2001, pp 947-951.
- [12] R. Alami, S. Fleury, M. Herrb, F. Ingrand and F. Robert, "Multi robot cooperation in the Martha project," *IEEE Robotics and Automation Magazine*, vol. 5(1), 1998, pp 36-47.

Final Project in ENME 665: Advanced Topics In Vibrations

Author: Jacob Ajslev Hersboell

Instructor: Professor B. Balachandran

May 17, 2007

Introduction and model description

In this project we consider a beam system. A model of the system can be viewed below

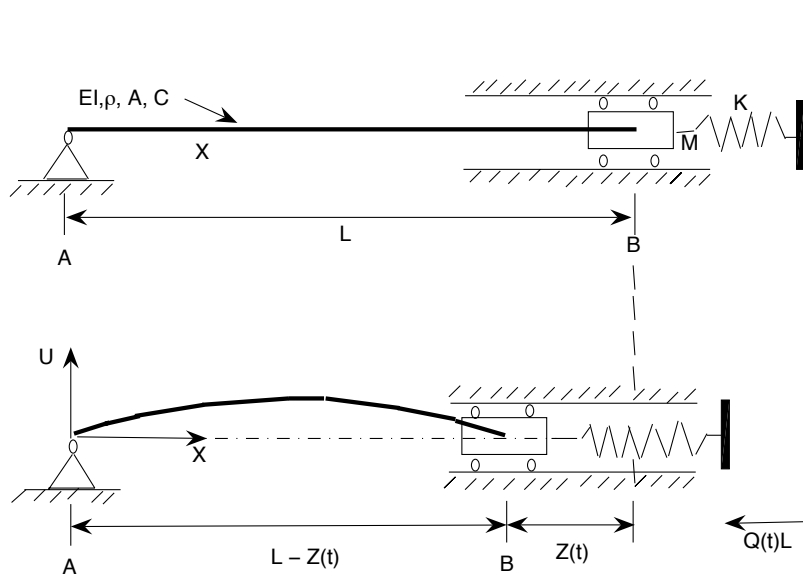


Figure 1: Illustration of the beam system in undeformed and deformed state

At the top is an illustration of the undeformed system and at the bottom is seen an illustration of the system deformed to the left. At this point it should be mentioned that the size of the coordinate $Z(t)$ is largely exaggerated. The beam is simply supported in A and B, is made of linear elastic material, has length L , bending stiffness EI and mass per. length ρA . Transverse deflection is described by $U(X, t)$, where X denotes the coordinate along the length of the axis and t describes time. Stretching of the beam axis is neglected and rotation of segments of the beam is sufficiently small that $\kappa = U''(X, t)$ is a good approximation, where κ describes the curvature of the beam and $(\cdot)' \equiv \frac{\partial}{\partial X}$. Dissipation of energy is modeled as internal viscous damping which implies that the internal bending moment can be modeled as $\tau(X, t) = EI\kappa + CEI\dot{\kappa}$, where $(\cdot) \equiv \frac{\partial}{\partial t}$ and C is the attenuation coefficient of the damping.

The support at B is moveable along the horizontal direction along X and is connected to a fixed boundary through a rigid body modeled as a point mass M and a linear massless spring with stiffness K . The coordinate of this support is denoted by $Z(t)$, measured from the undeformed state. The right endpoint of the spring is denoted by the coordinate $Q(t)L$ and is measured from a fixed right boundary. $Q(t)$ is modeled by $Q(t) = Q_0 + Q_1 \cos(\Omega t)$

where Q_0 , Q_1 and Ω is the control parameters. Note that Q_O can take positive as well as negative values. The compression of the spring is given by $Q(t)L - Z(t)$.

Contents

1 Mathematical model	6
1.1 a) Determination of the coordinate $Z(t)$	6
1.2 b) Partiel differential equation for finite small deflections of the beam	7
1.3 c) Linear expression of the reaction forces at A and B	10
2 Eigenvalue problem, natural frequency and free modes	11
2.1 a) Eigenvalue problem (EVP)	11
2.2 b) Investigation of the EVP	11
2.3 c) Rayleigh quotient $R[u_j]$	13
2.4 d) Eigenvalues and free modes	14
3 Discretized model, free mode expansion	16
3.1 a) Free mode expansion	16
3.2 b) Primary resonance	18
3.3 c) Approximation to the dynamical response of the beam	19
4 Local analysis of the system under static load	20
4.1 a) First order system, stationary points, there stability classification and the flow in the phase plane	20
4.1.1 $(y^*, v^*) = (0, 0)$	21
4.1.2 $(y^*, v^*) = \left(\sqrt{\frac{-\omega^2}{\gamma}}, 0\right)$ \wedge $(y^*, v^*) = \left(-\sqrt{\frac{-\omega^2}{\gamma}}, 0\right)$	22
4.2 b) Bifurcation in then parameter space	23
5 Quantitative analysis of the system under dynamical load	25
5.1 a) $\omega^2 > 0$	25
5.2 b) $\omega^2 < 0$	30
6 Applying high-frequency input to control the beam stiffness	34
7 Simulation program	36
8 Numerical analysis	37
8.1 a)	37
8.2 b)	38
8.3 c)	39
8.4 d)	40
8.5 e)	41
9 Conclusion	44

10 Appendix A, list of sources	45
11 Appendix B, source code for the simulation program	46

1 Mathematical model

1.1 a) Determination of the coordinate $Z(t)$

First I want to show that the coordinate $Z(t)$ can be approximated by

$$Z(t) \approx \frac{1}{2} \int_0^L (U')^2 dX \quad \text{for } U' \ll 1 \quad (1.1)$$

From the mathematical analysis it is known that the length, \mathcal{L} , for a certain curve, \mathcal{S} described in a Cartesian coordinate system in two dimension is given by

$$\mathcal{L} = \int_{\mathcal{S}} \sqrt{1 + (U')^2} dX \quad (1.2)$$

where $U' \equiv \frac{\partial U}{\partial x}$.

By carrying out a Tayler expansion of $\sqrt{1 + (U')^2}$ to higher order we get

$$\sqrt{1 + (U')^2} = 1 + \frac{1}{2}(U')^2 + \mathcal{O}(U')^4. \quad (1.3)$$

By that it is seen that the length of the curve \mathcal{S} , can be written on the form

$$\mathcal{L} = \int_S \left(1 + \frac{1}{2}(U')^2 + \mathcal{O}(U')^4\right) dX. \quad (1.4)$$

By considering the illustration of the undeformed system it is seen that $\mathcal{L} = L$ and the boundary conditions are given such that the integral becomes

$$L = \int_0^{L-Z(t)} \left(1 + \frac{1}{2}(U')^2 + \mathcal{O}(U')^4\right) dX \Leftrightarrow \quad (1.5)$$

$$L = L - Z(t) + \int_0^{L-Z(t)} \left(\frac{1}{2}(U')^2 + \mathcal{O}(U')^4\right) dX \Leftrightarrow \quad (1.6)$$

$$Z(t) = \int_0^{L-Z(t)} \left(\frac{1}{2}(U')^2 + \mathcal{O}(U')^4\right) dX. \quad (1.7)$$

By neglecting terms of order $\mathcal{O}(U')^4$ and higher we find the following

$$Z(t) \approx \frac{1}{2} \int_0^{L-Z(t)} (U')^2 dX. \quad (1.8)$$

The approximation is excellent if we assume that $U' \ll 1$ because $\mathcal{O}(U')^4 \ll 1$.

Moreover, the upper boundary condition is being approximated by $L - Z(t)$ til L , which is justifiable since $U' \ll 1$ and by that $Z(t) \ll L$. It is then shown that

$$Z(t) \approx \frac{1}{2} \int_0^L (U')^2 dX \quad \text{for } U' \ll 1 \quad (1.9)$$

1.2 b) Partiel differential equation for finite small deflections of the beam

I now want to show that finite small deflections of the beam is modeled by

$$\ddot{u} + \frac{CEI}{\rho AL^4} \dot{u}''' + \frac{EI}{\rho AL^4} u''''' + \left[\frac{K}{\rho AL} \left(Q_0 + Q_1 \cos(\Omega t) - \frac{1}{2} \int_0^1 (u')^2 dx \right) - \frac{M}{\rho AL} \int_0^1 \left(u' \ddot{u}' + (\dot{u}')^2 \right) dx \right] u'' = 0 \quad (1.10)$$

with boundary conditions

$$u(0, t) = u''(0, t) = u(1, t) = u''(1, t) = 0 \quad (1.11)$$

hvor $u = u(x, t)$, $u = \frac{U}{L}$, $x = \frac{X}{L} \in [0, 1]$, $(u')^2 \ll 1$, $(\cdot)' \equiv \frac{\partial}{\partial t}$ and $(\cdot)' \equiv \frac{\partial}{\partial x}$

Below is seen an illustration of an differential element of the beam under deformation. Stress resultants together with moments are indicated using traditional sign convention. Also an illustration of the free body diagram of the mass, M is shown



Figure 2: Illustration of a differential beam element together with a free body diagram of the mass M

By applying the conditions of equilibrium (static equilibrium in the horizontal direction, static equilibrium in the direction orthogonal to the paper and the sum of moments about a line orthogonal to the paper is equal to zero) we arrive at these three equations

$$(N + dN) - N = 0 \Rightarrow N' = 0 \quad (1.12)$$

$$(T + dT) - T = \rho A dX \ddot{U} \Rightarrow T' = \rho A \ddot{U} \quad (1.13)$$

$$(\tau + d\tau) - \tau + T dX - N dU = 0 \Rightarrow \tau' + T - N U' = 0 \quad (1.14)$$

Applying the chain rule of differentiation these three equations can be combined to

$$\tau'' + \rho A \ddot{U} - N U'' = 0 \quad (1.15)$$

As mentioned in the introduction the internal bending moment could be expressed by $\tau = EI\kappa + CEI\dot{\kappa}$, and that $\kappa \equiv U''$. This gives

$$\tau = EI\kappa + CEI\dot{\kappa} \Rightarrow \tau'' = EI\kappa'' + CEI\dot{\kappa}'' \quad (1.16)$$

$$\kappa \equiv U'' \Rightarrow \kappa'' \equiv U''' \Rightarrow \quad (1.17)$$

$$\tau'' = EIU''' + CEI\dot{U}''' \quad (1.18)$$

If we insert (1.18) into (1.15) we get

$$EIU''' + CEI\dot{U}''' + \rho A\ddot{U} - NU'' = 0 \quad (1.19)$$

If we consider the free body diagram for M we conclude that the equilibrium in the horizontal direction is given by

$$M\ddot{Z} = N - K(Z - Q(t)L) \Rightarrow \quad (1.20)$$

$$N = M\ddot{Z} + K(Z - Q(t)L) = M\ddot{Z} - K(Q(t)L - Z). \quad (1.21)$$

By inserting (1.21) in (1.19) we get

$$EIU''' + CEI\dot{U}''' + \rho A\ddot{U} - (M\ddot{Z} - K(Q(t)L - Z))U'' = 0. \quad (1.22)$$

The aim is now to normalize this partial differential equation by applying the above introduce variables $u = u(x, t)$, $u = \frac{U}{L}$, $x = \frac{X}{L} \in [0, 1]$, $(u')^2 \ll 1$, $()' \equiv \frac{\partial}{\partial x}$, $() \equiv \frac{\partial}{\partial t}$. Furthermore we put " \equiv " i (1.9) to " $=$ ", which is justifiable since $(u')^2 \ll 1$

We then get

$$U''' = \frac{L}{L^4}u''' \quad (1.23)$$

$$\dot{U}''' = \frac{L}{L^4}u''' \quad (1.24)$$

$$U'' = \frac{L}{L^2}u'' \quad (1.25)$$

$$U' = u' \quad (1.26)$$

$$\rho A\ddot{U} = \rho AL\ddot{u} \quad (1.27)$$

$$dx = \frac{dX}{L} \quad (1.28)$$

$$Z = \frac{1}{2} \int_0^L (U')^2 dX = \frac{1}{2} L \int_0^1 (u')^2 dx \Rightarrow \quad (1.29)$$

$$\dot{Z} = L \int_0^1 \dot{u}' u' dx \Rightarrow \ddot{Z} = L \int_0^1 (\dot{u}' u'' + (\dot{u}')^2) dx \quad (1.30)$$

By inserting (1.23)-(1.30) in (1.22) and normalize by ρA we find

$$\frac{EI}{\rho AL^4}u'''' + \frac{CEI}{\rho AL^4}\dot{u}'''' + \ddot{u} + \left[\frac{K}{\rho AL} \left(Q(t) - \frac{1}{2} \int_0^1 (u')^2 dx \right) - \frac{M}{\rho AL} \int_0^1 (\dot{u}' u'' + (\dot{u}')^2) dx \right] u'' = 0. \quad (1.31)$$

and after the insertion of the expression for $Q(t)$ one gets

$$\ddot{u} + \frac{EI}{\rho AL^4}u'''' + \frac{CEI}{\rho AL^4}\dot{u}'''' + \left[\frac{K}{\rho AL} \left(Q_0 + Q_1 \cos(\Omega t) - \frac{1}{2} \int_0^1 (u')^2 dx \right) - \frac{M}{\rho AL} \int_0^1 (\dot{u}' u'' + (\dot{u}')^2) dx \right] u'' = 0. \quad (1.32)$$

In this way we have shown what we desired to show. To make clear: (1.32) describes the vertical deflection, u , of the beam, for finitely small curvatures, $(u')^2 \ll 1$. In that way u does also represent finitely small deflections. (1.32) is a Duffing-type of equation with parametrically excitation. This type of equation is also called a Mathieu equation.

Since the beam is simply supported at A and B the deflection, U , and the bending moment, τ , at these points are identically equal to zero. And since the bending moment is proportional to U'' and \dot{U}'' for all C, E and I , $U''()$ and \dot{U}'' is also equal to zero at the endpoints of the beam. Furthermore we recall that $u(x, t) = \frac{U(X, t)}{L}$ and $x = \frac{X}{L}$. By that we clearly get

$$U(0, t) = 0 \Rightarrow u(0, t) = 0 \quad (1.33)$$

$$U''(0, t) = 0 \Rightarrow u''(0, t) = 0 \quad (1.34)$$

$$U(L, t) = 0 \Rightarrow u(1, t) = 0 \quad (1.35)$$

$$U''(L, t) = 0 \Rightarrow u''(1, t) = 0 \quad (1.36)$$

By that we have also validate the stated boundary conditions for (1.32).

For clarification it is now the goal to describe the physical interpretation of the terms in (1.32) and also identify which are linear and which are non-linear

- \ddot{u} . This term is connected to the inertia of the system and is linear.
- $\frac{EI}{\rho AL^4}u''''$. This term is a restoring force in the system and is linear.
- $\frac{K}{\rho AL} \left(Q_0 + Q_1 \cos(\Omega t) - \frac{1}{2} \int_0^1 (u')^2 dx \right) u''$. This term can also be interpreted as a restoring force. The first two terms are linear while the last term is non-linear.

- $\frac{CEI}{\rho AL^4} \dot{u}''''$. This term is connected to the damping of the system and is linear.
- $-\frac{M}{\rho AL} \left(\int_0^1 (\dot{u}' u'' + (\dot{u}')^2) dx \right) u''$. This term is connected to non-linear inertia in the system and is clearly non-linear. It arises through the non-linear relation between displacement of the right end of the beam and the inertia of the mass M .

1.3 c) Linear expression of the reaction forces at A and B

For completeness sake I state the linear expression of the reaction forces at point A and B and as a function of the transverse deflection $u(x, t)$. The way to find these expressions is to calculate the transverse force, T , in the beam and evaluate in A and B.

Now consider the linear part of (1.32) together with the equilibrium of force equation (1.13)

$$0 = \ddot{u} + \frac{EI}{\rho AL^4} u'''' + \frac{CEI}{\rho AL^4} \dot{u}'''' + \frac{K}{\rho AL} \left(Q_0 + Q_1 \cos(\Omega t) \right) u'' \Rightarrow \quad (1.37)$$

$$\ddot{u} = -\frac{EI}{\rho AL^4} u'''' - \frac{CEI}{\rho AL^4} \dot{u}'''' - \frac{K}{\rho AL} \left(Q_0 + Q_1 \cos(\Omega t) \right) u'' \Rightarrow \quad (1.38)$$

$$T' = \rho A \ddot{U} = \rho AL \ddot{u} = -\frac{EI}{L^3} u'''' - \frac{CEI}{L^3} \dot{u}'''' - K \left(Q_0 + Q_1 \cos(\Omega t) \right) u'' \Rightarrow \quad (1.39)$$

$$T = -\frac{EI}{L^3} u''' - \frac{CEI}{L^3} \dot{u}''' - K \left(Q_0 + Q_1 \cos(\Omega t) \right) u' \quad (1.40)$$

where (1.40) follows after integration of (1.39) from $x = 0$ to $x = x$. These boundary conditions implies that the constant of integration is equal to zero.

As earlier mentioned the linear expression of the reaction forces in A and B, as a function of u and its derivative, are then found by evaluating (1.40) in A and B

- Reaction force in A, $T = \left[-\frac{EI}{L^3} u''' - \frac{CEI}{L^3} \dot{u}''' - K \left(Q_0 + Q_1 \cos(\Omega t) \right) u' \right] \Big|_{x=0}$
- Reaction force in B, $T = \left[-\frac{EI}{L^3} u''' - \frac{CEI}{L^3} \dot{u}''' - K \left(Q_0 + Q_1 \cos(\Omega t) \right) u' \right] \Big|_{x=1}$

2 Eigenvalue problem, natural frequency and free modes

2.1 a) Eigenvalue problem (EVP)

The aim is now to derive an eigenvalue problem (EVP) based on (1.10), where the non-linear terms together with the damping term have been put equal to zero. Furthermore $Q_1 = 0$. The equation considered then takes the form

$$\ddot{u} + \frac{EI}{\rho AL^4} u'''' + \frac{KQ_0}{\rho AL} u'' = 0 \quad (2.1)$$

We assume that the solution can be expanded by the free modes, $\varphi_j(x)\sin(\omega_j t + \theta)$, so that the solution takes the form $u(x, t) = \sum_{j=0}^{\infty} \varphi_j(x)\sin(\omega_j t + \theta)$. By inserting $\varphi_j(x)\sin(\omega_j t + \theta)$ into (2.1) we arrive at

$$-\omega_j^2 \varphi_j \sin(\omega_j t + \omega) + \frac{EI}{\rho AL^4} \varphi_j'''' \sin(\omega_j t + \omega) + \frac{KQ_0}{\rho AL} \varphi_j'' \sin(\omega_j t + \omega) = 0 \quad (2.2)$$

Then we conclude that the EVP for the amplitude, φ_j , of the undamped linear system under static load is given by

$$\frac{EI}{\rho AL^4} \varphi_j'''' + \frac{KQ_0}{\rho AL} \varphi_j'' = \omega_j^2 \varphi_j \quad (2.3)$$

where ω_j^2 is the eigenvalue and the boundary conditions are given by

$$u(0, t) = 0 \Rightarrow \varphi_j(0) = 0 \quad (2.4)$$

$$u''(0, t) = 0 \Rightarrow \varphi_j''(0) = 0 \quad (2.5)$$

$$u(1, t) = 0 \Rightarrow \varphi_j(1) = 0 \quad (2.6)$$

$$u''(1, t) = 0 \Rightarrow \varphi_j''(1) = 0 \quad (2.7)$$

2.2 b) Investigation of the EVP

An investigation of the EVP is now being carrying out. The goal is to clarify if the EVP is self-adjoint and completely definite. Also it is the purpose to specify an interval for Q_0 for which the eigenvalues are real and positive (In that case free vibrations of the beam are namely possible).

The definition of self-adjointness and completely definiteness can be seen on page 41 and 42 in [1]. Two operators are here defined: K og L . By comparing (2.3) to the definitions it is seen that

$$K = \frac{EI}{\rho AL^4} \frac{d^4}{dx^4} + \frac{KQ_0}{\rho AL^4} \frac{d^2}{dx^2} \quad (2.8)$$

$$L = 1 \quad (2.9)$$

First it is examined if the EVP are self-adjoint. This is carried out by calculating the following integrals and conclude if they are true

$$\int_0^1 (uK\nu - \nu Ku)dx = 0 \quad \text{og} \quad \int_0^1 (uL\nu - \nu Lu)dx = 0 \quad (2.10)$$

where u and ν are test functions of (2.3).

calculation gives

$$\int_0^1 \left(u \frac{EI}{\rho AL^4} \frac{d^4\nu}{dx^4} + u \frac{KQ_0}{\rho AL^4} \frac{d^2\nu}{dx^2} - \nu \frac{EI}{\rho AL^4} \frac{d^4u}{dx^4} - \nu \frac{KQ_0}{\rho AL^4} \frac{d^2u}{dx^2} \right) dx \quad (2.11)$$

$$\underline{\int_0^1 (u1\nu - \nu 1u)dx = 0} \quad (2.12)$$

Using integration by parts two times on the fourth order terms and one time on the second order terms in (2.11) and utilize that the boundary conditions is homogeneous we get

$$\int_0^1 \left(u \frac{EI}{\rho AL^4} \frac{d^4\nu}{dx^4} + u \frac{KQ_0}{\rho AL^4} \frac{d^2\nu}{dx^2} - \nu \frac{EI}{\rho AL^4} \frac{d^4u}{dx^4} - \nu \frac{KQ_0}{\rho AL^4} \frac{d^2u}{dx^2} \right) dx = \quad (2.13)$$

$$\underline{\int_0^1 \left(u'' \frac{EI}{\rho AL^4} \nu'' - u' \frac{KQ_0}{\rho AL^4} \nu' - \nu'' \frac{EI}{\rho AL^4} u'' + \nu' \frac{KQ_0}{\rho AL^4} u' \right) dx = 0} \quad (2.14)$$

It can then be concluded that the EVP is self-adjoint.

To clarify: if the EVP is completely definite the following integrals has to be true.

$$\int_0^1 uKudx > 0 \quad \text{og} \quad \int_0^1 uLudx > 0 \quad (2.15)$$

$$\text{eller} \quad (2.16)$$

$$\int_0^1 uKudx < 0 \quad \text{og} \quad \int_0^1 uLudx < 0 \quad (2.17)$$

where again u is a test function of (2.3).

Since $L = 1$ it is easily seen that

$$\int_0^1 uLudx = \int_0^1 u1udx = \int_0^1 u^2 dx > 0. \quad (2.18)$$

We then conclude that only (2.15) can be fulfilled. Calculation using integration by parts with homogeneous boundary conditions gives

$$\int_0^1 u K u dx = \int_0^1 \left(u \frac{EI}{\rho AL^4} \frac{d^4 u}{dx^4} + u \frac{KQ_0}{\rho AL^4} \frac{d^2 u}{dx^2} \right) dx = \quad (2.19)$$

$$\frac{EI}{\rho AL^4} \int_0^1 \left(u \frac{d^4 u}{dx^4} \right) dx - \frac{KQ_0}{\rho AL^4} \int_0^1 \left(u \frac{d^2 u}{dx^2} \right) dx = \quad (2.20)$$

$$\frac{EI}{\rho AL^4} \int_0^1 \left(u'' u'' \right) dx - \frac{KQ_0}{\rho AL^4} \int_0^1 \left(u' u' \right) dx = \quad (2.21)$$

$$\frac{EI}{\rho AL^4} \int_0^1 (u'')^2 dx - \frac{KQ_0}{\rho AL^4} \int_0^1 (u')^2 dx. \quad (2.22)$$

Because Q_0 can take positive as well as negative values the EVP is not in general completely definite. By theorem 4.2 on page 44 in [1] it is seen that if the EVP is self-adjoint and completely definite then all the eigenvalues are real and positive. By considering (2.22) it is seen that the following restriction on Q_0 ensures that all the eigenvalues are real and positive

$$\frac{EI}{\rho AL^4} \int_0^1 (u'')^2 dx - \frac{KQ_0}{\rho AL^4} \int_0^1 (u')^2 dx > 0 \Rightarrow \quad (2.23)$$

$$\underline{\frac{EI}{K} \frac{\int_0^1 (u'')^2}{\int_0^1 (u')^2} > 0 > Q_0} \quad (2.24)$$

2.3 c) Rayleigh quotient $R[u_j]$

The goal now is to find an expression for the Rayleigh quotient, $R[u_j]$ for $j = 1, 2, \dots$ under application of the test functions $u_j = \sin(j\pi x)$.

The definition of the Rayleigh quotient is given on page 43 in [1] by

$$R[u_j] = \frac{\int_0^1 u_j K u_j dx}{\int_0^1 u_j L u_j dx} \quad (2.25)$$

where, as mentioned, u is a test function of (2.3). Calculation gives

$$R[u_j] = \frac{\int_0^1 u_j K u_j dx}{\int_0^1 u_j L u_j dx} \Rightarrow \quad (2.26)$$

$$\underline{R[u_j]} = \frac{\int_0^1 \sin(j\pi x) \left(\frac{EI}{\rho AL^4} \frac{d^4}{dx^4} \sin(j\pi x) + \frac{KQ_0}{\rho AL^4} \frac{d^2}{dx^2} \sin(j\pi x) \right) dx}{\int_0^1 \sin(j\pi x)^2 dx} = \quad (2.27)$$

$$\frac{\int_0^1 \sin(j\pi x) \left(\frac{EI}{\rho AL^4} \frac{d^4}{dx^4} \sin(j\pi x) + \frac{KQ_0}{\rho AL^4} \frac{d^2}{dx^2} \sin(j\pi x) \right) dx}{\int_0^1 \sin(j\pi x)^2 dx} = \quad (2.28)$$

$$\left(\frac{EI(j\pi)^4}{\rho AL^4} - \frac{KQ_0(j\pi)^2}{\rho AL^2} \right) \frac{\int_0^1 \sin(j\pi x) dx}{\int_0^1 \sin(j\pi x)^2 dx} = \frac{EI(j\pi)^4}{\rho AL^4} - \frac{KQ_0(j\pi)^2}{\rho AL^2}. \quad (2.29)$$

2.4 d) Eigenvalues and free modes

The objective is now to show that the Rayleigh quotients $R[u_j]$ for $j = 1, 2, \dots$ and test functions $u_j = \sin(j\pi x)$, respectively are eigenvalues and free mode shapes of the EVP so that

$$\omega_j^2 = \frac{EI}{\rho A} \left(\frac{j\pi}{L} \right)^4 - \frac{KQ_0 L}{\rho A} \left(\frac{j\pi}{L} \right)^2 \quad \text{for } j = 1, 2, \dots \quad (2.30)$$

$$\varphi_j(x) = \sin(j\pi x) \quad \text{for } 0 \leq x \leq 1 \quad (2.31)$$

are respectively squared natural frequencies and free mode shapes for the beam.

Since $\varphi_j(x) = \sin(j\pi x)$ earlier is used as test functions we know that $\varphi_j(x) = \sin(j\pi x)$ satisfies the boundary conditions of (2.3). By inserting $\varphi_j(x) = \sin(j\pi x)$ and (2.29) in (2.3) we get

$$\frac{EI}{\rho AL^4} (\sin(j\pi x))''' + \frac{KQ_0}{\rho AL} (\sin(j\pi x))'' = \left(\frac{EI}{\rho A} \left(\frac{j\pi}{L} \right)^4 - \frac{KQ_0}{\rho A} \left(\frac{j\pi}{L} \right)^2 \right) \sin(j\pi x) \quad (2.32)$$

$$\left(\frac{EI}{\rho A} \left(\frac{j\pi}{L} \right)^4 - \frac{KQ_0}{\rho A} \left(\frac{j\pi}{L} \right)^2 \right) \sin(j\pi x) = \left(\frac{EI}{\rho A} \left(\frac{j\pi}{L} \right)^4 - \frac{KQ_0}{\rho A} \left(\frac{j\pi}{L} \right)^2 \right) \sin(j\pi x) \quad (2.33)$$

$$0 = 0 \quad (2.34)$$

It can then be concluded that the orthogonal functions $\sin(j\pi x)$ satisfies (2.3) and also the boundary condition of this EVP. Further it is seen that the Rayleigh quotients given by (2.29) is the eigenvalues of (2.3) and thus denotes the squared natural frequencies. The objective is then reached.

It is further observed that $\omega_1^2 < 0$ implies the following

$$\frac{EI\pi^4}{\rho AL^4} - \frac{KQ_0L\pi^2}{\rho AL^2} < 0 \Rightarrow \quad (2.35)$$

$$\frac{EI\pi^2}{L^3} - KQ_0 < 0 \Rightarrow \quad (2.36)$$

$$\frac{EI\pi^2}{L^2} < KQ_0L \quad (2.37)$$

The expression to the right of the equality sign in (2.37) denotes the force by which the spring acts on the beam, and the expression to the left denotes the critical Euler load for the system of interest. Thus $\omega_1^2 < 0$ implies that the acting on the beam is larger than the critical load and the beam will therefore move away from the linear equilibrium $u = 0$.

3 Discretized model, free mode expansion

3.1 a) Free mode expansion

By applying that the solution, $u(x, t)$, to (1.10) with boundary conditions given by (1.11) can be expanded on the basis of the lowest n natural frequencies $\varphi_j(x)$, for $j = 1, 2, \dots, n$ (determined above) by

$$u(x, t) = \sum_{j=1}^n y_j(t) \varphi_j(x) = \sum_{j=1}^n y_j(t) \sin(j\pi x) \quad (3.1)$$

it is the objective to show that the modal amplitudes satisfies the equation

$$\ddot{y}_i + 2i^4 \beta \dot{y}_i + \left(\omega_i^2 + i^2 q \cos(\Omega t) + i\gamma \sum_{k=1}^n k^2 y_k^2 + 2i^2 \kappa \sum_{k=1}^n k^2 (y_k \ddot{y}_k + \dot{y}_k^2) \right) y_i = 0, \quad i = 1, 2, \dots, n \quad (3.2)$$

where ω_i denotes the linear natural frequency given by (2.30) and

$$\beta \equiv \frac{CEI\pi^2}{2\rho AL^4}, \quad q \equiv \frac{Q_1 K \pi^2}{\rho AL}, \quad \gamma \equiv \frac{K \pi^4}{4\rho AL}, \quad \kappa \equiv \frac{M \pi^4}{4\rho AL} \quad (3.3)$$

On the basis of the assumed form of the solution we get the following

$$\ddot{u} = \sum_{j=1}^n \ddot{y}_j(t) \sin(j\pi x) \quad (3.4)$$

$$u'' = -(j\pi)^2 \sum_{j=1}^n y_j(t) \sin(j\pi x) \quad (3.5)$$

$$\dot{u}''' = (j\pi)^4 \sum_{j=1}^n y_j(t) \sin(j\pi x) \quad (3.6)$$

$$u''' = (j\pi)^4 \sum_{j=1}^n y_j(t) \sin(j\pi x) \quad (3.7)$$

$$-\frac{1}{2} \int_0^1 (u')^2 dx = -\frac{1}{2} \int_0^1 \left[\left(\sum_{j=1}^n y_j(t) \sin(j\pi x) \right)' \right]^2 dx = -\frac{1}{2} \int_0^1 \left(\sum_{j=1}^n (j\pi) y_j(t) \cos(j\pi x) \right)^2 dx \quad (3.8)$$

$$-\int_0^1 u' \ddot{u}' dx = -\int_0^1 \sum_{j=1}^n (j\pi) y_j(t) \cos(j\pi x) \sum_{j=1}^n (j\pi) \ddot{y}_j(t) \cos(j\pi x) dx \quad (3.9)$$

$$-\int_0^1 (\dot{u}')^2 dx = -\int_0^1 \left(\sum_{j=1}^n (j\pi) y_j(t) \cos(j\pi x) \right)^2 dx \quad (3.10)$$

By inserting (3.4)-(3.10) in (1.10) we get

$$\begin{aligned}
& \sum_{j=1}^n \ddot{y}_j(t) \sin(j\pi x) + (j\pi)^4 \frac{CEI}{\rho AL^4} \sum_{j=1}^n y_j(t) \sin(j\pi x) + (j\pi)^4 \frac{EI}{\rho AL^4} \sum_{j=1}^n y_j(t) \sin(j\pi x) + \\
& \left[\frac{K}{\rho AL} \left(Q_0 + Q_1 \cos(\Omega t) - \frac{1}{2} \int_0^1 \left(\sum_{j=1}^n (j\pi) y_j(t) \cos(j\pi x) \right)^2 dx \right) \right. \\
& + \frac{M}{\rho AL} \left(- \int_0^1 \sum_{j=1}^n (j\pi) y_j(t) \cos(j\pi x) \sum_{j=1}^n (j\pi) \ddot{y}_j(t) \cos(j\pi x) dx - \int_0^1 \left(\sum_{j=1}^n (j\pi) \dot{y}_j(t) \cos(j\pi x) \right)^2 dx \right) \\
& \cdot \left. \left(-(j\pi)^2 \sum_{j=1}^n y_j(t) \sin(j\pi x) \right) \right] = 0 \quad (3.11)
\end{aligned}$$

By multiplying (3.11) by the free mode shape $\varphi_i(x) = \sin(i\pi x)$, integrating over the length, applying that

$$\int_0^1 \sin(i\pi x) \sin(j\pi x) dx \begin{cases} 0 & i \neq j \\ \frac{1}{2} & i = j \end{cases}, \quad (3.12)$$

which follows from the fact that $\sin(i\pi x)$ and $\sin(j\pi x)$ are orthogonal functions, and finally interchange summation and integration we arrive at

$$\begin{aligned}
& \int_0^1 \sin(i\pi x) \sum_{j=1}^n \ddot{y}_j(t) \sin(j\pi x) + \int_0^1 \sin(i\pi x) (j\pi)^4 \frac{CEI}{\rho AL^4} \sum_{j=1}^n y_j(t) \sin(j\pi x) + \\
& \int_0^1 \sin(i\pi x) (j\pi)^4 \frac{EI}{\rho AL^4} \sum_{j=1}^n y_j(t) \sin(j\pi x) + \\
& \left[\frac{K}{\rho AL} \left(Q_0 + Q_1 \cos(\Omega t) - \frac{1}{2} \int_0^1 \left(\sum_{j=1}^n (j\pi) y_j(t) \cos(j\pi x) \right)^2 dx \right) \right. \\
& + \frac{M}{\rho AL} \left(- \int_0^1 \sum_{j=1}^n (j\pi) y_j(t) \cos(j\pi x) \sum_{j=1}^n (j\pi) \ddot{y}_j(t) \cos(j\pi x) dx - \int_0^1 \left(\sum_{j=1}^n (j\pi) \dot{y}_j(t) \cos(j\pi x) \right)^2 dx \right) \\
& \cdot \left. \int_0^1 \sin(i\pi x) \left(-(j\pi)^2 \sum_{j=1}^n y_j(t) \sin(j\pi x) \right) \right] = 0 \Rightarrow \quad (3.13)
\end{aligned}$$

$$\begin{aligned}
& \frac{1}{2}\ddot{y}_i(t) + (i\pi)^4 \frac{CEI}{2\rho AL^4} \dot{y}_i(t) + (i\pi)^4 \frac{EI}{2\rho AL^4} y_i(t) + \\
& \left[\frac{K}{\rho AL} \left(Q_0 + Q_1 \cos(\Omega t) - \frac{1}{2} \int_0^1 \left(\sum_{k=1}^n (k\pi) y_k(t) \cos(k\pi x) \right)^2 dx \right) \right. \\
& + \frac{M}{\rho AL} \left(- \int_0^1 \sum_{k=1}^n (k\pi) y_k(t) \cos(k\pi x) \sum_{k=1}^n (k\pi) \ddot{y}_k(t) \cos(k\pi x) dx - \int_0^1 \left(\sum_{k=1}^n (k\pi) \dot{y}_k(t) \cos(k\pi x) \right)^2 dx \right) \\
& \left. \cdot \left(- \frac{(i\pi)^2}{2} y_i(t) \right) = 0 \Rightarrow \quad (3.14) \right]
\end{aligned}$$

$$\begin{aligned}
& \ddot{y}_i(t) + 2i^4 \beta \dot{y}_i(t) + \left[\omega_i^2 + i^2 q \cos(\Omega t) + 2i^2 \gamma \int_0^1 \left(\sum_{k=1}^n k y_k(t) \cos(k\pi x) \right)^2 dx \right. \\
& + 4i^2 \kappa \int_0^1 \sum_{k=1}^n k y_k(t) \cos(k\pi x) \sum_{k=1}^n k \dot{y}_k(t) \cos(k\pi x) dx + 4i^2 \kappa \int_0^1 \left(\sum_{k=1}^n k \dot{y}_k(t) \cos(k\pi x) \right)^2 dx \\
& \left. \cdot y_i(t) = 0 \Rightarrow \quad (3.15) \right]
\end{aligned}$$

$$\begin{aligned}
& \ddot{y}_i(t) + 2i^4 \beta \dot{y}_i(t) + \left[\omega_i^2 + i^2 q \cos(\Omega t) + 2i^4 \gamma \sum_{k=1}^n k^2 y_k^2(t) \int_0^1 \cos^2(k\pi x) dx \right. \\
& + 4i^2 \kappa \sum_{k=1}^n k^2 y_k(t) \ddot{y}_k(t) \int_0^1 \cos^2(k\pi x) dx + 4i^2 \kappa \sum_{k=1}^n k^2 y_k^2(t) \int_0^1 \cos^2(k\pi x) dx \left. \right] y_i(t) = 0 \Rightarrow \\
& \quad (3.16)
\end{aligned}$$

$$\ddot{y}_i(t) + 2i^4 \beta \dot{y}_i(t) + \left[\omega_i^2 + i^2 q \cos(\Omega t) + i^2 \gamma \sum_{k=1}^n k^2 y_k^2(t) + 2i^2 \kappa \sum_{k=1}^n k^2 \left(y_k(t) \ddot{y}_k(t) + y_k^2(t) \right) \right] y_i(t) = 0, \quad i = 1, 2, \dots, n$$

The stated constants β , q , γ , κ are defined by (3.3) and ω_i denotes the linear natural frequency defined by (2.30). The objective is then reached.

3.2 b) Primary resonance

The objective is now to identify which frequency, Ω , in (3.2) be a course for primary resonance. It is assumed that $\omega_i > 0$. Also it is the goal to clarify if internal resonance would be able to occur.

Since (3.2) is a Duffing-type of equation with parametric excitation it is given on page 96-98 in [1], that primary resonance occurs for $\Omega = 2\omega_i$, $i = 1, 2, \dots, n$.

Also, on page 137 in [1] it can be seen that the criteria for internal resonance in the system (which is non-linear of order three) is given as

$$\omega_i \approx 3\omega_j, \quad \omega_i \approx 2\omega_j \pm \omega_k, \quad \omega_i \approx \omega_j \pm \omega_k \pm \omega_l, \quad (3.18)$$

The first criterion is simple to confirm while the other criterions are more technical. Letting $\omega_i = 3\omega_j$ in (2.30) we get the following condition

$$\frac{EI\pi^2}{KQ_0L^3} = \frac{j^2 - 9i^2}{j^4 - 9i^4} \quad (3.19)$$

Since $j, i \in \mathcal{N}$ (3.19) leads to $j > 3i$.

Then, what can be concluded is the following: If for instance $i = 1$ og $j = 4$ and at the same time the parameters in the system are fixed to satisfy (3.19) for $i = 1$ og $j = 4$ then internal resonance is observed in the system.

In this case we have

$$\frac{EI\pi^2}{KQ_0L^3} = \frac{j^2 - 9i^2}{j^4 - 9i^4} = \frac{7}{247} \quad (3.20)$$

3.3 c) Approximation to the dynamical response of the beam

With $n = 1$ (3.2) takes the form

$$\ddot{y} + 2\beta\dot{y} + (\omega^2 + q\cos(\Omega t))y + \gamma y^3 + 2\kappa(y\ddot{y} + \dot{y}^2)y = 0 \quad (3.21)$$

where $w \equiv w_1$ og $y \equiv y_1$.

First it will be stated under which conditions this approximation describes the response of the beam satisfactory.

Since (3.21) is a simple-form approximation the restriction is that Ω is fare from the second and higher order natural frequencies. If this is not the case, the solution should include at least two of the equations on the form (3.17), one for each natural frequency that the response should reflect. The reason is that the deflection of the beam is described as a summation of the mode shapes associated with the natural frequencies.

For completeness the terms in (3.21) are categorized:

- \ddot{y} og $2\kappa(y\ddot{y} + \dot{y}^2)y$ are connected to the inertia in the system. The last two terms are due to non-linear inertia which is a result of the non-linear connection between the compression, Z , and the deflection, u of the beam.
- $2\beta\dot{y}$ is connected to the damping in the system.
- $(\omega^2 + q\cos(\Omega t))y$ and γy^3 are connected to the restoring force in the system.

4 Local analysis of the system under static load

4.1 a) First order system, stationary points, there stability classification and the flow in the phase plane

Utilizing the simple-form approximation (3.21) with $q = 0$ the objective is now to set up an identically first order system of differential equations where $v = \dot{y}$. Further a determination of the stationary points, there stability and classification is wanted for $\beta > 0$, $\gamma > 0$, $\kappa > 0$, $\omega^2 \in R$ and $\beta^2 \ll |\omega^2|$. Finally it is the goal to work out illustrations of the flow in the phase plane.

Since $v = \dot{y}$ it follows that $\dot{v} = \ddot{y}$. And since further $q = 0$ (3.21) gives

$$\ddot{y} + 2\beta\dot{y} + \omega^2y + \gamma y^3 + 2\kappa(y\ddot{y} + \dot{y}^2)y = 0 \Rightarrow \quad (4.1)$$

$$\ddot{y}(1 + 2\kappa y^2) + 2\beta\dot{y} + 2\kappa\dot{y}^2y + \omega^2y + \gamma y^3 = 0 \Rightarrow \quad (4.2)$$

$$\dot{y} = -\frac{2\beta\dot{y} + 2\kappa\dot{y}^2y + \omega^2y + \gamma y^3}{(1 + 2\kappa y^2)} \quad (4.3)$$

By that we have

$$\dot{y} = v \quad (4.4)$$

$$\dot{v} = \ddot{y} = -\frac{2\beta v + 2\kappa v^2y + \omega^2y + \gamma y^3}{(1 + 2\kappa y^2)} \quad (4.5)$$

(4.4) og (4.5) defines the identical first order system to (3.21).

To identify the stationary point it is seen that

$$\dot{y} = 0 \Rightarrow \underline{\underline{v = 0}} \quad (4.6)$$

$$\dot{v} = 0 \Rightarrow -\frac{2\beta v + 2\kappa v^2y + \omega^2y + \gamma y^3}{(1 + 2\kappa y^2)} = 0 \Rightarrow \quad (4.7)$$

$$\underline{\underline{\omega^2y + \gamma y^3 = 0}} \Rightarrow y = 0 \vee y = \pm\sqrt{\frac{-\omega^2}{\gamma}} \quad (4.8)$$

Thus it follows that three stationary points exist.

$$(y^*, v^*) = (0, 0) \quad \wedge \quad (y^*, v^*) = \left(\sqrt{\frac{-\omega^2}{\gamma}}, 0\right) \quad \wedge \quad (y^*, v^*) = \left(-\sqrt{\frac{-\omega^2}{\gamma}}, 0\right) \quad (4.9)$$

Note that the two last stationary points in (4.9) only exist for $\omega^2 \leq 0$ and only takes different values for $\omega^2 < 0$

To determine the stability of the stationary points given by (4.9) the jacobian $\mathcal{J}(y, v)$ of

the system (4.4) and (4.5) is calculated and evaluated in the stationary points. Then the following equation is solved: $\mathfrak{D}\text{et}(\mathcal{J}(y^*, v^*) - \lambda\mathcal{I}) = 0$ for λ , where $\lambda_j, j = 1, 2$. is the eigenvalues of $\mathcal{J}(y_j^*, v_j^*), j = 1, 2$, \mathcal{I} is the identity matrix with same dimension as $\mathcal{J}(y^*, v^*)$ and $\mathfrak{D}\text{et}$ denotes the determinant. Utilizing that $v^* = 0$ for all the stationary points calculation gives

$$\mathcal{J} = \begin{bmatrix} \frac{\partial \dot{y}}{\partial y} & \frac{\partial \dot{y}}{\partial v} \\ \frac{\partial \dot{v}}{\partial y} & \frac{\partial \dot{v}}{\partial v} \end{bmatrix} \quad (4.10)$$

$$\frac{\partial \dot{y}}{\partial y} = 0 \quad (4.11)$$

$$\frac{\partial \dot{y}}{\partial v} = 1 \quad (4.12)$$

$$\left. \frac{\partial \dot{v}}{\partial y} \right|_{v^*=0} = \frac{-2\gamma\kappa y^4 - 3\gamma y^2 + 2\kappa\omega^2 y^2 - \omega^2}{(1+2\kappa y^2)^2} \quad (4.13)$$

$$\left. \frac{\partial \dot{v}}{\partial v} \right|_{v^*=0} = -\frac{2\beta}{(1+2\kappa y^2)} \quad (4.14)$$

(4.15)

$$\mathcal{J} = \begin{bmatrix} 0 & 1 \\ \frac{-2\gamma\kappa y^4 - 3\gamma y^2 + 2\kappa\omega^2 y^2 - \omega^2}{(1+2\kappa y^2)^2} & -\frac{2\beta}{(1+2\kappa y^2)} \end{bmatrix} \quad (4.16)$$

An investigation of each of the stationary points given by (4.9) is now being carried through. First we consider $(y^*, v^*) = (0, 0)$

4.1.1 $(y^*, v^*) = (0, 0)$

$$\mathcal{J} = \begin{bmatrix} 0 & 1 \\ -\omega^2 & -2\beta \end{bmatrix} \Rightarrow \quad (4.17)$$

$$\mathfrak{D}\text{et}(\mathcal{J} - \lambda\mathcal{I}) = 0 \Rightarrow \lambda^2 + 2\beta\lambda + \omega^2 = 0 \Rightarrow \quad (4.18)$$

$$\underline{\lambda} = -\beta \pm \sqrt{\beta^2 - \omega^2} = \underline{-\beta \pm i\sqrt{\omega^2}} \quad (4.19)$$

since $\beta^2 \ll |\omega^2|$ and where $i = \sqrt{-1}$.

Two disjoint cases are now considered $\omega^2 > 0$ og $\omega^2 < 0$

- $\omega^2 > 0$

In this case λ takes two complex conjugated values, $\lambda_1 = -\beta - i\sqrt{\omega^2}$ and $\lambda_2 = -\beta + i\sqrt{\omega^2}$.

Since the real part $\Re e$ of λ_1 and λ_2 is equal to $-\beta < 0$, we conclude that the stationary point $(y^*, v^*) = (0, 0)$ is a stable foci

- $\omega^2 < 0$

In this case λ represent two real numbers $\lambda_1 = -\beta - \sqrt{-\omega^2}$ and $\lambda_2 = -\beta + \sqrt{-\omega^2}$.

Note that $\lambda_1\lambda_2 = \beta^2 + \omega^2 = \omega^2 < 0$ (where the last equality follows from the assumption $\beta^2 \ll |\omega^2|$).

Thus we conclude that the stationary point $(y^*, v^*) = (0, 0)$ is an unstable saddle point

We then consider $(y^*, v^*) = \left(\sqrt{\frac{-\omega^2}{\gamma}}, 0\right) \wedge (y^*, v^*) = \left(-\sqrt{\frac{-\omega^2}{\gamma}}, 0\right)$ together in one case since the jacobian evaluated at these two stationary points are the same.

$$4.1.2 \quad (y^*, v^*) = \left(\sqrt{\frac{-\omega^2}{\gamma}}, 0\right) \wedge (y^*, v^*) = \left(-\sqrt{\frac{-\omega^2}{\gamma}}, 0\right)$$

$$\mathcal{J} = \begin{bmatrix} 0 & 1 \\ \frac{-2\gamma\omega^2}{(2\kappa\omega^2-\gamma)} & \frac{2\beta\gamma}{(2\kappa\omega^2-\gamma)} \end{bmatrix} \Rightarrow \quad (4.20)$$

$$\text{Det}(\mathcal{J} - \lambda\mathcal{I}) = 0 \Rightarrow \lambda^2 - \frac{2\beta\gamma}{(2\kappa\omega^2-\gamma)}\lambda + \frac{2\gamma\omega^2}{(2\kappa\omega^2-\gamma)} = 0 \Rightarrow \quad (4.21)$$

$$\lambda = \frac{\beta\gamma}{(2\kappa\omega^2-\gamma)} \pm i\sqrt{\frac{-(\beta^2 + 2\omega^2)\gamma^2 + 4\gamma\kappa\omega^4}{(2\kappa\omega^2-\gamma)^2}} \Rightarrow \quad (4.22)$$

$$\underline{\lambda} = \frac{\beta\gamma}{(2\kappa\omega^2-\gamma)} \pm i\sqrt{\frac{-2\omega^2\gamma^2 + 4\gamma\kappa\omega^4}{(2\kappa\omega^2-\gamma)^2}} \quad (4.23)$$

since $\beta^2 \ll |\omega^2|$ and where $i = \sqrt{-1}$.

A earlier mentioned the stationary points

$(y^*, v^*) = \left(\sqrt{\frac{-\omega^2}{\gamma}}, 0\right) \wedge (y^*, v^*) = \left(-\sqrt{\frac{-\omega^2}{\gamma}}, 0\right)$ do only exist for $\omega^2 \leq 0$ and takes different values for $\omega^2 < 0$. From (4.23) we then conclude that $\frac{-2\omega^2\gamma^2 + 4\gamma\kappa\omega^4}{(2\kappa\omega^2-\gamma)^2} > 0$ and that $\frac{\beta\gamma}{(2\kappa\omega^2-\gamma)} < 0$ which shows that λ represents two complex conjugated numbers. Thus the two stationary points $(y^*, v^*) = \left(\sqrt{\frac{-\omega^2}{\gamma}}, 0\right) \wedge (y^*, v^*) = \left(-\sqrt{\frac{-\omega^2}{\gamma}}, 0\right)$ can then be categorized as stable Foci for $\omega^2 < 0$.

Below is seen some illustrations of the phase plane for different parameter configurations. First is shown illustrations for $\omega^2 > 0$ and then for $\omega^2 < 0$. The illustrations are carried out both with and without damping (without damping: $\beta = 0$). Also note, that the red circle on the illustrations are the initial conditions, while the green circle is where the trace ends.

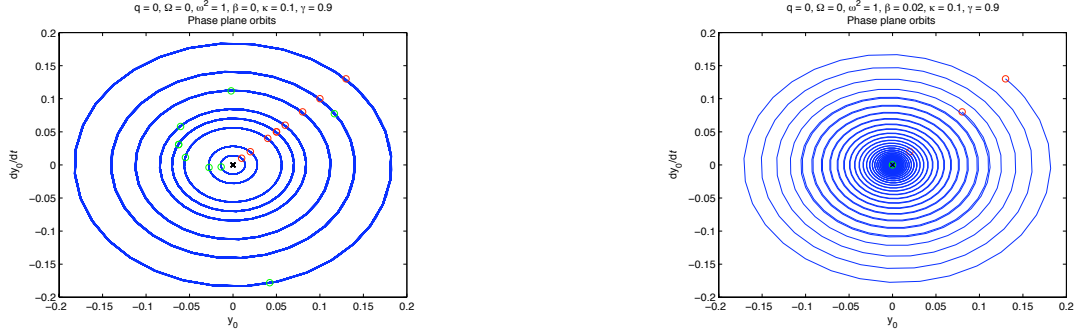


Figure 3: Phase plane illustrations

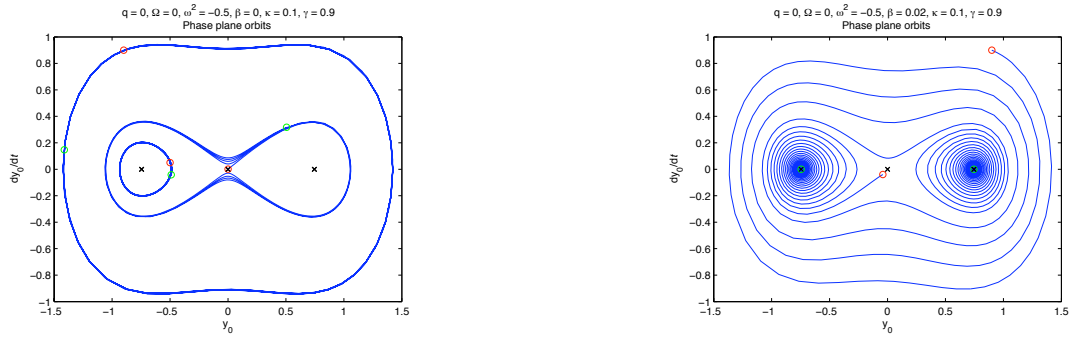


Figure 4: Phase plane illustrations

4.2 b) Bifurcation in then parameter space

The objective is now to show that $(y, v, \omega^2) = (0, 0, 0)$ is a bifurcation point. Furthermore the goal is to create a bifurcation diagram in the (ω^2, y) -plane.

By considering (4.19) we get for $\omega^2 = 0$: $\lambda = -\beta \pm i\sqrt{-\beta^2} \Rightarrow \lambda_1 = -2\beta \wedge \lambda_2 = 0$.

If further (4.22) is considered we get $\lambda = -\beta \pm i\sqrt{-\beta^2} \Rightarrow \lambda_1 = -2\beta \wedge \lambda_2 = 0$. Also recall that $\beta > 0$. These calculations shows that the eigenvalues for the three stationary points are respectively identically and that $\lambda_2 = 0$. This gives that $\omega^2 = 0$ is a bifurcation value. The fact that the eigenvalues are respectively identically are no surprise since the stationary points given by (4.9) are identically for $\omega^2 = 0$. Since it then can be concluded that the system has one stable stationary point for $\omega^2 > 0$ and two stable together with one unstable stationary point for $\omega^2 < 0$ and further that $(y^*, v^*) = (0, 0)$ is a stationary point at the bifurcation value $\omega^2 = 0$, then the set $(y, v, \omega^2) = (0, 0, 0)$ in the parameter space will be a bifurcation set.

In the (ω^2, y) -plane the bifurcation diagram takes the appearance

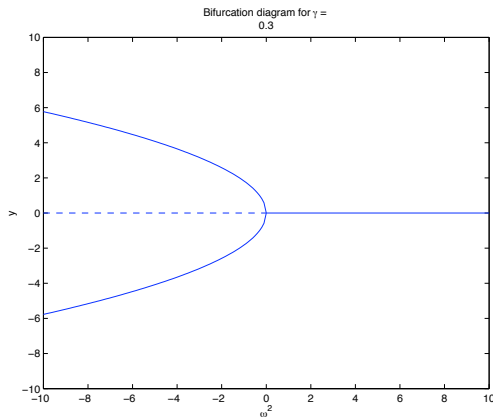


Figure 5: Bifurcation diagram for the beam

(solid/dashed line indicates stable/unstable branch). Based on the bifurcation diagram we conclude that the bifurcation that takes place at $(y, v, \omega^2) = (0, 0, 0)$ is a supercritical pitchfork bifurcation.

For $\omega^2 > 0$ a perturbation will make the beam oscillate around the stable equilibrium configuration $u = 0$. If the system is modeled with damping, the oscillation will die out as times go, and the system will turn up in the equilibrium configuration $u = 0$.

For $\omega^2 < 0$ a perturbation of the system will make the beam starting oscillating around one of the two stable equilibrium configurations $u(x, t) = \pm \sqrt{-\omega^2/\gamma} \sin(\pi x)$ (which are calculated from (3.17)). If damping is included in the model of the system the beam will end up in one of the equilibrium configurations $u(x, t) = \pm \sqrt{-\omega^2/\gamma} \sin(\pi x)$. Which one of them depends on the initial conditions. Thus a qualitative change in the dynamics of the beam happens at the bifurcation point. (Of cause, since this is the definition of a bifurcation).

5 Quantitative analysis of the system under dynamical load

The objective now is to carry out an quantitative analysis of the system under dynamical load. The analysis is based upon the assumption that the solution to (3.21) can be written as a multi scale solution (described in more details below). The analysis is divided into two disjoint cases $\omega^2 > 0$ and $\omega^2 < 0$ because of the qualitative change in the system at $\omega^2 = 0$.

5.1 a) $\omega^2 > 0$

First, the case $\omega^2 > 0$ is considered near primary resonance. This case corresponds to a situation where the initial tension KQ_0L in the spring implies that the beam is stretched for $u(x, t) = 0$ or that the compressive load is lesser in magnitude than the critical Euler load, $P_k = \frac{EI\pi^2}{L^2}$.

Now, the assumption is that the solution can be expressed as

$$y(T_0, T_1) = y_0(T_0, T_1) + \epsilon y_1(T_0, T_1) + \mathcal{O}(\epsilon^2), \quad \epsilon \ll 1, \quad (T_0, T_1) = (t, \epsilon t) \quad (5.1)$$

and that the dynamical load, the damping and all the non-linear terms are weak, which implies that these terms are of order $\mathcal{O}(\epsilon)$. Then (3.21) takes the form

$$\ddot{y} + \omega^2 y = -\epsilon \left(2\beta \dot{y} + q \cos(\Omega t) y + \gamma y^3 + 2\kappa(y\ddot{y} + \dot{y}^2)y \right) \quad (5.2)$$

Note that the introduced time scales $(T_0, T_1) = (t, \epsilon t)$ respectively represent the true time and a scaling of the true time.

Also, based upon the chain rule the following differential operators are introduced

$$\frac{\partial}{\partial t} = D_0 + \epsilon D_1 \quad (5.3)$$

$$\frac{\partial^2}{\partial t^2} = D_0^2 + 2\epsilon D_0 D_1 + \mathcal{O}(\epsilon^2) \quad (5.4)$$

where

$$D_i^j \equiv \frac{\partial^j}{\partial T_i^j}. \quad (5.5)$$

We then get

$$\dot{y} = (D_0 + \epsilon D_1)y \quad (5.6)$$

$$\ddot{y} = (D_0^2 + 2\epsilon D_0 D_1 + \mathcal{O}(\epsilon^2))y. \quad (5.7)$$

For simplicity an analysis of each term in (5.2) is being carried out one term at the time.

- $\ddot{y} = (D_0^2 + 2\epsilon D_0 D_1 + \mathcal{O}(\epsilon^2))(y_0 + \epsilon y_1) = D_0^2 y_0 + D_0^2 y_1 + \epsilon 2D_0 D_1 y_0 + \mathcal{O}(\epsilon^2)$
- $\omega^2 y = \omega^2(y_0 + \epsilon y_1) = \omega^2 y_0 + \epsilon \omega^2 y_1$
- $-\epsilon 2\beta \dot{y} = -\epsilon 2\beta(D_0 + \epsilon D_1)(y_0 + \epsilon y_1) = -\epsilon 2\beta D_0 y_0 + \mathcal{O}(\epsilon^2)$
- $-\epsilon \gamma y^3 = -\epsilon \gamma(y_0 + \epsilon y_1)^3 = -\epsilon \gamma y_0^3 + \mathcal{O}(\epsilon^2)$
- $-\epsilon 2\kappa y^2 \ddot{y} = -\epsilon 2\kappa(y_0 + \epsilon y_1)^2(D_0^2 + 2\epsilon D_0 D_1 + \mathcal{O}(\epsilon^2))(y_0 + \epsilon y_1) = -\epsilon 2\kappa y_0^2 D_0^2 y_0 + \mathcal{O}(\epsilon^2)$
- $-\epsilon 2\kappa y \dot{y}^2 = -\epsilon 2\kappa(y_0 + \epsilon y_1) \left((D_0 + \epsilon D_1)(y_0 + \epsilon y_1) \right)^2 = -\epsilon 2\kappa y_0 (D_0 y_0)^2 + \mathcal{O}(\epsilon^2)$
- $-\epsilon q \cos(\Omega t) y = -\frac{1}{2} \epsilon q e^{i\Omega t} (y_0 + \epsilon y_1) = -\frac{1}{2} \epsilon q e^{i\Omega t} y_0 + \mathcal{O}(\epsilon^2)$

By inserting the terms found above in (5.2) we achieve that (5.2) can be written as

$$C_1 + C_2 \epsilon + \mathcal{O}(\epsilon^2) = C_3 + C_4 \epsilon + \mathcal{O}(\epsilon^2) \quad (5.8)$$

where

$$C_1 = D_0^2 y_0 + \omega^2 y_0 \quad (5.9)$$

$$C_2 = D_0^2 y_1 + 2D_0 D_1 y_0 + \omega^2 y_1 \quad (5.10)$$

$$C_3 = 0 \quad (5.11)$$

$$C_4 = -2\beta D_0 y_0 - \gamma y_0^3 - 2\kappa y_0^2 D_0^2 y_0 - 2\kappa y_0 (D_0 y_0)^2 - \frac{1}{2} q y_0 e^{i\Omega T_0} \quad (5.12)$$

Since (5.8) has to be valid for all $\epsilon \ll 1$ we arrive at the following equations

$$D_0^2 y_0 + \omega^2 y_0 = 0 \quad (5.13)$$

$$D_0^2 y_1 + \omega^2 y_1 = -2D_0 D_1 y_0 - 2\beta D_0 y_0 - \gamma y_0^3 - 2\kappa y_0^2 D_0^2 y_0 - 2\kappa y_0 (D_0 y_0)^2 - \frac{1}{2} q y_0 e^{i\Omega T_0} \quad (5.14)$$

The solution to (5.13) is given by

$$y_0 = A(T_1) e^{i\omega T_0} + \bar{A}(T_1) e^{-i\omega T_0} \quad (5.15)$$

where $i = \sqrt{-1}$ and $\bar{A}(T_1)$ is the complex conjugated of $A(T_1)$

By inserting (5.15) in the right hand side of (5.14) and write up the individual terms we get

- $-2D_0 D_1 y_0 = -2i\omega A'(T_1) e^{i\omega T_0} + cc$
- $-2\beta D_0 y_0 = -2i\omega \beta A(T_1) e^{i\omega T_0} + cc$
- $-\gamma y_0^3 = -\gamma (A(T_1)^3 e^{3i\omega T_0} + 3A(T_1)^2 \bar{A}(T_1) e^{i\omega T_0}) + cc$
- $-2\kappa y_0^2 D_0^2 y_0 = -2\kappa i^2 \omega^2 (A(T_1)^3 e^{3i\omega T_0} + A(T_1)^2 \bar{A}(T_1) e^{i\omega T_0}) + cc$
- $-2\kappa y_0 (D_0 y_0)^2 = -2\kappa i^2 \omega^2 (A(T_1)^3 e^{3i\omega T_0} + A(T_1)^2 \bar{A}(T_1) e^{i\omega T_0}) + cc$
- $-\frac{1}{2} q y_0 e^{i\Omega T_0} = -\frac{1}{2} q (A(T_1) e^{i(\Omega+\omega)T_0} + \bar{A}(T_1) e^{i(\Omega-\omega)T_0}) + cc$

where cc denotes the complex conjugated of the previous terms.

By inserting the terms found above in (5.14) we arrive at

$$\begin{aligned} D_0^2 y_1 + \omega^2 y_1 = & \left[-2i\omega A'(T_1) - 2i\omega \beta A(T_1) - 3\gamma A(T_1)^2 \bar{A}(T_1) + 4\kappa \omega^2 A(T_1)^2 \bar{A}(T_1) \right] e^{i\omega T_0} + \\ & \left[-\gamma A(T_1)^3 + 4\kappa \omega^2 A(T_1)^3 \right] e^{3i\omega T_0} - \frac{1}{2} q \left(A(T_1) e^{i(\Omega+\omega)T_0} + \bar{A}(T_1) e^{i(\Omega-\omega)T_0} \right) + cc \quad (5.16) \end{aligned}$$

Since the case near primary resonance, $\Omega = 2\omega$, is considered, a parameter σ defined by

$$\Omega = 2\omega + \epsilon\sigma \quad (5.17)$$

is introduced to measure the nearness to $\Omega = 2\omega$.

(5.17) is now put into (5.16) yielding

$$\begin{aligned} D_0^2 y_1 + \omega^2 y_1 = & \left[-2i\omega A'(T_1) - 2i\omega \beta A(T_1) - 3\gamma A(T_1)^2 \bar{A}(T_1) + 4\kappa \omega^2 A(T_1)^2 \bar{A}(T_1) \right] e^{i\omega T_0} + \\ & \left[-\gamma A(T_1)^3 + 4\kappa \omega^2 A(T_1)^3 \right] e^{3i\omega T_0} - \frac{1}{2} q \left(A(T_1) e^{3i\omega T_0} e^{i\sigma T_1} + \bar{A}(T_1) e^{i\omega T_0} e^{i\sigma T_1} \right) + cc \Rightarrow \\ D_0^2 y_1 + \omega^2 y_1 = & \left[-2i\omega A'(T_1) - 2i\omega \beta A(T_1) - 3\gamma A(T_1)^2 \bar{A}(T_1) + 4\kappa \omega^2 A(T_1)^2 \bar{A}(T_1) - \frac{1}{2} q \bar{A}(T_1) e^{i\sigma T_1} \right] e^{i\omega T_0} + \\ & \left[-\gamma A(T_1)^3 + 4\kappa \omega^2 A(T_1)^3 - \frac{1}{2} q A(T_1) e^{i\sigma T_1} \right] e^{3i\omega T_0} + cc \quad (5.18) \end{aligned}$$

Terms proportional to $e^{i\omega T_0}$ causes secular terms and therefore have to be eliminated. By inspecting (5.18) the following equation has to be satisfied if a physical realistic solution of (5.18) is wanted.

$$-2i\omega A'(T_1) - 2i\omega \beta A(T_1) - 3\gamma A(T_1)^2 \bar{A}(T_1) + 4\kappa \omega^2 A(T_1)^2 \bar{A}(T_1) - \frac{1}{2} q \bar{A}(T_1) e^{i\sigma T_1} = 0 \quad (5.19)$$

(5.18) then takes the form

$$D_0^2 y_1 + \omega^2 y_1 = \left[-\gamma A(T_1)^3 + 4\kappa\omega^2 A(T_1)^3 - \frac{1}{2}qA(T_1)e^{i\sigma T_1} \right] e^{3i\omega T_0} + cc \quad (5.20)$$

A particular solution is then given by

$$y_1 = \frac{\frac{1}{2}A(T_1)qe^{i\sigma T_1} + A^3(T_1)(\gamma - 4\omega^2\kappa)}{8\omega^2} e^{3i\omega T_0} + cc \quad (5.21)$$

All together we then get

$$\begin{aligned} y(T_0, T_1) &= y_0(T_0, T_1) + \epsilon y_1(T_0, T_1) + \mathcal{O}(\epsilon^2) = \\ &A(T_1)e^{i\omega T_0} + \epsilon \frac{\frac{1}{2}A(T_1)qe^{i\sigma T_1} + A^3(T_1)(\gamma - 4\omega^2\kappa)}{8\omega^2} e^{3i\omega T_0} + \mathcal{O}(\epsilon^2) + cc \end{aligned} \quad (5.22)$$

To determine the amplitude $A(T_1)$ which is modeled by (5.19) we set $A(T_1) = \frac{1}{2}ae^{i\varphi}$, $a(T_1), \varphi(T_1) \in \mathcal{R}$. By insertion in (5.19) and separation of the real and imaginary part we get the following two equations of a and $\Psi = \sigma T_1 - 2\varphi \Rightarrow \Psi' = \sigma - 2\varphi'$

$$\begin{aligned} a' &= -\beta a - \frac{1}{4}\frac{q}{\omega}a\sin(\sigma T_1 - 2\varphi) = -\beta a - \frac{1}{4}\frac{q}{\omega}a\sin(\Psi) \\ a\Psi' &= -\frac{3}{4}\frac{\gamma}{\omega}a^3 + \kappa\omega a^3 + \sigma a - \frac{1}{2}\frac{q}{\omega}a\cos(\sigma T_1 - 2\varphi) = -\frac{3}{4}\frac{\gamma}{\omega}a^3 + \kappa\omega a^3 + \sigma a - \frac{1}{2}\frac{q}{\omega}a\cos(\Psi) \end{aligned} \quad (5.23)$$

The stationary solutions of (5.23) and (5.24) is given by letting $\Psi' = 0$ and $a' = 0$. The frequency-response equation $a(\Omega)$ is then given by

$$a = \pm \sqrt{\frac{1}{\kappa\omega - \frac{3}{4}\frac{\gamma}{\omega}} \left(-\sigma \pm \sqrt{\frac{1}{4}\frac{q^2}{\omega^2} - 4\beta^2} \right)} \quad (5.25)$$

which for $\epsilon = 1 \Rightarrow \Omega = 2\omega + \sigma$ gives

$$a = \pm \sqrt{\frac{1}{\kappa\omega - \frac{3}{4}\frac{\gamma}{\omega}} \left(2\omega - \Omega \pm \sqrt{\frac{1}{4}\frac{q^2}{\omega^2} - 4\beta^2} \right)} \quad (5.26)$$

The solution to (5.2) can then be written as

$$\begin{aligned} y(t) &= \cos\left(\frac{1}{2}(\Omega t - \Psi)\right) + \frac{1}{32}\epsilon \left[\frac{(\gamma - 4\omega^2\kappa)}{\omega^2}a^3 \cos\left(\frac{3}{2}(\Omega t - \Psi)\right) + 2\frac{q}{\omega^2}\cos\left(\frac{3}{2}(\Omega t - \frac{1}{3}\psi)\right) \right] \\ &\quad + \underline{\underline{\mathcal{O}(\epsilon^2)}} \end{aligned} \quad (5.27)$$

An illustration of the stationary amplitude $a(\Omega)$ as a function of the frequency Ω is seen below

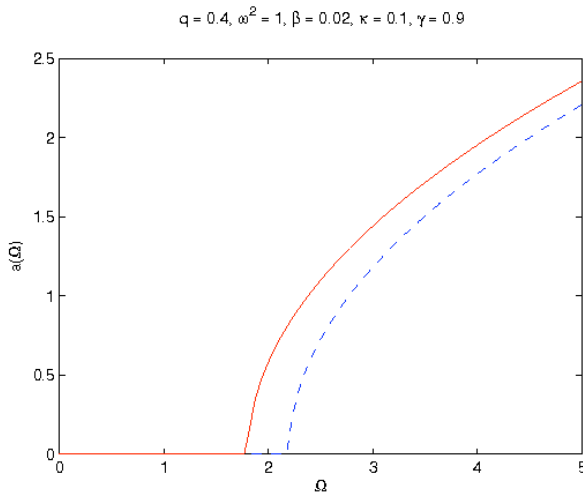


Figure 6: Illustration of the stationary amplitude $a(\Omega)$ as a function of the frequency Ω

The red graph shows the stable solution while the blue graph shows the unstable solution. That the stability is given like that is now proved.

The Jacobian of the system (5.23) and (5.24) is considered and evaluated using (5.25) for which $a' = 0$ og $\Psi' = 0$

$$\mathcal{J} = \begin{bmatrix} 0 & \frac{1}{2}\tilde{a}\left(\left(\frac{3}{4}\frac{\gamma}{\omega} - \kappa\omega\right)\tilde{a}^2 - \sigma\right) \\ \left(-\frac{3}{2}\frac{\gamma}{\omega} + 2\kappa\omega\right)\tilde{a} & -2\beta \end{bmatrix} \quad (5.28)$$

By determine the eigenvalues of the jacobian and utilize that the real part of the eigenvalue for the unstable solution is larger than zero, we arrive at

$$\left[-\frac{3}{4}\frac{\gamma}{\omega} + \kappa\omega\right]\tilde{a}^2 \left(\left[-\frac{3}{4}\frac{\gamma}{\omega} + \kappa\omega\right]\tilde{a}^2 + \sigma\right) < 0 \quad (5.29)$$

Based upon (5.26) the following is defined

$$\tilde{a}_1^2 \left[-\frac{3}{4}\frac{\gamma}{\omega} + \kappa\omega\right] \equiv -\sigma + \sqrt{\frac{1}{4}\frac{q^2}{\omega^2} - 4\beta^2} \quad (5.30)$$

$$\tilde{a}_2^2 \left[-\frac{3}{4}\frac{\gamma}{\omega} + \kappa\omega\right] \equiv -\sigma - \sqrt{\frac{1}{4}\frac{q^2}{\omega^2} - 4\beta^2} \quad (5.31)$$

and by insertion of (5.30) and (5.31) in the right hand side (5.29) we get

- For \tilde{a}_1 : $\left(-\sigma + \sqrt{\frac{1}{4}\frac{q^2}{\omega^2} - 4\beta^2}\right)\left(\sqrt{\frac{1}{4}\frac{q^2}{\omega^2} - 4\beta^2}\right)$

- For \tilde{a}_2 : $\left(-\sigma + \sqrt{\frac{1}{4} \frac{q^2}{\omega^2} - 4\beta^2} \right) \left(-\sqrt{\frac{1}{4} \frac{q^2}{\omega^2} - 4\beta^2} \right)$

It is important to mention that for the given illustration of the amplitude $a(\Omega)$ as a function of the frequency Ω we have that $\left[-\frac{3}{4} \frac{\gamma}{\omega} + \kappa\omega \right] < 0$. Based upon (5.26) we can then conclude that $\left(-\sigma + \sqrt{\frac{1}{4} \frac{q^2}{\omega^2} - 4\beta^2} \right) < 0$ for $\tilde{a}_1, \tilde{a}_2 \in \mathcal{R}$.

Since $\left(\sqrt{\frac{1}{4} \frac{q^2}{\omega^2} - 4\beta^2} \right) > 0$ it can then be concluded that only \tilde{a}_1 fulfills the criterion of being unstable. This case is exactly the blue graph and then the objective is reached: The red graph shows the stable solution while the blue graph shows the unstable solution.

It is well known that the frequency-response function will go to infinity when the excitation frequency goes towards the resonance frequencies (In this case the first natural $\Omega = 2\omega$) if the system considered is linear and without damping. If damping is included in the model the "peak" of the graph illustrating the frequency response relationship will move away from the resonance frequency and be bounded if the system is under external excitation. This is not the case if the system is under parametric excitation, which is the case for the model in this report. To limit the frequency-response function in this case non-linear terms has to be included in the model. If the stiffness introduced by the non-linear terms are at the "softening" type (less than zero), the graph will bend to the left, and if the stiffness is of the "hardening" type (positive) the graph will bend to the right. Thus the peak is not located at the resonance frequencies in the non-linear model.

5.2 b) $\omega^2 < 0$

In this part the analysis for $\omega^2 < 0$ near the primary resonance, $\Omega \approx \sqrt{-2\omega^2}$, is being carried out. This corresponds to a case where the pretension in the spring KQ_0L implies that the beam, at $u(x, t) = 0$, is under the influence of a compressive force which is larger in magnitude than the critical buckling load $P_k = \frac{EI\pi^2}{L^2}$. Furthermore it is assumed that q is sufficiently small such that the beam performs small and finite oscillations about the state of equilibrium $u(x, t) \neq 0$. Finally it is assumed that $\kappa = 0$.

(3.21) then takes the form

$$\ddot{y} + 2\beta\dot{y} + (\omega^2 + q\cos(\Omega t))y + \gamma y^3 = 0 \quad (5.32)$$

By introducing the parameters $\tilde{\omega}^2 \equiv -2\omega > 0$ and $\zeta(t) = y(t) - \tilde{y}$ where \tilde{y} denotes the state of equilibrium $\tilde{y} = \pm\sqrt{\frac{-\omega^2}{\gamma}}$, (which was found under the bifurcation analysis) it is now

possible to rewrite (5.32) as follows

$$\zeta(t) = y(t) - \tilde{y} \Rightarrow \dot{\zeta}(t) = \dot{y}(t) \Rightarrow \ddot{\zeta}(t) = \ddot{y}(t) \Rightarrow \quad (5.33)$$

$$0 = \ddot{y} + 2\beta\dot{y} + (\omega^2 + q\cos(\Omega t))y + \gamma y^3 \Leftrightarrow \quad (5.34)$$

$$0 = \ddot{\zeta} + 2\beta\dot{\zeta} + (\omega^2 + q\cos(\Omega t))(\zeta + \tilde{y}) + \gamma(\zeta + \tilde{y})^3 \Leftrightarrow \quad (5.35)$$

$$0 = \ddot{\zeta} + 2\beta\dot{\zeta} - 2\omega^2\zeta + 3\sqrt{-\omega^2\gamma}\zeta^2 + \gamma\zeta^3 + q\cos(\Omega t)(\zeta + \frac{\mu}{3\gamma}) \Leftrightarrow \quad (5.36)$$

$$0 = \ddot{\zeta} + 2\beta\dot{\zeta} + \tilde{\omega}\zeta + \mu\zeta^2 + \gamma\zeta^3 + q\cos(\Omega t)(\zeta + \frac{\mu}{3\gamma}) \quad (5.37)$$

where $\mu \equiv 3\tilde{\omega}\sqrt{\frac{\gamma}{2}}$. (5.37) denotes the equation of motion for small finite transversal deviations of the beam about the state of equilibrium $\zeta = 0$. The natural frequency is then $\tilde{\omega}^2 \equiv -2\omega > 0$.

It is now assumed that the dynamical part of the load, the damping and all the non-linear terms are "weak" which is identical to say that they are of order $\mathcal{O}(\epsilon)$. Then (5.37) can be rewritten as

$$\ddot{\zeta} + \tilde{\omega}^2\zeta = \epsilon \left(-2\beta\dot{\zeta} - \mu\zeta^2 - \gamma\zeta^3 - q\cos(\Omega t)(\zeta + \frac{\mu}{3\gamma}) \right) \quad (5.38)$$

We assume that the solution of (5.38) can be written on the form

$$\zeta(T_0, T_1) = \zeta_0(T_0, T_1) + \epsilon\zeta_1(T_0, T_1) + \mathcal{O}(\epsilon^2), \quad \epsilon \ll 1, \quad (T_0, T_1) = (t, \epsilon t) \quad (5.39)$$

By insertion of (5.39) in (5.38) we get the following (same procedure as in the case $\omega^2 > 0$)

$$D_0^2\zeta_0 + \tilde{\omega}^2\zeta_0 = 0 \quad (5.40)$$

$$D_0^2\zeta_1 + \tilde{\omega}^2\zeta_1 = -2D_0D_1\zeta_0 - 2\beta D_0\zeta_0 - \mu\zeta_0^2 - \gamma\zeta_0^3 - q\cos(\Omega t)(\zeta_0 + \frac{\mu}{3\gamma}) + cc \quad (5.41)$$

The solution to (5.40) is given by

$$\zeta_0 = A(T_1)e^{i\tilde{\omega}T_0} + \bar{A}(T_1)e^{-i\tilde{\omega}T_0} \quad (5.42)$$

If (5.42) is put into (5.41) the following is found

$$\begin{aligned} D_0^2\zeta_1 + \tilde{\omega}^2\zeta_1 = & \left(-2i\tilde{\omega}A' - 2i\tilde{\omega}\beta A - 3\gamma A^2 \bar{A} \right) e^{i\tilde{\omega}T_0} - \mu A \bar{A} - \mu A^2 e^{2i\tilde{\omega}T_0} - \gamma A^3 e^{3i\tilde{\omega}T_0} \\ & - \frac{1}{2}q \left(A e^{i(\Omega+\tilde{\omega})T_0} + \bar{A} e^{i(\Omega-\tilde{\omega})T_0} + \frac{\mu}{3\gamma} e^{i\Omega T_0} \right) + cc \end{aligned} \quad (5.43)$$

Using $\Omega = \tilde{\omega} + \epsilon\sigma$ we get

$$\begin{aligned} D_0^2\zeta_1 + \tilde{\omega}^2\zeta_1 &= \left(-2i\tilde{\omega}A' - 2i\tilde{\omega}\beta A - 3\gamma A^2 \bar{A} \right) e^{i\tilde{\omega}T_0} - \mu A \bar{A} - \mu A^2 e^{2i\tilde{\omega}T_0} - \gamma A^3 e^{3i\tilde{\omega}T_0} \\ &\quad - \frac{1}{2}q \left(Ae^{2i\tilde{\omega}T_0} e^{i\sigma T_1} + \bar{A}e^{i\sigma T_1} + \frac{\mu}{3\gamma} e^{i\tilde{\omega}T_0} e^{i\sigma T_1} \right) + cc \Rightarrow \\ D_0^2\zeta_1 + \tilde{\omega}^2\zeta_1 &= \left(-2i\tilde{\omega}A' - 2i\tilde{\omega}\beta A - 3\gamma A^2 \bar{A} + \frac{\mu}{3\gamma} e^{i\sigma T_1} \right) e^{i\tilde{\omega}T_0} - \\ &\quad \mu A \bar{A} - (\mu A^2 + \frac{1}{2}qe^{i\sigma T_1}) e^{2i\tilde{\omega}T_0} - \gamma A^3 e^{3i\tilde{\omega}T_0} - \frac{1}{2}q \bar{A} e^{i\sigma T_1} + cc \end{aligned} \tag{5.44}$$

Terms proportional with $e^{i\tilde{\omega}T_0}$ causes secular terms. To get en physical valid solution the following equation then has to be satisfied

$$2i\tilde{\omega}A' + 2i\tilde{\omega}\beta A + 3\gamma A^2 \bar{A} + \frac{\mu}{6\gamma} q e^{i\sigma T_1} = 0 \tag{5.45}$$

If the objective is to determine a solution of (5.32) on the form $y = y_0 + \mathcal{O}(\epsilon)$ we do not have to solve (5.44). To determine $A(T_1)$ modeled by (5.45) we introduce $A(T_1) = \frac{1}{2}ae^{i\varphi}$, $a = a(T_1)$, $\varphi = \varphi(T_1) \in \mathcal{R}$, $\Psi = \sigma T_1 - \varphi \Rightarrow \Psi' = \sigma - \dot{\varphi}$. By insertion of $A(T_1)$ in (5.45) and separation of real and imaginary part we arrive at the following two implicit equations for a og φ .

$$a' = -\beta a - \frac{q}{2\sqrt{2\gamma}} \sin(\Psi) \tag{5.46}$$

$$a\Psi' = -\frac{3}{8}\frac{\gamma}{\tilde{\omega}}a^3 - \frac{q}{2\sqrt{2\gamma}} \cos(\Psi) + \sigma a \tag{5.47}$$

The stationary solutions of (5.46) and (5.47) is found by letting $\Psi' = 0$ og $a' = 0$. The frequency-response relation, $a(\Omega)$ then follows implicit given by

$$\underline{\frac{q^2}{8\gamma} = a^2 \left[\beta^2 + \left(\Omega - \tilde{\omega} - \frac{3}{8}\frac{\gamma}{\tilde{\omega}}a^2 \right)^2 \right]} \tag{5.48}$$

where ϵ is put equal to one, $\epsilon = 1 \Rightarrow \Omega = \tilde{\omega} + \sigma$.

The solution $y(t) = y_0(t) + \mathcal{O}(\epsilon)$ of (5.32) is then given by

$$y(t) = \zeta_0(t) + \sqrt{\frac{-\omega^2}{\gamma}} + \mathcal{O}(\epsilon) = A(T_1)e^{i\tilde{\omega}T_0} + \sqrt{\frac{-\omega^2}{\gamma}} + cc \Rightarrow \tag{5.49}$$

$$\underline{\underline{y(t) = a \cos(\Omega t - \Psi) + \sqrt{\frac{-\omega^2}{\gamma}} + \mathcal{O}(\epsilon)}} \tag{5.50}$$

where cc denotes the complex conjugated and a is given as the solution of (5.48). Below is seen an illustration of the stationary amplitude given implicit by (5.48). Different values of q are used: $q = [0.05, 0.1, 0.2, 0.3, 0.4, 0.5]$. The solution of (5.48) can be found using the MATLAB function "fzero".

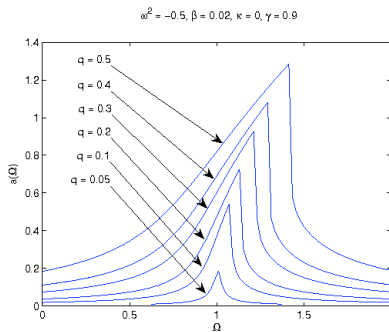


Figure 7: Illustration of the stationary amplitude $a(\Omega)$ as a function of Ω

It should be mentioned, that the part of each curve that follows after the peaking point, is unstable. Ie. the decreasing part of each curve. (Also, compare this illustration with illustration (b) on page 167 in [3]. There is exact agreement between the illustrations).

6 Applying high-frequency input to control the beam stiffness

It is now the objective to carry out an high-frequency (HF) excitation analysis of the beam. The HF excitation has influence on the effective stiffness of the beam and therefore also the effective natural frequencies. It is assumed that Ω is much higher than the fundamental natural frequency ω_1 but still sufficiently smaller than the higher order natural frequencies. In that case (3.21) is still valid as a model for the transversal deflection of the beam with $\Omega \gg \omega_1$. To achieve significant effect when using the HF excitation we let $q = \Omega \hat{q}$ where $\hat{q} \leq \mathcal{O}(\omega)$.

The solution of (3.21) is assumed to be on the form $y(t) = z(t) + \Omega^{-1}\phi(t, \tau)$, $\tau = \Omega t$. Thus the solution consists of a slow component $z(t)$ and a fast component $\phi(t, \tau)$. The objective is now to determine a differential equation governing $z(t)$.

First, note the condition

$$\langle \phi(t, \tau) \rangle \equiv \frac{1}{2\pi} \int_0^{2\pi} \phi(t, \tau) d\tau = 0 \quad (6.1)$$

where $\langle \cdot \rangle$ denotes averaging over a period of time.

Using the chain rule of differentiation we get

$$\frac{dy}{dt} = \dot{z} + \phi' + \Omega^{-1}\dot{\phi} \quad (6.2)$$

$$\frac{d^2y}{dt^2} = \Omega\phi'' + \ddot{z} + 2\phi' + \Omega^{-1}\ddot{\phi} \quad (6.3)$$

where $\dot{\phi} \equiv \frac{\partial \phi}{\partial t}$, $\phi' \equiv \frac{\partial \phi}{\partial \tau}$ and $\frac{d\tau}{dt} = \Omega$.

By insertion of $y(t) = z(t) + \Omega^{-1}\phi(t, \tau)$ and $q = \Omega \hat{q}$ together with (6.2) and (6.3) in (3.21) one gets

$$\begin{aligned} (\Omega\phi'' + \ddot{z} + 2\phi' + \Omega^{-1}\ddot{\phi})(1 + 2\kappa(z + \Omega^{-1}\phi)^2) &= \\ -2\beta(\dot{z} + \phi' + \Omega^{-1}\dot{\phi}) - (\omega^2 + \hat{q}\Omega\cos(\tau))(z + \Omega^{-1}\phi) & \\ -\gamma(z + \Omega^{-1}\phi)^3 - 2\kappa(\dot{z} + \phi' + \Omega^{-1}\dot{\phi})^2(z + \Omega^{-1}\phi) &\Rightarrow \\ (\phi'' + \Omega^{-1}\ddot{z} + 2\Omega^{-1}\dot{\phi}')(1 + 2\kappa z^2 + 4\kappa\Omega^{-1}z\phi) &= \\ -\hat{q}\cos(\tau)z + \Omega^{-1} \left[-\hat{q}\cos(\tau)\phi - 2\beta(\dot{z} + \phi') - \omega^2 z - \gamma z^3 - 2\kappa(\dot{z} + \phi')^2 z \right] + \mathcal{O}(\Omega^{-2}) &\Rightarrow \\ \phi''(1 + 2\kappa z^2) &= -\hat{q}\cos(\tau)z + \Omega^{-1} \left[-\hat{q}\cos(\tau)\phi - 4\kappa z\phi'' - \ddot{z} - 2\kappa z^2 \ddot{z} - 2\dot{\phi}' - 4\kappa z^2 \dot{\phi}' - 2\beta(\dot{z} + \phi') \right. \\ &\quad \left. - \omega^2 z - \gamma z^3 - 2\kappa(\dot{z} + \phi')^2 z \right] + \mathcal{O}(\Omega^{-2}) \quad (6.4) \end{aligned}$$

A first order solution to (6.4) is then given by

$$\phi(t, \tau) = \frac{\bar{q}z}{1 + 2\kappa z^2} \cos(\Omega t) + \mathcal{O}(\Omega^{-1}) \quad (6.5)$$

It is noticed that this equation satisfies (6.1).

By averaging (6.4) under the application of (6.1) we arrive at the differential equation governing $z(t)$

$$\ddot{z} + 2\beta\dot{z} + \left(\omega^2 + \frac{1}{2} \frac{\hat{q}}{1 + 2\kappa z^2}\right)z + \gamma z^3 + 2\kappa(z\ddot{z} + \dot{z}^2)z = 0 \quad (6.6)$$

The solution of (3.21) is then given by

$$y(t) = z(t) + \Omega^{-1} \frac{\bar{q}z}{1 + 2\kappa z^2} \cos(\Omega t) + \mathcal{O}(\Omega^{-2}) \quad (6.7)$$

where $z(t)$ is given as a solution of (6.6).

Comparing (6.6) to (3.21) it is seen that $z(t)$ is governed by a differential equation of the same form as the original equation (single mode approximation) describing the system. Also it is seen that the HF excitation has an influence on the stiffness term in (3.21), $(\omega^2 + q \cos(\Omega t))y$. This term undergoes a change from being autonomous to non-autonomous.

Cf. the definition on page 294 in [1] of "restoring force", $f_r(z)$, we see from (6.6) that

$$f_r(z) = \left(\omega^2 + \frac{1}{2} \frac{\hat{q}}{1 + 2\kappa z^2}\right)z \quad (6.8)$$

The effective stiffness at the equilibrium point $y = z = 0$, defined on page 294 in [1], is then given by

$$f'_r(0) = \omega^2 + \frac{\hat{q}}{2} \quad (6.9)$$

Based on that observation we can conclude that the HF excitation changes the fundamental frequency in the system from being $\sqrt{\omega_1}$ to $\sqrt{\omega_1 + \frac{\hat{q}}{2}}$. Further that stability of the equilibrium point $y = 0$ for $\omega_1 > 0$, remains stable.

Thus the HF excitation increases the natural frequency in the system.

If a Taylor-expansion of (6.6) is carried out we get

$$\left(\omega^2 + \frac{\hat{q}}{1 + 2\kappa z^2}\right)z = \left(\omega^2 + \frac{\hat{q}}{2}\right)z - \kappa\hat{q}z^3 + \mathcal{O}(z^5) \quad (6.10)$$

Considering the sign of the dominating non-linear term in (6.10), $-\kappa\hat{q}z^3$ it can be concluded that the HF excitation implies a "softening" in the system about the equilibrium point $z = 0$.

7 Simulation program

To carry out a numerical examination of the beam system, creation of MATLAB codes is now the objective. The program has to be capable of creating time series, phase plane illustrations, Poincare-maps and frequency spectra illustrations. Further it should be possible to get the largest Lyapunov-exponent.

A print of the codes can be viewed in appendix B.

Overall 5 MATLAB functions are used: `solution`, `lyap1`, `fft_dB`, `diffsystem1` and `diffsystem2`. `solution` which is created by me is the main function. It holds two sub-functions `diffsystem1` and `diffsystem2` in which the first order differential equations system are implemented. Depending on what the objective is `solution` calls `lyap1` or `fft_dB` (which are made by JJT). `solution` consist of five if-statements which are controlled by the user of the program. The statement that is used in the given calculation depends on the objective. Thus, in the first statement calculations of the time series are carried through. In the second statement the phase plane is being calculated. In the third statement the Poincare-map is calculated. In the fourth statement the frequency spectra is found and in the fifth statement the largest Lyapunov-exponent are calculated.

In the top of `solution` the user specifies the values of the parameters used to identify the system and also the values used as initial conditions. After the call of the function the wanted calculation together with the illustrations are carried out.

8 Numerical analysis

In this section a numerical analysis of the beam system is carried out. The MATLAB functions described in the foregoing section is used in the analysis. It is important to mention that the parameter values used in the single calculation and corresponding illustration (series of illustrations) is denoted in the top of the illustration.

8.1 a)

The objective is to make an illustration of the transient response for $q = 0$, $y(0) = 0$, $\dot{y}(0) = 0.1$ and respectively for $\omega^2 = 1$ og $\omega^2 = -\frac{1}{2}$. These can be viewed in the bottom of this page.

From the illustrations we immediately conclude that we observe what we would expect. In illustration one the beam settles down in the equilibrium configuration $y = 0$ which was expected cf. the analysis made in section four (note that the attenuation coefficient of the damping is different from zero). In the second illustration the beam settles down in an equilibrium configuration with maximal deflection equal to $y \approx 0.7453$. According to the analysis made in chapter four this value should be equal to $\sqrt{\frac{-\omega^2}{\gamma}} = \frac{\sqrt{5}}{3} \approx 0.745356$. The conclusion is then that there is an completely acceptable agreement between theory and numerical analysis. Further this observation confirms the bifurcation that takes place at $(y, v, \omega^2) = (0, 0, 0)$. It should be mentioned that the beam settles down in $y = \sqrt{\frac{-\omega^2}{\gamma}}$ instead of $y = -\sqrt{\frac{-\omega^2}{\gamma}}$ as a consequence of the initial conditions.

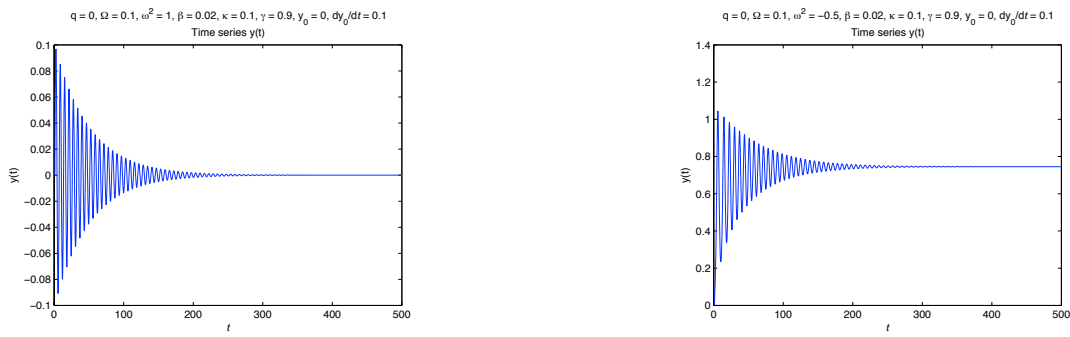


Figure 8: Plot of the transient response

8.2 b)

The objective is now to carry out an examination of the quantitative predictions made in subsection 5(a), for $q \ll 1$, $\omega^2 = 1$, $\Omega \approx 2\omega$. Hence the goal is to confirm that the theoretic expression of the stationary amplitude (5.26) is in agreement with the numeric solution. Five investigations are made using $q = 0.1, 0.2, 0.3, 0.4, 0.5$ and $\beta = 0.02, \gamma = 0.9, \kappa = 0.1$ and $y(0) = \dot{y}(0) = 0.01$. Below is shown a scheme showing the theoretic and numeric values. (r.d stands for relative deviation, $r.d = \frac{a_{\text{theoretic}} - a_{\text{numeric}}}{a_{\text{theoretic}}}$)

q	0.1	0.2	0.3	0.4	0.5
amplitude, theoretic	0.2284	0.3992	0.5014	0.5838	0.6551
amplitude, numeric	0.2272	0.3948	0.4929	0.5704	0.6362
r.d	0.005	0.011	0.017	0.023	0.029

As can be seen from the scheme the relative deviation increases with q . Despite that fact, the relative deviation seems to be "small" enough (acceptable) to conclude that there is acceptable agreement between theory (expression (5.26)) and the numerically found result for $q = 0.1, 0.2, 0.3, 0.4, 0.5$.

Furthermore illustrations of the frequency spectra and phase plane are made for $q = 0.2$. The result are seen below on this page.

As can be seen on the illustration of the frequency spectra two frequencies are dominating. One of them does precisely coincide with the first natural frequency $\omega = 1 \Rightarrow f = \frac{1}{2\pi} = 0.159$. Also if we compare both these two illustration with the first one on page 271 in [1], it seems that we observed what we would expect, meaning, a finite number of domination frequency in the frequency spectra is associated with a period one orbit in the phase plane.

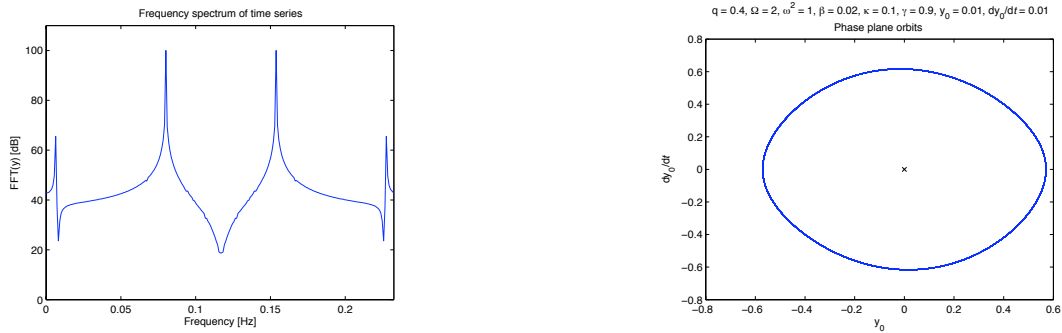


Figure 9: Illustration of the frequency spectra and the phase plane

8.3 c)

The objective is now to investigate the qualitative predictions made in subsection 5(b), for $q \ll 1$, $\omega^2 = -\frac{1}{2}$, $\Omega \approx \tilde{\omega}$, $\kappa = 0$, $\beta = 0.02$, $\gamma = 0.9$, $y(0) = 0.01$, $\dot{y}(0) = 1.01$. The analysis is carried out in a similar way that was done in the previous subsection. Now the comparison is made with the expression (5.48). Below is seen a scheme with the results

q	0.0005	0.001	0.002	0.003	0.004	0.01	0.1
amplitude, teori	0.00931	0.0186	0.0373	0.0558	0.0742	0.1681	0.4744
amplitude, numerisk	0.00932	0.0186	0.0370	0.0545	0.0701	0.1236	0.2622
f.a	0.001	0.001	0.008	0.023	0.055	0.265	0.447

As can be seen from the scheme the theoretic expression (5.48) is in good agreement with the numerically found results as long as $q \ll 1$. When q approaches the order 10^{-2} it can be seen that the error is to large for the model to be satisfactory.

Further, an illustration of the frequency spectra and the phase plane is shown in the bottom of this page for $q = 0.001$ and the rest of the parameters given as above stated.

Observe that again it is the case that the first "spike" coincides with the first natural frequency $\omega^2 = -\frac{1}{2} \Rightarrow \tilde{\omega} = 1 \Rightarrow f = 0.159$. Also the qualitative look of the illustrations are similar with those on page 271 in [1]. Thus cf. the argumentation made in the previous subsection we conclude that the observed illustration is in good agreement with what we would expect.

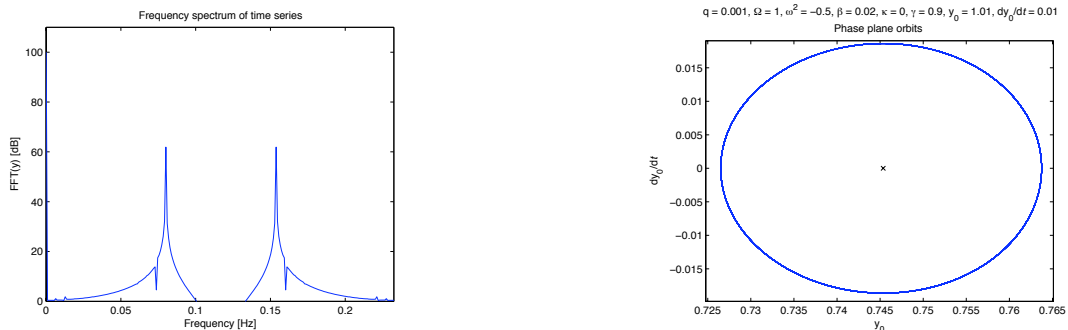


Figure 10: Illustration of the frequency spectra and the phase plane

8.4 d)

The objective is now to carry out an analysis of the frequency response relationship given by (5.26) for different values of Ω and all other parameters hold constant. This is identical to the procedure of following a curve of the amplitude. An illustration of this is seen below. Note that the red curve is the theoretical solution of the amplitude while the blue crosses are the numerically discrete solution. Also, the lower illustration is a zoom of the first plot. By observing the illustrations we conclude that there is extremely good correspondence between theory and the numerically found result until we reach the value $\Omega \approx 2.15$. At that point the numerical solution jumps to the zero solution $a \approx 0$. That we do not observe correspondence is actually not a surprise since the mathematical expression (5.26) does not take that particular feature of the physical systems into account. What I am trying to say here is that what we observe is exactly what we would expect; The mathematical model simply does not take this feature into account. (Simply compare the numerical result with the illustration (a) on page 169 in [3], then it is clear that what is observed is exactly in agreement with what we would expect).

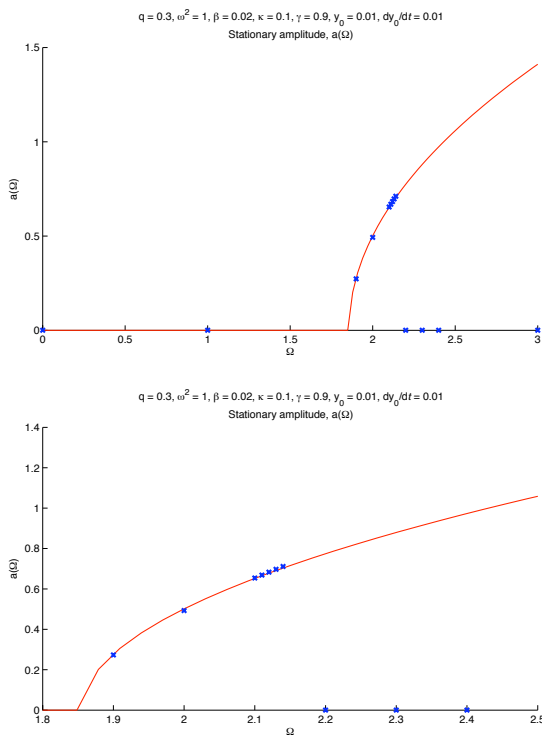


Figure 11: Illustration of the stationary amplitude, a

8.5 e)

The objective is now to find a chaotic solution/response of the beam when $\omega^2 < 0$. Lets us choose $\omega^2 = -\frac{1}{2}$. Also $\Omega < 4$ and $q < 1$. The initial conditions are set to $y(0) = 1.01$ and $\dot{y} = 0.01$. Below is seen an illustration of the phase plane, the Poincare-map, the largest Lyapunov exponent and the frequency spectra for the described configuration of the system

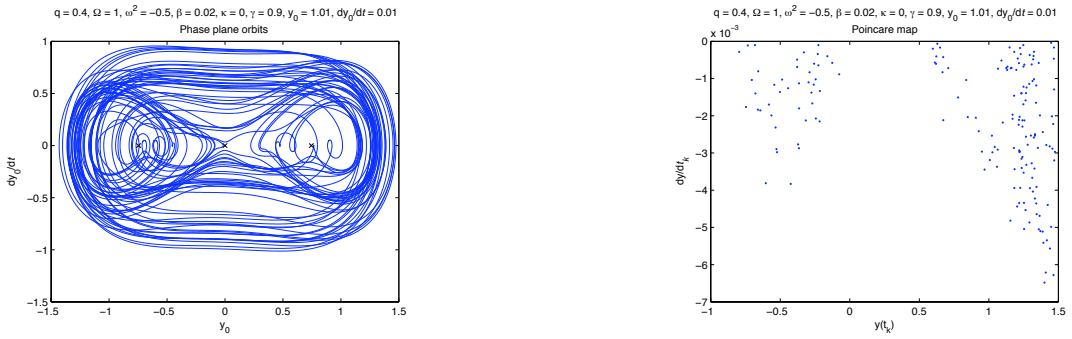


Figure 12: Illustration of the phase plane and the Poincare map

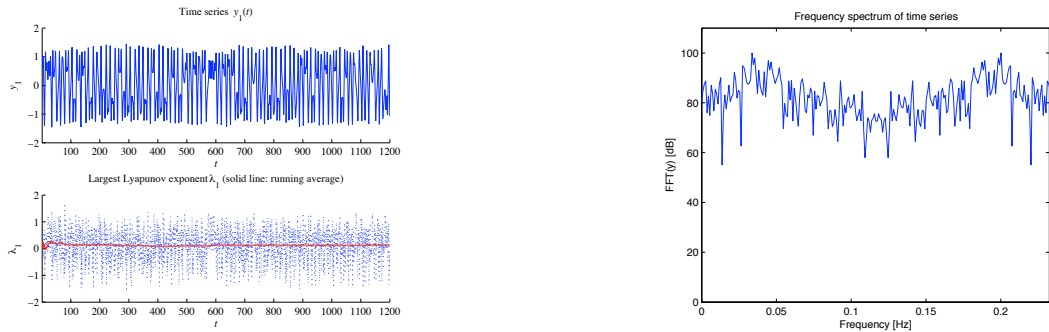


Figure 13: Illustration of the largest Lyapunov exponent and the frequency spectra

An important fact to mention is that the largest Lyapunov exponent is found to be $\lambda_{max} = 0.13199$ which proves that the above example is chaotic. That the response indeed is chaotic is further supported by the three other illustrations. (Note that the transient response has been cut away because we are only interested in the steady state solution); The trajectory in the phase plane does not seem to repeat itself. Also this is true for the Poincare map. And by the frequency spectra we conclude that all frequencies are represented, which also indicates chaos.

Furthermore the objective is to make an investigation of the "route to chaos". This is carried out by considering the Poincare map, the phase plane and the largest Lyapunov exponent for different values of Ω and all other parameters hold constant. Ω is being varied from the lower boundary $\Omega_{min} = 0.001$ to the upper boundary $\Omega_{max} = 0.225$. The upper boundary is chosen so since chaotic behavior is observed for this value (recall the objective is to investigate the "route to chaos"). Below is seen a series of illustrations of the phase plane and the Poincare map for different values of Ω . Furthermore the largest Lyapunov exponent is shown in a scheme under the series of illustrations

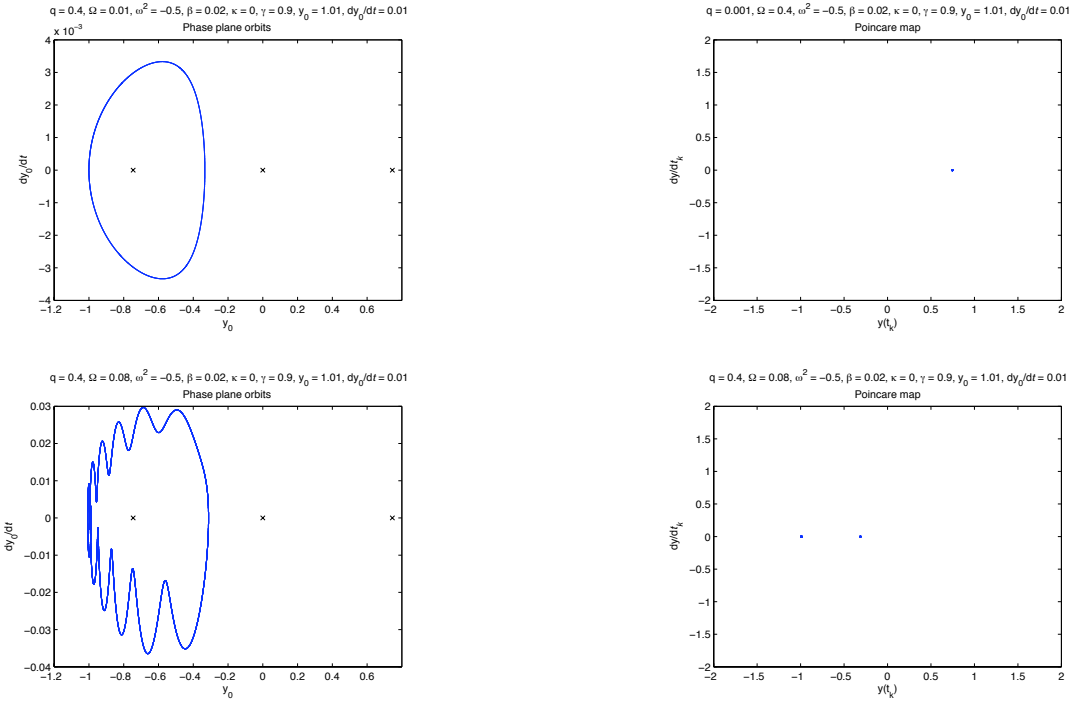


Figure 14: Illustrations of the phase plane and Poincare map for different values of Ω

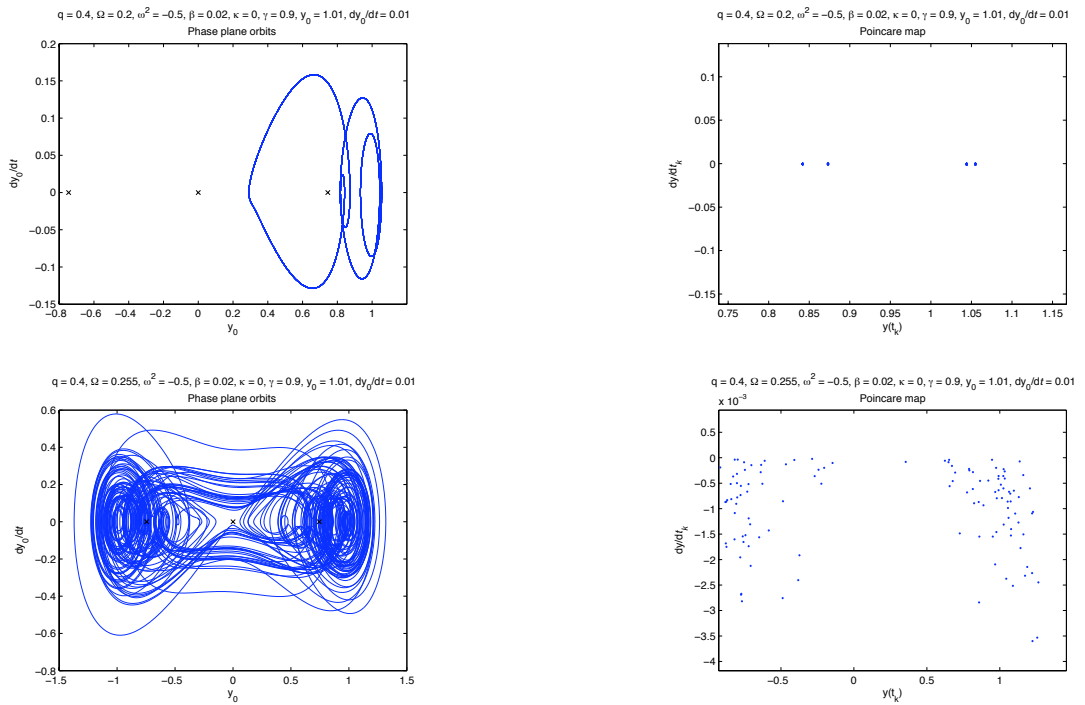


Figure 15: Illustrations of the phase plane and Poincare map for different values of Ω

Ω	0.01	0.08	0.2	0.255
λ_{max} ,	-0.00015	-0.00038	-0.00061	0.062

Considering the values in the scheme it is observed that the first three values of Ω are cause for motions that are NOT chaotic in behavior (The largest Lyapunov exponent is negative). But for the fourth value of Ω we do indeed observe chaotic behavior since the value of the largest exponent is positive. By considering the series of illustrations it seems right to conclude that the "route to chaos" contains the phenomenon period doubling. Also it should be mentioned that calculations for several other values of Ω and for different periods of time has been carried out. The observation here was that the largest Lyapunov exponent changed sign from positive to negative when the time was increased. This behavior shows that the solution for the given Ω is NOT chaotic but it also indicates that the "route" to chaos also contains the phenomenon "Intermittent" route to chaos. Furthermore, some calculations showed effects that indicates the existence of the phenomenon "Transient" route to chaos. What was not observed was "Quasi periodic" route to chaos.

9 Conclusion

Through the analysis of the simply supported beam system it has been recognized that the mathematical theoretical single form approximation and the numerical calculations are in good agreement as long as the outlined conditions for the range of validity of the single form approximation is satisfied. It was seen that a qualitative change in the system happened when the sign of the square of the natural frequency changes from positive to negative (identical to say that a bifurcation happens). The effect of this is that the dynamics of the system undergoes a change such that the beam oscillates away from the undeformed state of equilibrium when the sign of the square of the natural frequency is negative. Depending upon damping the beam will continue to oscillate or finally settle down in a deformed equilibrium configuration.

Further it was observed that for specific chosen values of the parameters describing the system, chaotic behavior of the beam did occur. If control of the behavior of the system is the objective, these parameter configuration giving rise to chaos should be avoided. To ensure control of the response of the system, it is recommended that the value of the external load does not exceed the critical buckling load since this will ensure that of the square of the natural frequency is positive and hence that chaos is avoided. Furthermore, obeying this restriction also ensures that the correspondence between theory and numeric is good, since it was observed that for negative values of the square of the natural frequency the external load does not have to be "large" before the difference between the theoretical and numerical calculated value of the stationary amplitude becomes critical "large".

Finally it should be mentioned that High Frequency excitation (HF) should not be used as a control of the external load since the effect of this is a "softening" in the system, which does not have a positive effect on the stability of the system.

10 Appendix A, list of sources

[1]: Thomsen JJT (2003) Vibrations and stability, Advanced Theory, Analysis and Tools, vol. 2, Springer-Verlag, New York.

[2]: Nayfeh and Balachandran (1995), Applied Nonlinear Dynamics, Wiley.

[3]: Nayfeh and Mook (1995), Nonlinear Oscillations, Wiley.

11 Appendix B, source code for the simulation program

```
% This MATLAB function creates times series, phase plane plots,
% Poincaré maps, frequency spectras and calculates the largest Lyapunov
% exponent for the beam system.

% Jacob Ajslev Hersboell, s022020

function [T,Y] = solution(choice,t1,t2,y0,dify0)

choice = choice; % used to identify what the program should
% do

t1 = t1; % starting time
t2 = t2; % ending time

y0 = y0; % initial deflection
dify0 = dify0; % initial velocity

ODEparameters.omega = 1; % natural frequency
ODEparameters.Omega = 2; % excitation frequencs
ODEparameters.beta = 0.02; % damping
ODEparameters.kappa = 0; % rigid point mass
ODEparameters.gamma = 0.9; % stiffness
ODEparameters.q = 0.2; % excitation amplitude

WithVariationalEqs = false;

SystemParameters = ... % used to create labels
[ 'q = ' num2str(ODEparameters.q) ...
, '\Omega = ' num2str(ODEparameters.Omega) ...
, '\omega^2 = ' num2str(ODEparameters.omega) ...
, '\beta = ' num2str(ODEparameters.beta) ...
, '\kappa = ' num2str(ODEparameters.kappa) ...
, '\gamma = ' num2str(ODEparameters.gamma) ...
, 'y_0 = ' num2str(y0) ...
, 'dy_0/dt = ' num2str(dify0) ];
% used in ODE45

options = odeset('RelTol',1e-10,'Abstol', 1e-10);
clf
```

```

if choice == 1 % time series
    % solves the diff. system
    [T1,Y1] = ode45(@diffsystem1,[t1 t2],...
        [y0 dify0 ODEparameters.Omega*t1],options);

    plot(T1(length(Y1)-1/2*length(Y1):end,1)...
        ,Y1(length(Y1)-1/2*length(Y1):end,1));
    title({SystemParameters; 'Time series y(t)'});
    xlabel('\itt'); ylabel('y(t)');
        % amplitude calculated numerically
    stationary_numeric = (max(Y1(length(Y1)... -1/2*length(Y1):end,1))-min(Y1(length(Y1)-1/2*length(Y1):end,1)))/2

elseif choice == 2 % Poincaré
    % solves the diff. system
    [T1,Y1] = ode45(@diffsystem1,[t1 t2],...
        [y0 dify0 ODEparameters.Omega*t1],options);

        % sign of velocity used in calculating the
        % Poincaré map
    signs = sign(Y1(round(length(Y1)/2):end,2));
    j = 1;
    for i = 1:length(signs)-1
        if signs(i+1) ~= signs(i) & signs(i+1) == -1
            point1(j) = Y1(i+round(length(Y1)/2),1);
            point2(j) = Y1(i+round(length(Y1)/2),2);
            j = j+1;
        end
    end

    plot(point1, point2, '.')
    title({SystemParameters; 'Poincaré map'});
    xlabel('y(t_k)'); ylabel('d{y}/d{\itt_k}');

elseif choice == 3 % phase plane
    % solves the diff. system
    [T1,Y1] = ode45(@diffsystem1,[t1 t2],...
        [y0 dify0 ODEparameters.Omega*t1],options);

    plot(Y1(length(Y1)-1/2*length(Y1):end,1),...
        Y1(length(Y1)-1/2*length(Y1):end,2))

```

```

hold on
    % stationary points
if ODEparameters.omega > 0
    plot(0,0, 'x k')
elseif ODEparameters.omega < 0
    y_tilde1 = sqrt(-ODEparameters.omega/ODEparameters.gamma);
    y_tilde2 = -sqrt(-ODEparameters.omega/ODEparameters.gamma);
    plot(0,0, 'x k',y_tilde1,0, 'x k',y_tilde2,0, 'x k')
end

title({SystemParameters, 'Phase plane orbits '});
xlabel('y_0'); ylabel('d{y_0}/d{itt}');

elseif choice == 4           % frequency spectra

N = 512;

T = t2 - t1;                 % total sampling time
dt = T / (N-1);              % sampling interval
t = t1 : dt : t2;            % sampling instances
fs = 1/dt;                   % sampling frequency
fNyq = 1/2*(N-1)/ T;         % Nyquist frequency

[T1,Y1] = ode45(@diffsystem1,t,[y0 dify0 ODEparameters.Omega*t1]);
y = Y1(length(Y1)-1/2*length(Y1):end,1);

disp(['Nyquest frequency: ' num2str(fNyq)]);

LP_filter = false;           % should the time series be lowpass filtered?

if LP_filter
    CutoffFrequency = 0.95*fNyq;
    FilterOrder = 5;
        % in dB down from the peak passband valueStopBandRipple
    StopBandAttenuation = 20;
        % larger values => wider transition widths (shallow roll-off)
[filterCoeff1, filterCoeff2] = cheby2(FilterOrder, ...
    StopBandAttenuation, CutoffFrequency/fNyq);
    y = filter(filterCoeff1, filterCoeff2, y);
end

```

```

        % calcultate FFT
dBmax = 100;           % Scales output to max at this value
% Function fft_dB is defined below
[xFFTdB, fFFT, nFFT, fNyq] = fft_dB(y,N,T,dBmax);

plot(fFFT,xFTdB(1:nFFT),'-b');      % plot FFT
axis([0 fNyq 0 1.1*dBmax]);
xlabel('Frequency [Hz]'); ylabel('FFT({y}) [dB]');...
title('Frequency spectrum of time series');

elseif choice == 5          % Lyaponov exponet

WithVariationalEqs = true;
                           % initial conditions to the diff system
InitialConditions = [y0 dify0 ODEparameters.Omega*t1];
t_transient = t1;
t_stop = t2;
nSimTimeSteps = 10;
timestep_Lyap = 2*pi/ODEparameters.Omega /nSimTimeSteps
GraphicalOutput = true;
NumericalOutput = true;
NumOutputPoints = 100;
lambda1 = lyap1(@diffsystem2,ODEparameters,InitialConditions, ...
    t_transient,t_stop,timestep_Lyap, ...
    GraphicalOutput,NumericalOutput,NumOutputPoints);
disp(['Result of calling lyap1: lambda1 = ',num2str(lambda1)]);

end

% In this MATLAB function the first order differential system that
% describes the physical system: Beam system is implemented.

% Jacob Ajslev Hersboell, s022020

function df = diffsystem1(t,y)

df(1,1) = y(2);
df(2,1) = -(2*ODEparameters.beta*y(2)+2*ODEparameters.kappa*y(2)^2*y(1)...
+(ODEparameters.omega+ODEparameters.q*cos(y(3)))*y(1) ...
+ODEparameters.gamma*y(1)^3)/(1+2*ODEparameters.kappa.*y(1)^2);

```

```
df(3,1) = ODEparameters.Omega;
end

% In this MATLAB function the first order differential system that
% describes the physical system: Beam system, and the variational equations
% are implemented.

% Jacob Ajslev Hersboell, s022020

function df = diffsystem2(t,y,ODEparameters,WithVariationalEqs)

df(1,1) = y(2);
df(2,1) = -(2*ODEparameters.beta*y(2)+2*ODEparameters.kappa*y(2)^2*y(1)...
            +(ODEparameters.omega+ODEparameters.q*cos(y(3)))*y(1) ...
            +ODEparameters.gamma*y(1)^3)/(1+2*ODEparameters.kappa*y(1)^2);
df(3,1) = ODEparameters.Omega;

if (WithVariationalEqs)
    df(4,1) = y(5);
    df(5,1) = ( -(2*ODEparameters.kappa*y(2).^2+...
                  (ODEparameters.omega+ODEparameters.q*cos(y(3)))... 
                  +3*ODEparameters.gamma*y(1).^2)... 
                  *(1+2*ODEparameters.kappa.*y(1).^2)... 
                  +(2*ODEparameters.beta*y(2)+2*ODEparameters.kappa*y(2).^2.*y(1)...
                  +(ODEparameters.omega+ODEparameters.q*cos(y(3))).*y(1)...
                  +ODEparameters.gamma*y(1).^3)*(4*ODEparameters.kappa*y(1)) )/...
                  (1+2*ODEparameters.kappa.*y(1).^2).^2*y(4)...
                  -(2*ODEparameters.beta+4*ODEparameters.kappa*y(2).*y(1))/...
                  (1+2*ODEparameters.kappa.*y(1).^2)*y(5)...
                  +((ODEparameters.q*sin(y(3))).*y(1))/...
                  (1+2*ODEparameters.kappa.*y(1).^2)*y(6);
    df(6,1) = 0;
end
end
end
-----  
-----  
-----
```

```
function [xFTdB, fFFT, nFFT, fNyq] = fft_dB(x,N,T,dBmax);
% Compute the FFT of a uniformly sampled time series, in the form typically
% used for vibration analysis.
%
% INPUT
%     x: Vector containing the uniformly sampled time series to be FFT'ed
%     N: Length of x
%     T: Total sampling time
%     dBmax: Max dB-value wanted for the FFT
%
% OUTPUT
%     xFTdB: Vector containing the FFT of x, given as magnitude (i.e. |FFT(x)|),
%             and scaled to [..;100dB]
%     fFFT: Vector of frequencies corresponding to the elements in xFTdb
%     nFFT: Number of elements in xFTdb and fFFT
%     fNyq: Nyquist frequency (=largest value in fFFT)
%
% NOTES:
% (1) IMPORTANT: Be sure to bandlimit the input.
% It is very important that x(t) does not contain frequencies larger
% than the Nyquist frequency, fNyq = 1/2*fs, where fs = (N-1)/T is the
% sampling frequency. Should such frequencies occur, the FFT-algorithm will
% map them as frequencies below f_Nyq, as socalled aliasing frequencies.
% It is NOT possible to distinguish between an aliasing frequency and a
% "real" frequency. The only way to avoid aliasing is to ensure, typically
% by lowpass filtering, that the time series is band-limited to [0;f_Nyq]
%
% (2) No windowing (e.g. Hanning or exponential) of the time series is
% applied; feel free to window the timesignal before FFT'ing it
%
% (3) Some books on frequency analysis:
% - Randall, R. B., Frequency Analysis, Brüel & Kjær, Copenhagen, 1987.
% - Ewins, D. J., Modal Testing: Theory and Practice, Wiley, New York, 1984.
%
% JJT / 12.3.2004
%
-----  
dt = T / (N-1);      % Sampling interval
fs = 1/dt;           % Sampling frequency
fNyq = 1/2*fs;       % Nyquist frequency
df = 1/T;            % Frequency resolution
nFFT = N/2 + 1;       % (useful) Length of the FFT (the remaining N/2-1
```

```

    %points are not used)
xFFT = fft(x);           % Use MATLAB's function fft to Fourier
                          %transform the time series
                          % Constant needed for calculating dB
                          % Definition: [dB] = 20*log(SignalValue/SignalReferenceValue)
dBnorm = 100 - 20*log10(max(abs(xFFT)));
                          % For displaying the FFT: calculate |xFFT| in dB.
xFTtdB = 20*log10(abs(xFFT)) + dBnorm;
                          % Frequency lines corresponding to the FFT-components
fFFT = 0 : df : (nFFT-1)*df;
-----
-----
-----
%-----
function lambda1 = lyap1(ODEfunHandle,ODEparameters,InitialConditions,...
                         t_transient,t_stop,timestep_Lyap,...
                         GraphicalOutput,NumericalOutput,NumOutputPoints)
% Estimate the largest Lyapunov exponent lambda1 for a system
% dy/dt = f(y), y=[y1;y2;...;YN] of N 1st-order differential equations,
% using the procedure given refrence [4] below, eqs. (6.5)-(6.7).
%
% OUTPUT
% lambda1: Estimated largest Lyapunov exponent
%
% INPUT
% ODEfunHandle: Handle to a user-supplied function defining the ODEs,
% along with their variational equations, following the syntax:
% dy = ODEfun( t, y, ODEparameters, WithVariationalEqs)
% The function is constructed as for the MATLAB ODE-solvers (e.g. see
% ode45) for the first N equations, and then augmented by N variational
% equations for computing dy(N+1),...,dy(2*N), cf. the example given
% in 'lyap1_test'. The ODE-function should only compute the variational
% equations when the parameter WithVariationalEqs is true/1.
% ODEparameters: Struct defining the ODE-parameters.
% InitialConditions: Row vector defining y at time zero;
% t_transient: Transient cutoff-time, i.e.: the solution for
% t=[0:t_transient] is first computed, and then discarded as transients
% before lambda-estimation is intiated.
% t_stop: Final time; lambda1-estimation is performed for t=[t_transient:
% tstop]
% timestep_Lyap: Timestep used when estimating the local value of lambda1.

```

```
% Choose this value sufficiently small so as to capture the local
% 'stretches' while avoiding the global 'folds'. E.g., choose a
% timestep
% equal to a small fraction (e.g. 1/10) of one period of a
% characteristic
% oscillation frequency (e.g. the excitation frequency, if there is one).
% Note that this timestep can be much larger than the internal timestep
% used by the ODE-solver.
% GraphicalOutput: true/false: Show / don't show lambda1-convergence
% graphically (true=>slower performance)
% NumericalOutput: true/false: Output / don't output running
% lambda1-averages
% NumOutputPoints: Approx. number of intermediate lambda1-values in output
%
% REMARKS
% If GraphicalOutput and NumericalOutput are both false, lyap1 outputs
% nothing but the output parameter lambda1.
% With GraphicalOutput the iterations can be interrupted by pressing
% 'q' on the keyboard when the figure is active; the last running
% average of lambda1 is then output. Note that program execution is
% slower with GraphicalOutput.
%
% EXAMPLE USAGE
% See the separate function 'lyap1_test'
%
% REFERENCES
% [1] A. Wolf et al.: 'Determining Lyapunov exponents from a time series',
% Physica 16D (1985) 285-317.
% [2] T.S. Parker and L.O. Chua: 'Practical Numerical Algorithms for
% Chaotic Systems', Springer-Verlag, New York, 1989.
% [3] F.C. Moon: 'Chaotic Vibrations', Wiley, New York, 1987.
% [4] J.J. Thomsen: 'Vibrations and Stability (2nd ed.)', Springer, 2003.
% Refs. [1-3] also describe how to estimate the full spectrum of Lyapunov
% exponents, and (at least [1]) how to estimate Lyapunov exponents from
% experimentally obtained time series.
%
% VERSION HISTORY
% v1.0: April 10, 2006
% [Jon Juel Thomsen, MEK, Tech. Univ. of Denmark]
```

```
% Function initializations
global KeyPressed_q; KeyPressed_q = false;
WithVariationalEqs=true; SkipVariationalEqs=false;

% Check input
ValidTimes = (t_transient > 0) & (t_stop > t_transient)...
    & (timestep_Lyap < t_stop-t_transient) ;
if ~ValidTimes
    error(['Input times must satisfy',...
        '0<t_transient<t_stop & timestep_Lyap<t_stop-t_transient']);
end

% Prepare augmented initial conditions vector
N = length(InitialConditions);
y0 = zeros(1,2*N);
y0(1:N) = InitialConditions;

% Solve dy/dt = f(y) for some time to get rid of transient, i.e
% t=[0;t_transient].
if NumericalOutput
    disp('-----');
    disp('Start transient simulation ...');
end
[t,y_transient] = ode45( ODEfunHandle,[0 t_transient],...
    InitialConditions,[],ODEparameters,SkipVariationalEqs);
if NumericalOutput disp('... end transient simulation ...'); end

% Then solve for t=[t_transient; t_stop], or to user interrupts
% by pressing 'q':

% First some preparations:
t_start = t(end); % = t_transient
nPostTrans = (t_stop-t_transient)/timestep_Lyap + 1;
t_end = t_start + timestep_Lyap;
y0(1:N)=y_transient(end,1:N); % Use postransient solution
                                % point as initial condition
y0(N+1:2*N)=1/sqrt(N); % for the VARIATIONAL system of
                           % dy/dt = f(y); unit-normalized
if NumericalOutput
    NumOutputRate=round(nPostTrans/NumOutputPoints);
    disp('Start post-transient simulation ...')
```

```

end
if GraphicalOutput
    clf;
    set(gcf,'KeyPressFcn',@KeyPressq)
    figure(1);
    disp('... Press ''q'' in the figure window to interrupt ...')
    ylim1_old=[4711 4711]; ylim2_old=[4711 4711];
end
lambda1_local_k=0; lambda1_RunningAverageOld=0; nav=0;

% Then iterate small timesteps (= timestep_Lyap) ahead:

while (t_end < t_stop)
    [t,y] = ode45( ODEfunHandle, [t_start, t_end], y0, [], ...
                  ODEparameters,WithVariationalEqs);
    if GraphicalOutput
        subplot( 2, 1, 1 )
        hold on;
        % Plot time series (add new point)
        plot([t_start,t_end],[y0(1),y(end,1)],'-b');
        ylim1_changed = ( ylim ~= ylim1_old );
        if ylim1_changed
            set(gca,'fontsize',10,'fontname','Times New Roman');
            title( 'Time series \{ity\}_1(\{itt\})' )
            xlabel('\itt'); ylabel('{ity}_1');
            xlim([t_transient t_stop]); % axis limits
        end
        ylim1_old = ylim;
    end

    % Calculate local Lyapunov exponents and running average,
    % using eqs. (6.6)-(6.7) in Thomsen: "vibrations and Stability" (2003)
    norm_eps_k = 1; % Since the init.conds. for the variational eqs.
                    %are unit-normalized
    norm_eps_kPlus1 = norm(y(end,N+1:2*N));
    lambda1_local_kPlus1=1/timestep_Lyap*log2(norm_eps_kPlus1/norm_eps_k);
    nav = nav+1;
    lambda1_RunningAverageNew = (lambda1_RunningAverageOld*(nav-1)...
                                + lambda1_local_kPlus1)/nav;

    % Plot average largest Lyapunov exponent (add new runinng average)

```

```

if GraphicalOutput
    subplot( 2, 1, 2 )
    hold on;
    plot([t_start,t_end],[lambda1_local_k,lambda1_local_kPlus1],...
          ':b','linewidth',1);
    plot([t_start,t_end],[lambda1_RunningAverageOld,...
        lambda1_RunningAverageNew],...
          '-r','linewidth',1.5);
    ylimCur = ylim;
    ylim2_changed = ( ylimCur ~= ylim2_old );
    if ylim2_changed
        set (gca,'fontsize',10,'fontname','Times New Roman');
        xlabel('t'); ylabel('lambda_1');
        xlim([t_transient t_stop]); % axis limits
        title('Largest Lyapunov exponent {\it\lambda}_1(solid line: running average)');
        %%legend('{\it\lambda}_1(\it t)', '{\it\lambda}_1 (av.)');
        %%legend('boxoff');
        %% NOT used: Legend slows done live update of the figure a lot
    end
    ylim2_old = ylim;
    drawnow
    if KeyPressed_q break; end % check if user wants to interrupt
end

% Renormalize initi.cond. for the variational equations, and prepare for
% the next timestep
y0(1:N) = y(end,1:N); % For the system odes
y0(N+1:2*N) = y(end,N+1:2*N)/norm_eps_kPlus1; % for the variational eqs.
t_start = t_end;
t_end = t_start + timestep_Lyap;
lambda1_local_k = lambda1_local_kPlus1;
lambda1_RunningAverageOld = lambda1_RunningAverageNew;
if NumericalOutput
    if mod(nav,NumOutputRate)==0
        disp([' t = ' num2str(t_end,'%13.4f')...
              ', lambda_1 = ' ...
              num2str(lambda1_RunningAverageNew,'%+8.3f')]) )
    end
end
end
lambda1 = lambda1_RunningAverageNew;

```

```
if NumericalOutput
    disp('... end post-transient simulation ...')
    disp(['Final Lambda_1 =' num2str(lambda1,'%+.3f')]) )
end

%-----
function Key_q_Pressed = KeyPressq(src,evnt)
% Test if user presses a key within the active figure
%-----
global KeyPressed_q
KeyPressed_q = (evnt.Character == 'q');
```

Title:

System Identification and Nonlinear Analysis of parameters of a simplified model for flapping flight at low Reynolds numbers.

Introduction:

The study of the unsteady aerodynamics of flapping insect flight is a complex, coupled fluid-structure system. Currently, few models exist that attempt describe the fluid dynamics acting on the flapping wing of an insect. A model of this type can be used to characterize, control, and exploit the flapping wing system for specific performance goals. In most studies, the structure is rigid and its motion prescribed (Sun and Tang 2001), or the fluid dynamics are approximated experimentally (such as Schenato 2003). Schenato's simplified model of a fly's flapping is simple since the work is focused on the overall flight control of a robot fly with rigid plates. Sun and Tang's work is with a two dimensional rigid plate undergoing prescribed kinematics.

The project proposes the exploration of a flexible structure whose dynamics are coupled with the fluid flow. This more closely resembles the natural structure of insect wings. The introduction of flexibility on the wing adds many dimensions of complexity to this problem. As a starting point, this proposed model will be a chord wise cross-section with motion in a plane, Figure 1. This is a model of two rigid bars with a torsion spring at the center pin joint. The motion of top bar is sinusoidally prescribed by similar kinematics to what is common in the literature (See Wang, et al. 2004). This model will then be used in a direct numerical simulation of the unsteady viscous flow at various parameters consistent with the literature in the range of natural flies. This immersed boundary method fluid-structure interaction solver was developed by Marcos Vanella and his advisor Dr. Balaras in 2006 at UMD.

The simulation will be run at a range of stiffness values of the torsion spring. This data will be collected, analyzed, and filtered for the construction of a reduced order state space model of the fluid forces acting on the structural system. To validate and test the system identification, it will be compared with the various outputs and parameters changes. This new analytical model will then be used to characterize, in a dynamical notion, the fluid-structure system. The generalized forces will then be used with the structural model to predict improved values and conditions for flexibility to maximize lift.

This work is in part of a larger, ongoing research project here at UMD. Once the two beam model is understood, then there will be the introduction of flexibility models of increased complexity, such as a nonlinear elastic beam. Ideas on the flexural stiffness of three dimensional insect wings could come from work such as Combes and Daniel 2003. Ultimately the work will be towards a full three dimensional case. This project will lay the foundation in dynamics and control for this continued work.

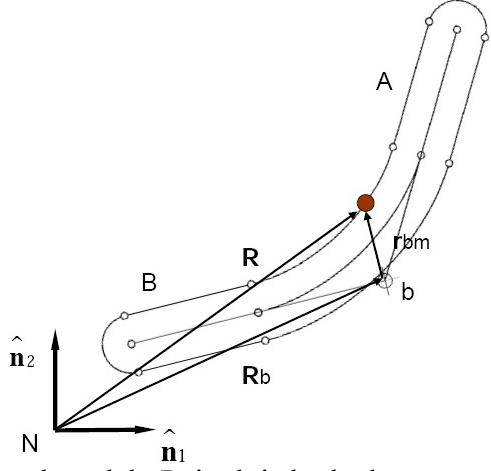


Figure 1: Diagram of structural model. Point b is looked at as a pin joint with a torsion spring, the surface is made smooth for the fluids solver.

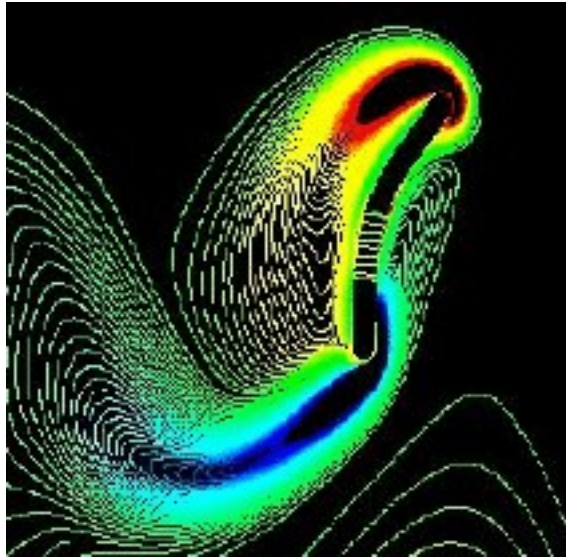


Figure 2: Vorticity field snapshot of the field flexible structure in Vanella2006 fluid solver

Bibliography

Combes, S. A. and Daniel, T. L.. Flexural stiffness in insect wings. *Journal of Experimental Biology* 207, 2979-2987 (2003).

Shenato , L.. Analysis and Control of Flapping Flight: from Biological to Robotic Insects. PhD Thesis. University of California at Berkeley, 2003.

Sun, M. and Tang, J.. Unsteady aerodynamic force generation by a model fruit fly wing in flapping motion. *Journal of Experimental Biology* 205, 55-70 (2002).

Sunada, S. and Ellington, C. P. Approximate Added-Mass Method for Estimating Induced Power for Flapping Flight. *AIAA Journal* 38.8, 1313-1321. August 2000.

Wang, Z. J., Birch, J. M., and Dickinson, M. H.. Unsteady forces and flows in low Reynolds number hovering flight: two-dimensional computations vs robotic wing experiments. *Journal of Experimental Biology* 207, 449-460 (2004).

Nonlinear Model of Aerodynamic Forces of a Planar Two-Link Body in Hovering Flapping at Reynolds Number 75

Timothy Fitzgerald

18-May-2007

Contents

1	Introduction	2
1.1	Background	2
1.2	The Fluid-Structure-Interaction Solver	2
1.3	The Flapping Kinematics	3
1.4	The Need for a Reduced-Order System	5
2	Initial Models	5
2.1	The Equation of Motion	5
2.2	The First Model: Linear State Space Identification	6
2.3	The Second Model: Fourier Series	7
3	The Working Model	8
3.1	Form of the Model	8
3.2	Sensitivity of the Parameters	8
3.3	Stability of the Periodic Attractor	12
4	Sources of Nonlinearity and Reducing the Model	15
4.1	How the reduced-reduced model compared to the DNS Simulations	15
5	Conclusions and Future Directions	19

Abstract

This project focuses on the development and analysis of a reduced order model constructed from a Direct Naiver-Stokes (DNS) Solver for a two-link model undergoing hovering flapping. Due to the complexity of the DNS simulation, solving for one period of flapping takes between two and three days on a current desktop computer. This computational expense gives rise to need of a reduced order model for a simpler numerical study of the system.

The analysis of the purposed nonlinear model includes the predicted stability at a range of stiffness values collected from several DNS simulations. Also the sources of the nonlinearity in the purposed force model are also discussed with views on future work on this problem.

1 Introduction

1.1 Background

To further the understanding of flapping flight of insects, engineering models have been constructed to analyze the parameters in order to exploit flapping as a viable form of mobility for micro aerial vehicles (MAVs). Here at the University of the Maryland, the approach to understanding the dynamics of flapping has focused on simple models. These models started with a rigid bar chord section undergoing flapping flight, then moved into a flexible link. The next step in the series of models is a chain of links, and the ultimate 2-dimensional formulation will be a continuously flexible beam. Dr. Balaras and Marcos Vanella have developed a DNS code to make the 2D simulations. Figure 1 is the mechanical model of the 2 link system.

Further study will be on a 3-dimensional system. Notions of distribution of stiffness will be inspired from [1, 2, 3].

1.2 The Fluid-Structure-Interaction Solver

As state earlier, the fluid solver is using fixed-grid DNS to calculate the velocity and pressure fields surrounding the body. Using an immersed boundary method the solver also couples the free part of the structure with forces. Thus the motion of the structure is coupled to the motion of the fluids. The

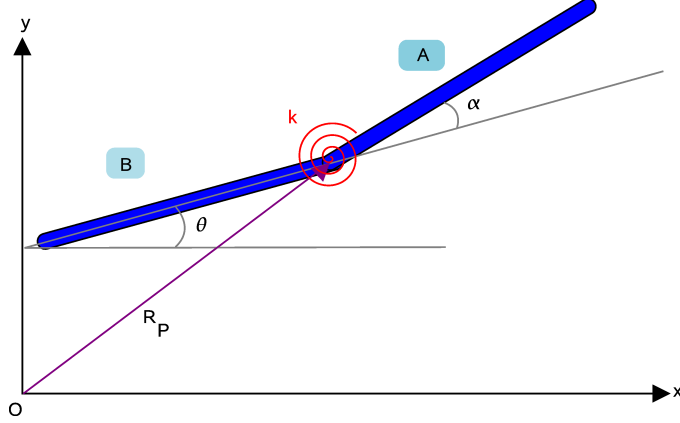


Figure 1: Physical model of the 2 link system

flexible body is defined by the dynamics of the rigid links with a torsion spring attached at the center point.

To simplify the parameter space of: length, width, spring constant, mass, fluid density, fluid speed, and forcing frequency a simple set of ratios can be derived. This leads to three independent parameters ρ/ρ_f (which is the ratio of the density of the beams to the density of the fluid), ω/ω_f (which is the ratio of the natural frequency of the structure over the forcing frequency), and Re (the Reynolds Number). For this study, the region of interest is for a high coupling with the fluid. This means a low Reynolds Number and a relatively light beam mass so that the viscous forces from the fluid are on the same order as the inertial forces on the structure. This region was described by Marcos Vanella in his runs of this code in 2006 as

$$\begin{aligned} Re &= 75 \\ \rho/\rho_f &= 25 \\ 2 \leq \omega/\omega_f &\leq 6 \end{aligned}$$

Figure 2 is an example of a snapshot of the vorticity field during a simulation.

1.3 The Flapping Kinematics

The kinematics of link B are prescribed in a similar manner as Wang [8] prescribes the entire motion of their rigid beam. The additional exponential

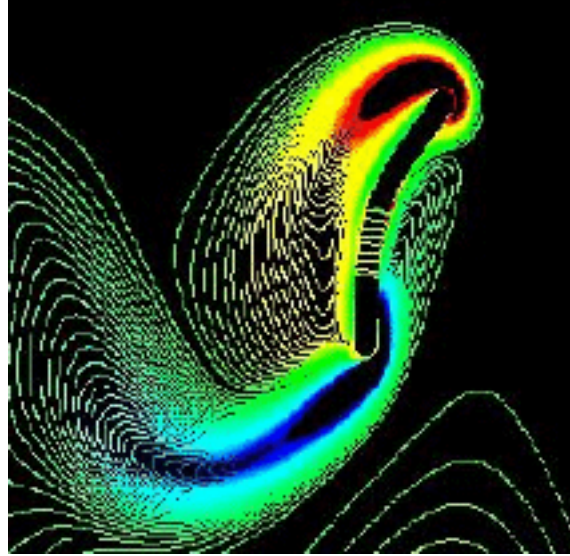


Figure 2: Vorticity, from Marcos Vanella 2006

term provides a damped start, which allows the DNS to begin more smoothly. However at steady state the motion is purely sinusoidal. In our notation:

$$\theta(t) = \theta_0 + (1 - e^{-t/\tau}) A_\theta \sin(2\pi f t + \phi) \quad (1)$$

$$x(t) = (1 - e^{-t/\tau}) \frac{A_x}{2} \sin(2\pi f t) \quad (2)$$

$$y(t) = (1 - e^{-t/\tau}) \frac{A_y}{2} \sin(2\pi f t) \quad (3)$$

$$\tau = 0.8/f \quad (4)$$

Where x and y represent the coordinates in Figure 1 of the pin joint. The values of the coefficients used are also those used by Wang [8] based on Sane's work [7]. These parameters describe level hovering with the degree of freedom in α to be determined by the fluid-structure interaction.

$$\begin{aligned}
f &= \frac{1}{\pi A_x} \\
\theta_0 &= -90^\circ \\
A_\theta &= 45^\circ \\
A_x &= 2.8 \\
A_y &= 0
\end{aligned}$$

1.4 The Need for a Reduced-Order System

The complexity of the DNS code is such that at the Reynolds Number of 75, and a sufficiently sized grid (on the order of 660,000 points) it takes about 2.6 days to compute 1 period of oscillation. Therefore running the simulation until steady state can take weeks. Therefore, it is purposed to explore a system described by a system of ordinary differential equations. This is taking the partial differential equations, and assuming that the aerodynamic loading on the structure can be modeled by a finite-dimensioned function or system of functions.

2 Initial Models

2.1 The Equation of Motion

For the general case of motion in the plane, the equation of motion is found from Figure 1 by using Newton's 2nd Law or Lagrange's Equation.

$$\begin{aligned}
I_A \ddot{\alpha} + k\alpha &= -I_A \ddot{\theta} + m_A \eta_A \sin(\theta + \alpha) \ddot{x} \\
&\quad - m_A \eta_A \cos(\theta + \alpha) \ddot{y} - m_A g \eta_A \cos(\theta + \alpha) + Q_\alpha
\end{aligned}$$

However, the absence of gravity (rotated in the plane) and with level hovering ($y(t) = 0$), then the above equation becomes

$$I_A \ddot{\alpha} + k\alpha = -I_A \ddot{\theta} + m_A \eta_A \sin(\theta + \alpha) \ddot{x} + Q_\alpha \quad (5)$$

This is the form of the equation that was used throughout this project. It is the general force Q_α that is what is attempted to be modeled from data collected from simulations of the DNS. Simulation data has been run and

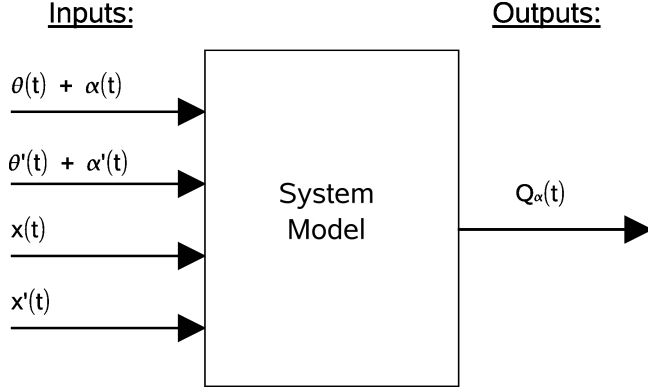


Figure 3: The input/output model of the generalized force Q_α

analyzed for $\omega/\omega_f = (2, 3, 4, 6)$. Using the fluid simulation parameters, the overall length of the body is fixed to 1, the thickness of the beam is chosen to be 1/10, the density of the fluid is fixed to 1. From this, it is possible to calculate the associated parameters (m_A, I_A, k, η_A) that are used in the equation of motion in state form.

The system input/output model of Figure 3 was chosen for its basis on the coupling of the prescribed kinematics with the degree-of-freedom α .

2.2 The First Model: Linear State Space Identification

The first purposed model is that of a multi-input-single-output (MISO) time varying system. One of the simplest representations, and is to both implement and curve is that of a linear time invariant system in state space form.

$$\dot{\vec{q}} = \mathbf{A}\vec{q} + \mathbf{B}\vec{u} \quad (6)$$

$$Q_\alpha = \mathbf{C}\vec{q} + \mathbf{D}\vec{u} \quad (7)$$

Where \vec{q} are the n fictitious states of the forcing Q_α , and the matrices $\mathbf{A}, \mathbf{B}, \mathbf{C}, \mathbf{D}$ are fit using the System Identification Toolbox in Matlab [4]. The easy in integration comes from appending $\dot{\vec{q}}$ to the states of the equation 5.

Various attempts at this method were made, and all of them had the same flaws. In general, the best fit to the data was done with $n = 3$, using the N4SID parameter estimation. The problem was observed when the system

was implemented in equation 5. This linear system would explode, reaching 4-5 orders of magnitude greater values than the output range should be. After a certain period of time, around 3-4 flapping cycles, the force would settle down to the realistic range. This was implemented by turning off the force on α until 4 cycles has passed, therefore keeping the original system from also exploding. When this was done the results were still poor in steady state, and not realistic. Time does not permit a full discussion and figures to illustrate this, but it is believed that the main reason for this was seen in the matrices $\mathbf{A}, \mathbf{B}, \mathbf{C}, \mathbf{D}$ directly upon close inspection.

The problem lies in the base argument, that the system can be approximated by 7 such that it is linearly time dependant and a linear combinations of the input vector u . Noting that the fitted values of A were much less than B , by several orders implies a problem with the approach. This means that the function was dominated by u , but since there are nonlinearities in the true functions, as discussed later, the fit was poor. This brought the need of nonlinear curve fitting, rather than on system identification to light, which brings us to the next evolutionary step.

2.3 The Second Model: Fourier Series

For a short time, there was an exploration of using a Fourier Series to approximate $Q_\alpha(t)$. This function would of the form:

$$Q_\alpha(\alpha + \theta, \dot{\alpha} + \dot{\theta}, x, \dot{x}, t) = \sum_{p=1}^n a_p \cos(p\omega t) + b_p \sin(p\omega t)$$

With coefficients being matched by some curve fitting algorithm to the given inputs. However, this has the shortcoming of being difficult to visualize, and does not really work well in this context. It provides the periodicity needed in the function, but not easily attainted and analyzed nonlinearity. Therefore after some curve fitting and simulations, this approach was also dropped.

Upon discussing this problem with Dr. Balachandran, he suggested a model that is a coupled polynomial with fitter terms. This is what is described in the next section.

3 The Working Model

3.1 Form of the Model

From the previous section the short comings of the other approaches have been discussed. This newer model is based on fitting parameters to the function

$$Q_\alpha(\gamma, \dot{\gamma}, x, \dot{x}) = (\beta_1\gamma + \beta_2\dot{\gamma} + \beta_3x + \beta_4\dot{x}) \quad (8)$$

$$+ (\beta_5\gamma + \beta_6\dot{\gamma} + \beta_7x + \beta_8\dot{x})^2 \quad (9)$$

$$+ (\beta_9\gamma + \beta_{10}\dot{\gamma} + \beta_{11}x + \beta_{12}\dot{x})^3 \quad (10)$$

where $\gamma = \theta + \alpha$ and β_i is the i th free parameter to be fit. The short comings of this equation were not clear at first, but became apparent in further analysis. This form was chosen in an attempt to preserve the cross-coupling terms of nonlinearity, as well as keep the number of fitting parameters small. However there were problem with the sensitivity of the parameter fitting.

3.2 Sensitivity of the Parameters

Since there was a range of $\omega/\omega_f = (2, 3, 4, 6)$ a set of β parameters were fit to each run. Since the function to be fit is nonlinear and the estimation is gradient based, a small change in an initial guess lead to different values of β . Therefore the values of β cannot be determined uniquely in this manner. The next evolution of this model would be purposed to correct this problem. The parameter estimation was done using using the Statistics Toolbox in Matlab [5].

Not all the set of β found gave the same stability information. This is not seen in the DNS simulation data, where all values of ω/ω_f ran provide a stable periodic attractor. Finding a set of initial guesses for each frequency ratio was a challenge. In the end a stable set was found for each DNS simulation data, see Figure 4.

To see how well the nonlinear forcing works, the estimated model and the actual signal from the DNS simulations are plotted in Figure 5. Note the very accurate representation as steady state is achieved, as well as the fair transient behavior at startup. These were estimate using the DNS data for all the inputs and only seeing the comparison on Q_α .

For an example of the simulation of accuracy, against a known value of $\omega/\omega_f = 3$ see Figures 6 and 7.

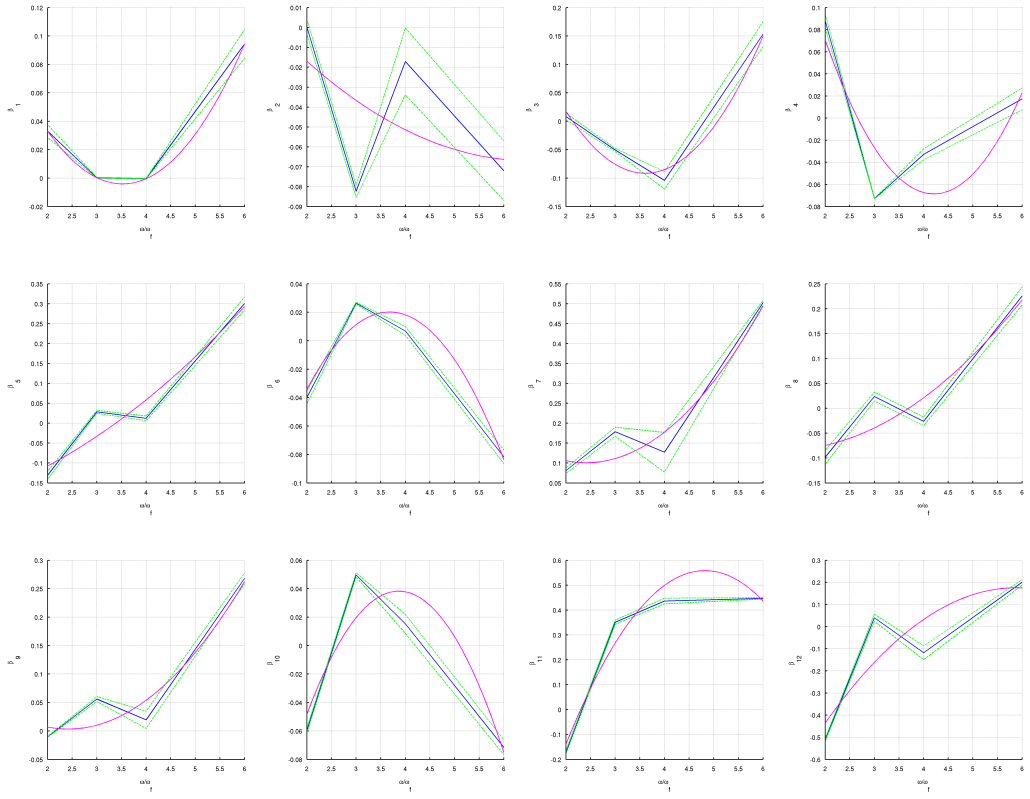


Figure 4: estimated β_i values as a function of ω/ω_f . The blue lines are the linear interpolation between the data points. The green lines are the statistical bounds that the estimation method gave on each β_i . The magenta curve is an attempt at a parabola fit to $\beta_i(\omega/\omega_f)$

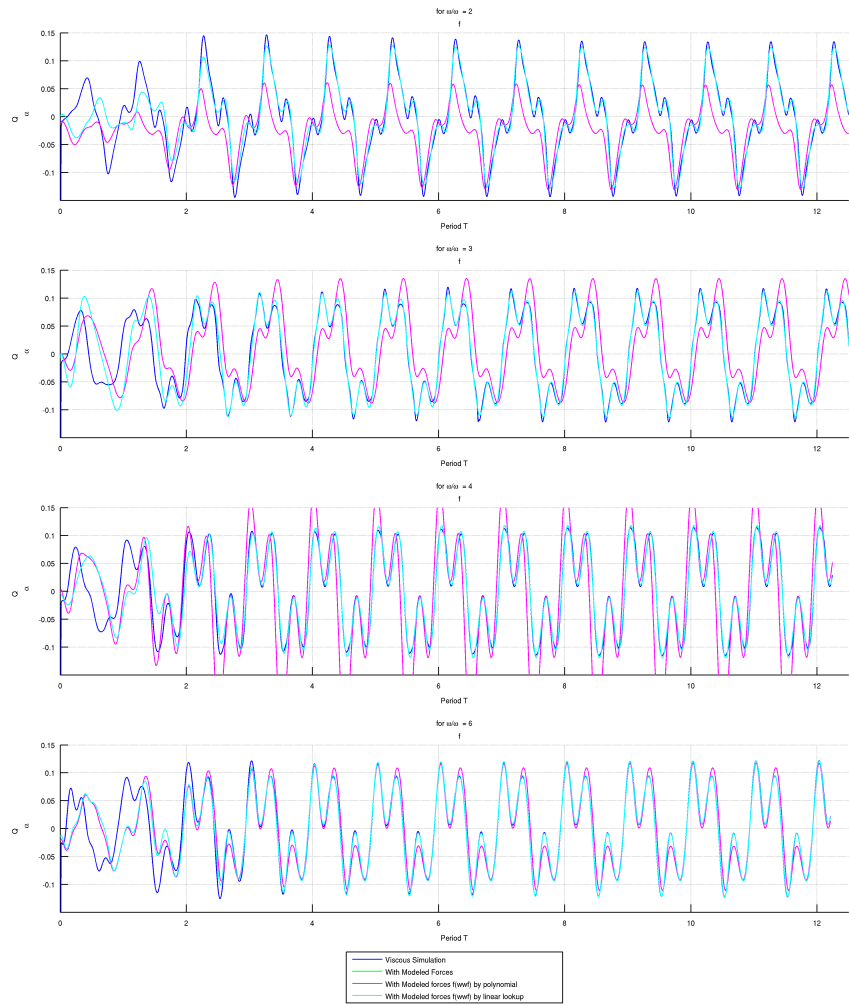


Figure 5: force fits of Q_α with prescribed inputs from the DNS simulation. Note that the green line is completely under the light blue line.

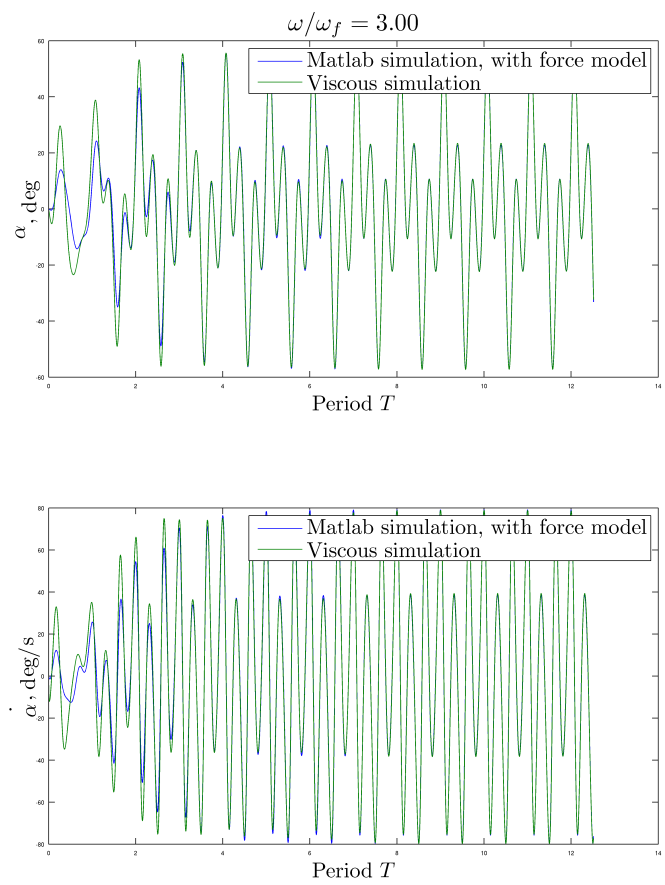


Figure 6: Time History of α and $\dot{\alpha}$

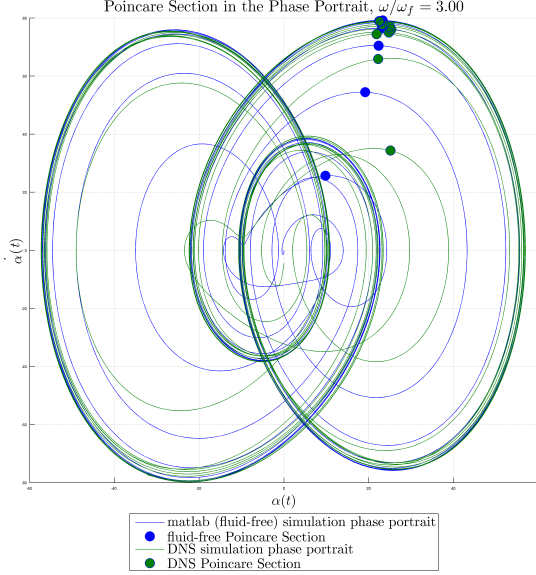


Figure 7: Phase Portrait at $\omega/\omega_f = 3$

As we can see, this implies that for the known value of $\omega/\omega_f = 3$ the ODE model fits the DNS simulation very well. However, due to the time of computation, the simulations of the DNS code at off values of $\omega/\omega_f = (2.5, 5)$ could not be completed to make a comparison. This is left for future work to fine tune the model inbetween known fitted points.

3.3 Stability of the Periodic Attractor

This was done in two ways: a brute force look at the Poincaré section for various initial conditions and the use of constructing the periodic orbit solution. As an example of the brute force method, Figure 8 shows how all the initial conditions over a very large starting range converge to a single point in the Poincaré section.

Through the use of the Shooting Method, as described in [6, Section 6.5.2], for a non-autonomous system the Floquet parameters were calculated

Poincare Section for system with forcing model, for various initial conditions

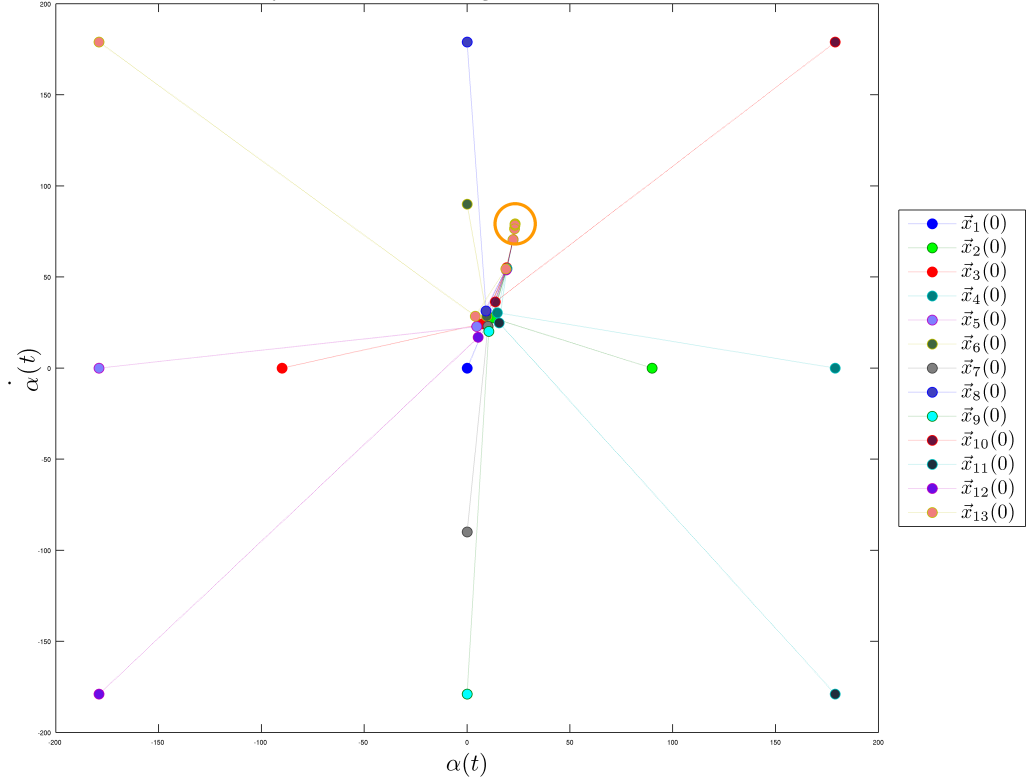


Figure 8: Poincare Section at Various Starting points traced to the stable periodic attractor $\omega/\omega_f = 3$

across the range of ω/ω_f . The Periodic Solution to the system is of the form

$$\mathbf{x}(t_0) = \eta \quad (11)$$

$$\mathbf{x}(t_0 + T, \eta) = \eta \quad (12)$$

$$t_0 \geq 0 \quad (13)$$

$$T = \frac{2\pi}{f} \quad (14)$$

by means of calculating a correction to an initial guess on the vector η by calculating $n + 1$ initial guesses, each perturbed by a small quantity δ in the k th element such that

$$\begin{aligned} \mathbf{x}(t_0) &= \eta_0 \\ \mathbf{x}^k(t_0) &= \eta_0 + \delta \mathbf{e}_k \end{aligned}$$

where e_k is the k th column of the identity matrix. Then calculating each column of

$$\frac{\partial \mathbf{x}}{\partial \eta_k}(T, \eta_0) = \frac{\mathbf{x}^k(T + t_0, \eta_0 + \delta \mathbf{e}_k) - \mathbf{x}(T + t_0, \eta_0)}{\delta} \quad (15)$$

And from the orthogonality condition, solving the equation

$$\delta \eta = \left[\frac{\partial \mathbf{x}}{\partial \eta}(T + t_0, \eta_0) - \mathbf{I} \right]^{-1} (\eta_0 - \mathbf{x}(T + t_0, \eta_0)) \quad (16)$$

gives the needed correction to make the starting place for next iteration of the solution. Once the solution has converged to below a small tolerance, $|\delta \eta| < \epsilon$, then the matrix

$$\Phi = \frac{\partial \mathbf{x}}{\partial \eta}(T + t_0, \eta) \quad (17)$$

is equal to the monodromy matrix. Then, calculating the eigenvalues of this matrix gives Floquest parameters. The solution is a stable periodic attractor if all Floquet parameters for that orbit are inside the unit circle of the complex plane. Figure 9 demonstrates the results of this sequential continuation of this stable periodic attractor. The value of ω/ω_f is calculated by a linear interpolation for each β_i between the two nearest known fitted

values of β_i . This is not necessarily representative of solution at unknown points, however it is a conjecture that will be tested in the future when more data is available. This shows that for this set of β parameters the system has a stable periodic attractor for all the known corresponding data points of the DNS simulation.

4 Sources of Nonlinearity and Reducing the Model

Due to the time constraints on this project a complete and lengthy discussion of the this topic is not possible. As a starting point to find the sources of nonlinearity and the relative contributions to the overall solution, equation 10 is expanded and calculated for the various values of β_i . Then the maximum value of each column is calculated. Then the value of each element is checked against this maximum, and if it is greater than 20 it remains, else it is zeroed. This constructs the reduced values of each nonlinear parameters, see Table 1.

From here it is clear how a large group of nonlinear terms, especially in the quadratic section of the expansion, account for only a small part of the solution. There this new reduced model is tested to see if it still accurately produces the same stability information as full system.

4.1 How the reduced-reduced model compared to the DNS Simulations

Using the parameters from Table 1, then run a simplified set of points to construct a periodic solution as in previous section. The results can be seen in Figure 10. It is clear that when the threshold is set at %20 that the lowest value of ($\omega/\omega_f = 2$) is predicted incorrectly, and the stability of ($\omega/\omega_f = 4$) has become critical. The other points are still reasonable close.

This gives some insight into how, and from what source, the nonlinearity of the force Q_α varies across different operating regions of ω/ω_f . This is probably due to $\omega/\omega_f = 2$ influence on the fluid, and the creation of different vortex structures in the wake.

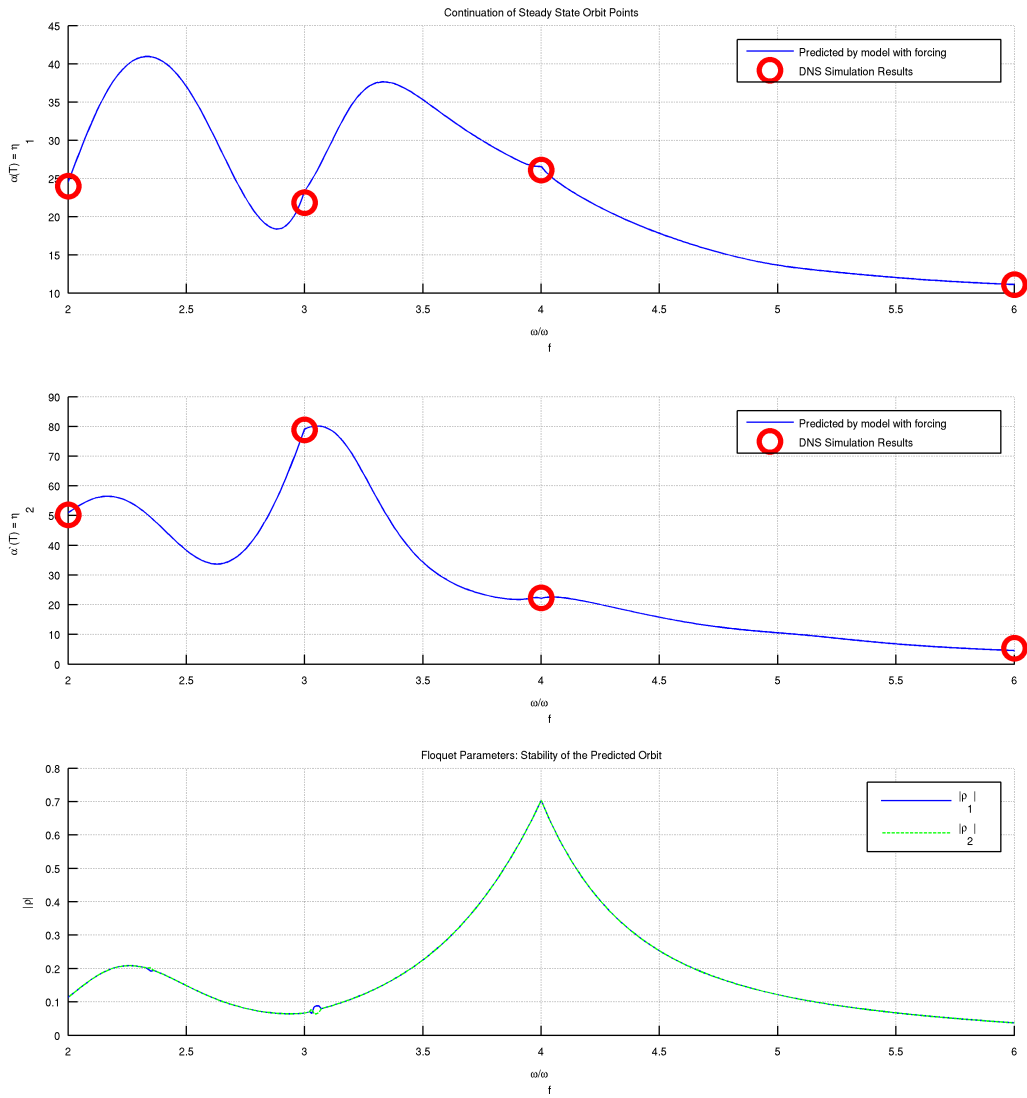


Figure 9: Predicted Continuation and Stability of Periodic Solutions over a range of ω/ω_f

Table 1: Numerical Values of the Expanded form of Q_α with values set to zero if less than %20 maximum

i	Terms	Coeffs	$\omega/\omega_f = 2$	$\omega/\omega_f = 3$	$\omega/\omega_f = 4$	$\omega/\omega_f = 6$
1	γ	β_1	0.0331	0	0	0.0943
2	$\dot{\gamma}$	β_2	0	-0.0824	0	-0.0720
3	\dot{x}	β_4	0.0879	-0.0729	-0.0328	0
4	x	β_3	0	-0.0505	-0.1040	0.1532
5	γ^2	β_5^2	0	0	0	0.0904
6	$\gamma\dot{\gamma}$	$2\beta_5\beta_6$	0	0	0	0
7	$\dot{\gamma}^2$	β_6^2	0	0	0	0
8	$\gamma\dot{x}$	$2\beta_5\beta_8$	0	0	0	0.1356
9	$\dot{\gamma}\dot{x}$	$2\beta_6\beta_8$	0	0	0	0
10	\dot{x}^2	β_8^2	0	0	0	0
11	γx	$2\beta_5\beta_7$	0	0	0	0.3023
12	$\dot{\gamma}x$	$2\beta_6\beta_7$	0	0	0	-0.0821
13	$x\dot{x}$	$2\beta_7\beta_8$	0	0	0	0.2266
14	x^2	β_7^2	0	0.0319	0	0.2526
15	γ^3	β_9^3	0	0	0	0
16	$\gamma^2\dot{\gamma}$	$3\beta_{10}\beta_9^2$	0	0	0	0
17	$\gamma\dot{\gamma}^2$	$3\beta_{10}^2\beta_9$	0	0	0	0
18	$\dot{\gamma}^3$	β_{10}^3	0	0	0	0
19	$\gamma^2\dot{x}$	$3\beta_{12}\beta_9^2$	0	0	0	0
20	$\gamma\dot{\gamma}\dot{x}$	$6\beta_{10}\beta_{12}\beta_9$	0	0	0	0
21	$\dot{\gamma}^2\dot{x}$	$3\beta_{10}^2\beta_{12}$	0	0	0	0
22	$\gamma\dot{x}^2$	$3\beta_{12}^2\beta_9$	0	0	0	0
23	$\dot{\gamma}\dot{x}^2$	$3\beta_{10}\beta_{12}^2$	-0.0468	0	0	0
24	\dot{x}^3	β_{12}^3	-0.1336	0	0	0
25	γ^2x	$3\beta_{11}\beta_9^2$	0	0	0	0.0963
26	$\gamma\dot{\gamma}x$	$6\beta_{10}\beta_{11}\beta_9$	0	0	0	0
27	$\dot{\gamma}^2x$	$3\beta_{10}^2\beta_{11}$	0	0	0	0
28	$\gamma\dot{x}x$	$6\beta_{11}\beta_{12}\beta_9$	0	0	0	0.1439
29	$\dot{\gamma}\dot{x}x$	$6\beta_{10}\beta_{11}\beta_{12}$	-0.0314	0	0	0
30	\dot{x}^2x	$3\beta_{11}\beta_{12}^2$	-0.1342	0	0	0
31	γx^2	$3\beta_{11}^2\beta_9$	0	0.0207	0	0.1606
32	$\dot{\gamma}x^2$	$3\beta_{10}\beta_{11}^2$	0	0.0184	0	0
33	$\dot{x}x^2$	$3\beta_{11}^2\beta_{12}$	-0.0449	0	-0.0676	0.1200
34	x^3	β_{11}^3	0	0.0433	0.0830	0.0893

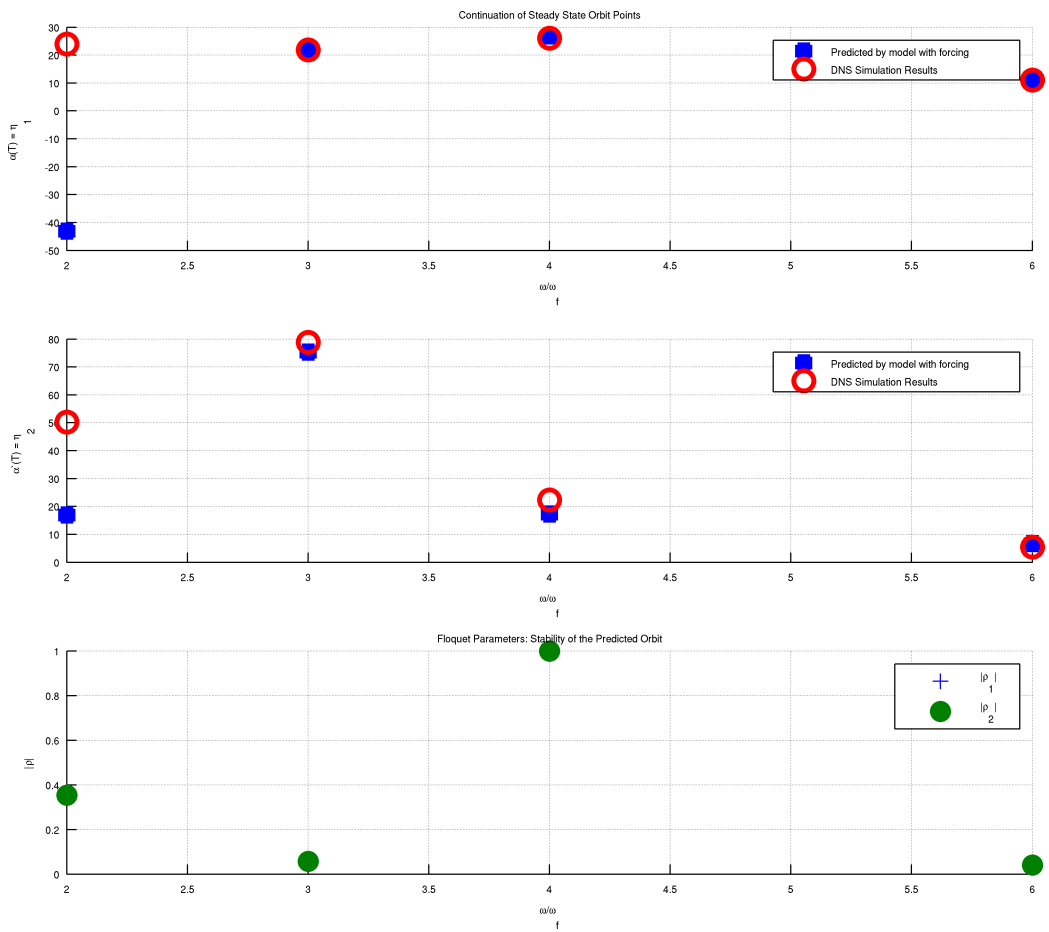


Figure 10: Predicted Continuation and Stability of Periodic Solutions over a range of ω/ω_f for the reduced model with many zero entries

5 Conclusions and Future Directions

In all, the project did give insight into possible causes for nonlinearities in the fluid force acting on the structural model. The estimated working model also gave very good results when implemented into the equation of motion across all the ranges of $\omega/\omega_f = (2, 3, 4, 6)$. Since the comparsion data has not yet been completed, then a true comparison to see if the model works for inbetween values of ω/ω_f , say at 2.5 or 5.

Further study can also include a revamped model for Q_α taking into account the information gathered from Section 4 on the sources of nonlinearity. Also, further study in optimization will give a deeper insight in the actual parameter estimation procedure. Perhaps a global minimum for the curve fit can be achieved using more advanced procedures.

References

- [1] S. A. Combes and T. L. Daniel. Flexural stiffness in insect wings i. scaling and the influence of wing venation. *Journal of Experimental Biology*, 206:2979–2987, 2003. Authors from the Department of Biology, University of Washington, Seattle.
- [2] S. A. Combes and T. L. Daniel. Flexural stiffness in insect wings ii. spatial distribution and dynamic wing bending. *Journal of Experimental Biology*, 206:2989–2997, 2003. Authors from the Department of Biology, University of Washington, Seattle.
- [3] S. A. Combes and T. L. Daniel. Into thin air: contributions of aerodynamic and inertial-elastic forces to wing bending in the hawkmoth *manduca sexta*. *Journal of Experimental Biology*, 206:2999–3006, 2003.
- [4] Lennart Ljung. *System Identification Toolbox User’s Guide*. The Mathworks, 7th edition, March 2007.
- [5] The Mathworks. *Statistics Toolbox 6 User’s Guide*, March 2007.
- [6] Ali H. Nayfeh and Balakumar Balachandran. *Applied Nonlinear Dynamics*. Wiley, 1995.

- [7] Sanjay P. Sane and Michael H. Dickinson. The control of flight force by a flapping wing: Lift and drag production. *Journal of Experimental Biology*, 204:2607–2626, May 2001.
- [8] Z. Jane Wang, James M. Birch, and Michael H. Dickinson. Unsteady forces and flows in low reynolds number hovering flight: two-dimensional computations vs robotic wing experiments. *Journal of Experimental Biology*, 207:449–460, 2004.

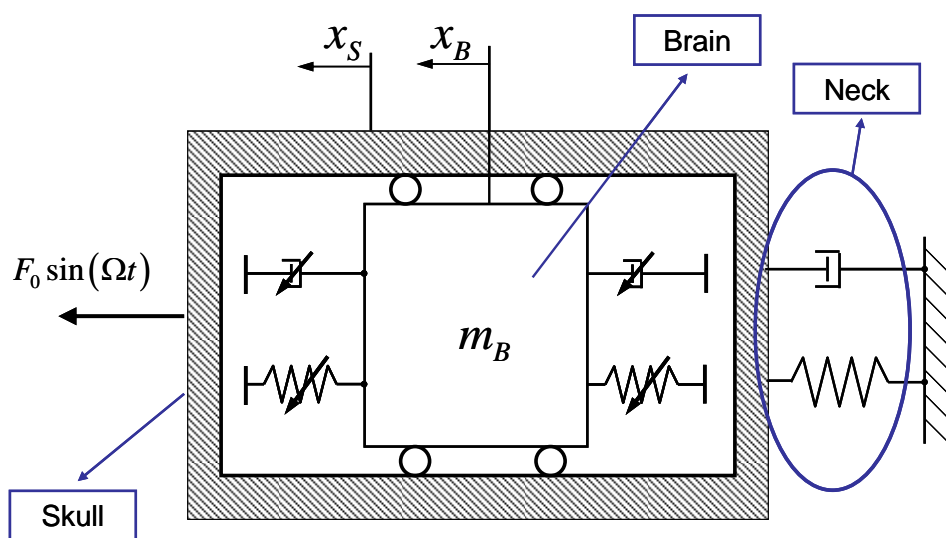
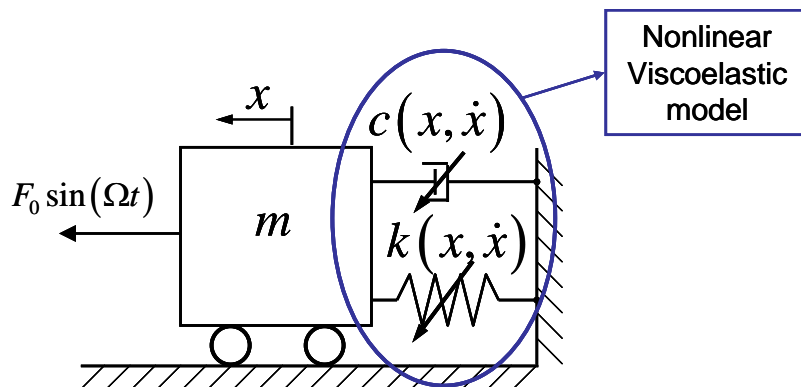
Analysis of Nonlinear Viscoelastic Constitutive Properties for Brain Tissue for Dynamic Simulations

The study of brain injury caused by direct or indirect (due to accelerations) impacts to the head has attracted attention since the last four decades. Recently, brain injury caused by strong blasts originated from explosions or other sources have gained attention among the researching community. In studying brain injury several complexities need to be surpassed, such as those related to geometry of the problem and definition of material properties. Geometrical complexities of the head and tissues pose limitations for analytical treatments of problem. Therefore, the trend nowadays is the using of finite element models (FEM) that allow dealing with more complicated and detailed geometries. In addition, these models enable studying stress and strain distributions inside the head, developed as a consequence of an impact or a blast. Accurate data of the head geometry may be obtained from sources such as magnetic resonance imaging (MRI). Although the geometric complexities may be accounted for with this methodology, simplified material constitutive models were commonly used for the different parts. Linear elastic properties are generally assumed for the bones (skull) and internal membranes (falx cerebelli, dura, tertorium, etc), and sometimes for the brain tissue. However, some models include linear viscoelastic properties for the brain and other few deal with nonlinear viscoelastic constitutive laws.

Several *in vitro* experimental works with rat and pig brain tissues (e.g., Miller and Chinezi, 2002), have suggested that the mechanical response of brain tissue need to be characterized as nonlinear viscoelastic solid with different behavior to compression and tension.

It is the goal of this work to explore different tissue nonlinear viscoelastic constitutive laws proposed in the literature. Particularly the models proposed by Miller and Chinezi (2002) and Shen *et al* (2006), as well as some standard models for non-linear hyperelasticity (Odgen, Mooney-Rivlin for incompressible materials) will be analyzed in order to construct simplified, lumped mass-spring-dashpot models (Figure 1). These simplified models allow characterizing analytically the response of brain tissue under dynamic loading and transient inputs. The influence of the different parameters (material constants) that characterizes the nonlinear behavior of the material is investigated in looking for possible bifurcations. Once understanding of these basic models has been gained, more complex models are proposed to study head+brain dynamic response.

This work constitutes a part of a successive approach towards incorporating non-linear viscoelastic models of brain tissue in finite element models to study the system head+brain and gain better understanding of the stress-strain distribution developed under impact or blast loads.



References:

- Miller K., Chinezi K, 2002. Mechanical properties of brain tissue in tension. *Journal of Biomechanics* **35**, 483-490.
- Miller K., Chinezi K, Orssengo G., Bednarz P., 2000. Mechanical properties of brain tissue in-vivo: experiment and computer simulation. *Journal of Biomechanics* **33**, 1369-1376.
- Darvish K. K., Crandall J.R. Nonlinear viscoelastic effects in oscillatory shear deformation of brain tissue. *Medical Eng. & Physic* **23**, 633-645.
- Shen F., Tay T.E., Li J.Z., Nigen S., Lee P.V.S, Chan H.K., 2006. Modified Bilston nonlinear viscoelastic Model for finite element head injury studies. *Journal of Biomech. Eng* **128**, 797-801.
- Nayfeh A. and, Mook D. T., 1995. *Nonlinear Oscillations*. Wiley.
- Nayfeh A. and Balachandran B., 1995. *Applied Nonlinear Dynamics: Analyticl, Computational, and Experimental Methods*. Wiley

Dynamic Analysis and Parameter Study on Biped Robot with Torso by Simple Controller

ENME 665 Project
Student: YenChen Liu

May 12, 2009

Contents

1	Introduction	2
1.1	Background	2
1.2	Motivation	2
2	System Model	5
2.1	Robot Model	5
2.2	Controller and Mechanical Energy	7
2.3	Simulation Model	7
3	Gait Motion and Stable Orbit	11
3.1	Steady Gait	11
3.2	Motion of Torso	11
3.3	Definition of Characteristics	12
3.4	Stability of Poincaré Map	13
4	Parameter Study	14
4.1	Effect of Slope Angle with $\theta_3^d = -\psi$	14
4.2	Effect of Desired Torso Angle	14
4.3	Effect of Slope Angle with $\theta_3^d = \psi$	16
4.4	Effect of Slope Angle with $\theta_3^d = -0.291$ rad	19
4.5	Effect of Torso Length	19
4.6	Period-doubling Bifurcation	22
5	Conclusions and Further Works	24

Chapter 1

Introduction

1.1 Background

Biped robots and other legged robots are superior to wheel robots because the former are potentially suited to hazardous environments, exploration of unstructured terrain, moving on unpaved terrains, and ascending and descending the stairs. However, the most important issue that obstructs the application of walking robot is the lack of energy efficiency. Therefore, the developments of passive or semi-passive bipedal locomotion attract many researchers' attentions and interests in order to accomplish an efficient walking robot.

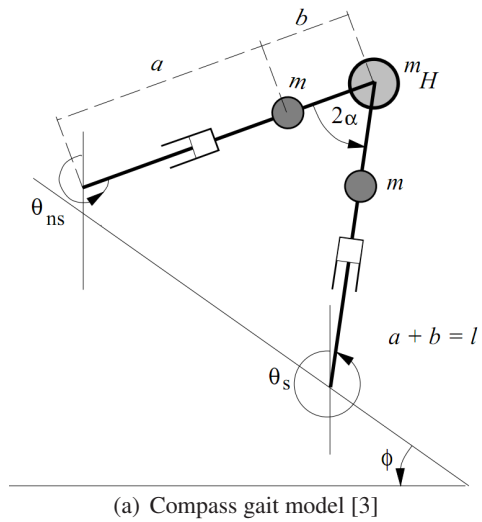
Passive walking provides two interesting features, which are inherent stability and low energy consumption [11]. The passive biped models can resist small disturbances for certain parameter values without control. In addition, the energy consumption of passive biped robot is much lower than the conventional bipedal robot because they are driven from the conversion of the robot's gravitational potential energy as it walks down the slope.

Different passive-based compass-like biped models, shown in Figure 1.1, have been used to investigate the phenomena of passive walking, such as the straight legged model [3], the kneed model [1], the torso model [5], and the 3D model. The motion of biped robot that has been proved is a limit cycle, whose stability can be decided by calculating the Jacobian matrix of Poincaré map of the limit cycle. The behavior of straight legged model, which is the simplest compass-like biped model, was studied in [3]. The researchers showed that three parameters, the ground slope, the normalized mass, and the length of robot, affect the robot gait in the same qualitative manner. They also demonstrated the existence of bifurcation and chaotic gait. Recently, the research in [13] studied the comparison of gaits for straight legged model and kneed model. However, these models can not be used for walking uphill without any control input. Seeing that, the researches in [2, 10] proposed passivity-based control law to assist the robot walking uphill.

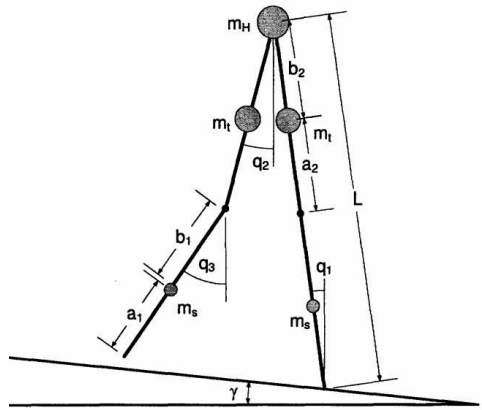
1.2 Motivation

The conventional passive biped robot can only walk in a declined slope with a certain walking period, velocity and step length. These values are mainly determined by the slope angle. In order to extend the applied area of biped robot, researches with limited control on a passivity-based biped robot are required. If a biped robot can take the advantage of inherent stability and low energy consumption in addition to a simple control to enhance the working range and performance, it definitely can be applied to different kind of needs, such as robotic engineering, biomedical engineering, etc.

For example, there are many research institutes around the world doing the research on walking or humanoid robot. However, for the sake of walking on different slope of ground,



(a) Compass gait model [3]



(b) Biped robot with knee [1]

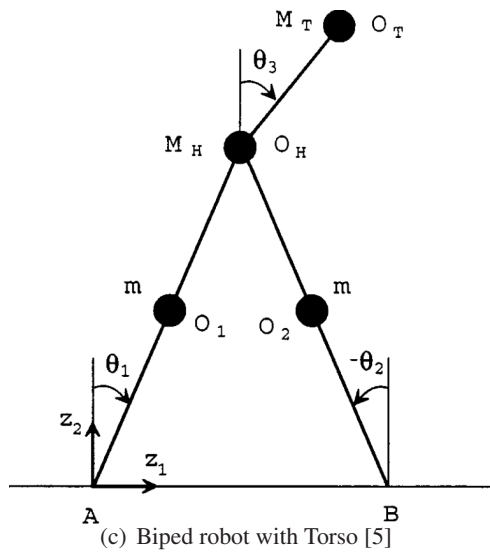


Figure 1.1: Different Kinds of Biped Model.

walking in different speed or ascending and descending the stairs, the weight and power consumption of these robots are comparatively higher. If the research on passivity-based biped robot is accomplished, the biped robot can meet the diverse demands of lower weight and energy consumption. Moreover, handicapped patients mostly use wheelchairs to assist their movements from one place to another. Yet, wheelchairs can only work on flat ground, so that the patients have difficulties in moving to the direction they want. In addition, patients using wheelchairs are sitting instead of standing, they usually have self-confident problem in their social life. If possible, the passivity-based biped robot can be utilized in the future to develop a walking assisted device, which can be controlled by only the user's torso position.

In this project, the nonlinear behavior of passive biped robot with torso by simple PD control is studied. The stability of passive gait and limit cycle is discussed based on orbital stability or Poincaré stability and the contraction of phase flow. Moreover, the effects of continuous change of the parameters on the gait of the biped robot with torso is studied in order to find out whether the bifurcation of the system will cause when one of the parameters exceeds a certain value. The parameters considered will be slope angle, torso angle and length of torso. The objective of this project is to find out the relation between torso and gait characteristics.

This report is organized as follows. The considered robot model of biped robot with torso as well as simulation model were mentioned in Chapter 2. Then the motion of steady gait and torso, stable orbit, and stability of Poincaré map were discussed in Chapter 3. The results of parameter study were finally summarized in Chapter 4.

Chapter 2

System Model

2.1 Robot Model

The dynamic model of a simple planar biped robot with torso is shown in Figure 2.1. The robot consists of two straight legs and a torso, with no ankles and no knees. The model has five degree-of-freedom if there is no foot contact with the ground. During the swing stage of the motion, the stance leg is acting as a pivot. Thus the biped robot has only three degree-of-freedom.

The governing equation of the robot consists of nonlinear differential equations for the swing stage and algebraic equations for the transition, which is the impact between the foot and ground. The dynamic model of the robot between two sequential impacts is referred to [5]. The Lagrange dynamics is

$$M(q)\ddot{q} + C(q, \dot{q})\dot{q} + G(q) = Bu \quad (2.1)$$

where $q = [\theta_1 \ \theta_2 \ \theta_3]^T$, and $u = [u_1 \ u_2]^T$. The details of the matrices are

$$M(q) = \begin{bmatrix} M_{11} & M_{12} & M_{13} \\ M_{21} & M_{22} & 0 \\ M_{31} & 0 & M_{33} \end{bmatrix} \quad (2.2)$$

$$M_{11} = \left(\frac{5}{4}m_l + m_h + m_t\right)l^2, \quad M_{12} = -\frac{1}{2}m_ll^2\cos(\theta_1 - \theta_2)$$

$$M_{13} = m_t l \cos(\theta_1 - \theta_3)l_t, \quad M_{21} = M_{12}, \quad M_{22} = \frac{1}{4}m_t l^2$$

$$M_{31} = M_{13}, \quad M_{33} = m_t l_t^2$$

$$C(q, \dot{q}) = \begin{bmatrix} 0 & C_{12} & C_{13} \\ C_{21} & 0 & 0 \\ C_{31} & 0 & 0 \end{bmatrix} \quad (2.3)$$

$$C_{12} = -\frac{1}{2}m_l^2 \sin(\theta_1 - \theta_2)\dot{\theta}_2, \quad C_{13} = m_t l \sin(\theta_1 - \theta_3)l_t \dot{\theta}_3$$

$$C_{21} = \frac{1}{2}m_l^2 \sin(\theta_1 - \theta_2)\dot{\theta}_1, \quad C_{31} = -m_t l \sin(\theta_1 - \theta_3)l_t \dot{\theta}_1$$

$$G(q) = \begin{bmatrix} -\frac{1}{2}g(2m_h + 3m_l + 2m_t)l \sin(\theta_1) \\ \frac{1}{2}g m_t l \sin(\theta_2) \\ -g m_t l \sin(\theta_3) \end{bmatrix} \quad (2.4)$$

$$B = \begin{bmatrix} -1 & 0 \\ 0 & -1 \\ 1 & 1 \end{bmatrix} \quad (2.5)$$

On the dynamic equation of swing stage, the θ_1 is the angle of stance leg, which is contact with ground, θ_2 is the angle of swing leg, and θ_3 is the angle of torso. The input u_1 is a torque applied between the torso and the stance leg, and u_2 is a torque applied between the torso and the swing leg. The mass of legs, hip, and torso are lumped and denoted by m_l , m_h , and m_t , respectively. The length of legs, and torso are denoted by l , and l_t .

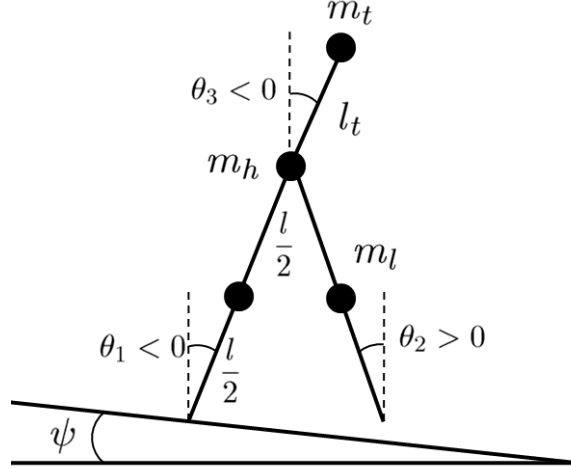


Figure 2.1: A typical limit cycle for the compass-like biped.

For a steady walking, swing leg and stance leg switches sequentially. A swing leg will switch to stance leg after it contact the ground, and vice versa. During the contact between the swing leg and the ground, the impact model can be derived based on the conservation law of angular momentum. The impact is assumed to be inelastic and without slipping. During the impact stage, the configuration remains unchanged. The pre-impact and the post-impact configurations of the robot can be simply related by

$$q^+ = \begin{bmatrix} 0 & 1 & 0 \\ 1 & 0 & 0 \\ 0 & 0 & 1 \end{bmatrix} q^- \quad (2.6)$$

The superscripts “-” and “+” respectively denote pre-impact and post-impact. The equation means during the impact, the leg of swing and stance is changed and the torso keeps unchanged. As for the angular velocity between pre-impact and post-impact, it can be computed from

$$Q^+(q^+) \dot{q}^+ = Q^-(q^-) \dot{q}^- \quad (2.7)$$

Then the angular velocity after impact can be obtained

$$\dot{q}^+ = (Q^+(q^+))^{-1} Q^-(q^-) \dot{q}^- = P(q) \dot{q}^- \quad (2.8)$$

where

$$P(q) = \frac{1}{P_d l_t} \begin{bmatrix} P_{11} & P_{12} & P_{13} \\ P_{21} & P_{22} & P_{23} \\ P_{31} & P_{32} & P_{33} \end{bmatrix} \quad (2.9)$$

$$P_d = -3m_l + 2m_l \cos(2\theta_1^- - 2\theta_2^-) - 4m_h - 2m_t + 2m_t \cos(2\theta_2^- - 2\theta_3^-)$$

$$P_{11} = (-2m_l - 4m_h - 2m_t) \cos(\theta_1^- - \theta_2^-) + 2m_t \cos(\theta_1^- + \theta_2^- - 2\theta_3^-)$$

$$P_{12} = m_l, \quad P_{22} = 2m_l \cos(\theta_1^- - \theta_2^-), \quad P_{32} = -m_l l \cos(\theta_2^- - \theta_3^-)$$

$$P_{21} = m_l - (4m_l + 4m_h + 2m_t) \cos(2\theta_2^- - 2\theta_2^-) + 2m_t \cos(2\theta_1^- - 2\theta_3^-)$$

$$P_{31} = (-m_l - m_h - m_t)2l\cos(\theta_1^- - \theta_3^-) + (m_l + m_h + m_t)2l\cos(\theta_1^- - 2\theta_2^- + \theta_3^-) \\ + m_l l \cos(3\theta_1^- - 2\theta_2^- - \theta_3^-)$$

In addition to the assumptions that the impact is inelastic and without slipping, here also assumes that the lower leg is clear to the ground until the desired moment of contact. The idea of using prismatic-joint knee in [3] is adopted here. Then the impacts occur when the tip of the swing leg contacts the walking surface. Let H be the height from the tip of swing leg to the ground, which is defined by

$$H(q^-) = l(\cos(\theta_1 + \psi) - \cos(\theta_2 + \psi)) \quad (2.10)$$

where ψ is the angle of slope. The impact occurs in the set S , which is defined by

$$S = \{(q, \dot{q}) | H(q^-) = 0, \frac{dH(q^-)}{dt} < 0, \text{and } \dot{\theta}_1 < 0, \dot{\theta}_2 < 0\} \quad (2.11)$$

2.2 Controller and Mechanical Energy

Biped robot with torso can not provide passive walking, because the control torque of torso is needed. There are many controllers can be used for controlling torso on biped robot [6, 8, 9]. In this project, the simple PD controller is used on the torque applied between the torso and stance leg, which is u_1 and defined by

$$u_1 = -k_p(\theta_3 - \theta_3^d) - k_d\dot{\theta}_3 \quad (2.12)$$

where θ_3^d is the desired torso angle, which is a constant, k_p and k_d are the control gains. If choose the desired torso angle $\theta_3^d = -\psi$, where ψ is the slope angle, the torso would be held on vertical to the slope when the biped robot walking on the slope with $\psi > 0$.

For a biped robot without torso, the total mechanical energy keep constant between two impacts, which means the sum of potential energy and kinetic energy conserve during the swing stage. However, on the biped robot with torso, the sum of these two energy doesn't conserve anymore, because the controller for torso is needed. On the other hand, the sum of potential energy, kinetic energy, and controller energy will be constant during swing stage. These energy are computed by the equations below.

$$P = m_h g l \cos(\theta_1) + m_l g \frac{l}{2} \cos(\theta_1) + m_l g \left(l \cos(\theta_1) - \frac{l}{2} \cos(\theta_2) \right) \\ + m_t g (l \cos(\theta_1) + l_t \cos(\theta_3)) + P_0 \quad (2.13)$$

$$K = \frac{1}{2} \dot{q}^T M(q) \dot{q}, \quad E_t = \int \dot{q}^T B u \quad (2.14)$$

where P is the potential energy, K is kinetic energy, and E_t is the energy applied to the torso. The total mechanical energy $E = P + K + E_t$ will keep constant during the swing stage.

2.3 Simulation Model

Although the biped robot has a simple kinematics, the hybrid nature of the governing equations make it impossible to utilize the traditional tools to aid the study of strongly nonlinear systems. There are several approaches can be utilized to handle problems in the situation. Numerical simulation, which is the most generally used tool for planar biped robot, will be adopted in this project. The full nonlinear equations of the robot is preserved. The model of simulation for the analysis and study below are built on Simulink.

The first simulation conducted here is referred to [6]. The value of parameters for the original simulation are

$$m_l = 5kg , \quad m_h = 10kg , \quad m_t = 10kg$$

$$l = 1m , \quad l_t = 0.5m , \quad g = 9.8m/s$$

$$\psi = 0.052rad , \quad \theta_3^d = -0.052rad , \quad k_p = 700 , \quad k_d = 200$$

And the limit cycle can be found on the initial conditions

$$q = \{0.2429, -0.3741, -0.0537\} , \quad \dot{q} = \{-1.0104, 0.0106, -0.0764\}$$

The simulation results for this simulation are shown from Figure 2.2 to Figure 2.3.

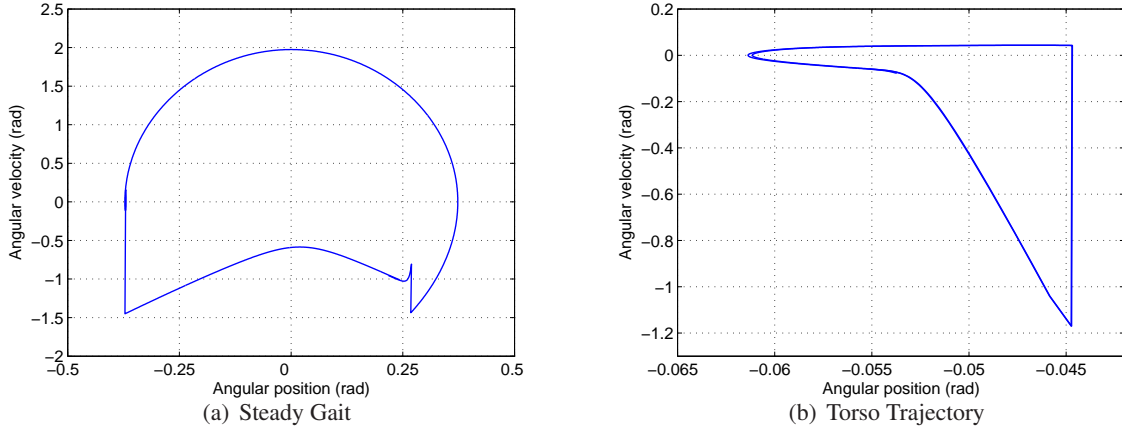


Figure 2.2: Steady Trajectory when $\psi = 0.052rad$, $\theta_3^d = -0.052rad$, $k_p = 700$ and $k_d = 200$.

Figure 2.2, (a) is the steady gait trajectory, which is similar to biped robot without torso [2, 10], and (b) is the trajectory of torso, which can be referred to [6]. The detailed motion of gait and torso will be discussed in next chapter.

Figure 2.3 shows the angular position of two legs, blue and green lines, and torso, red line. The dash-dot lines represent the occurrence of impact. In this Figure, from 0sec to 0.762sec, the green line is swing leg, and blue line is stance leg. After the first impact, the green line switches from swing leg to stance leg and blue line switches to swing leg. The angular position of torso will sway between the value -0.052 rad.

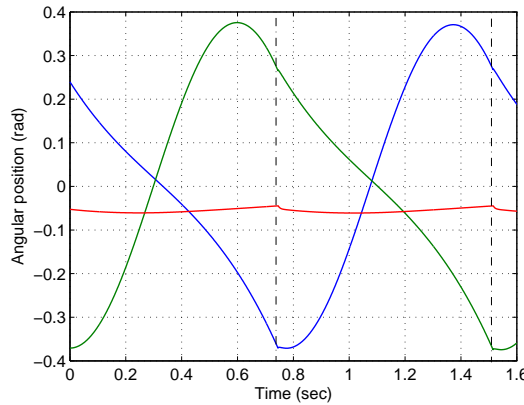
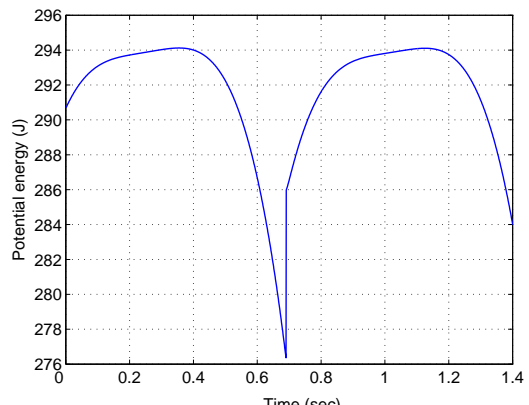
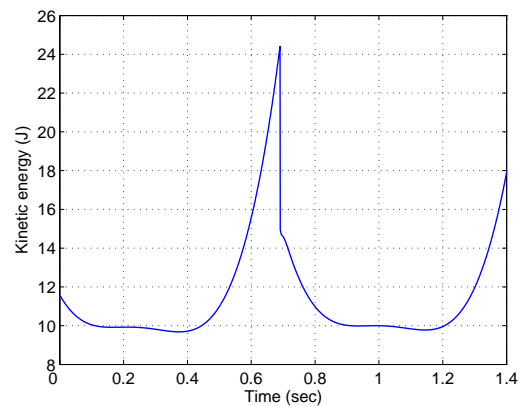


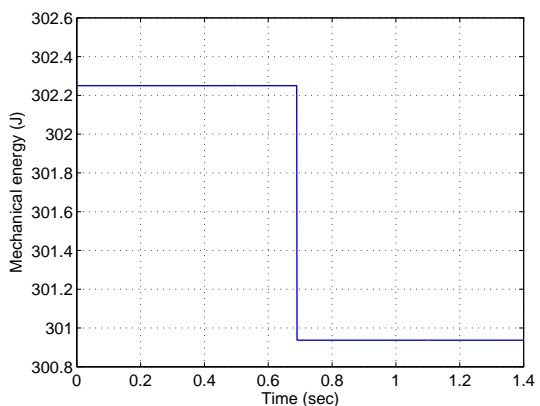
Figure 2.3: Time response.



(a) Potential energy



(b) Kinetic energy



(c) Total energy

Figure 2.4: Mechanical Energy During the Swing Stage.

For the mechanical energy, the potential energy is shown in Figure 2.4 (a), and (b) is the kinetic energy. The potential energy will decrease and convert to kinetic energy before the impact happens. At the moment of impact, the robot has the highest kinetic energy and lowest potential energy. After the impact, the kinetic energy will be converted to potential energy of the new swing leg, and decrease again then following the procedure mentioned above.

The potential energy and kinetic energy on Figure 2.4 (a) and (b) have the same contours comparing to [12, 13]. However, for biped robot, the sum of potential energy and kinetic energy do not keep constant during a swing stage, because there is another energy input, which is the power applied from the controller on torso. If the power from controller is considered, the total mechanical energy of biped robot with torso is also conserved as shown in Figure 2.4 (c). As mentioned in [2], the impact equations result in the dissipation and the contraction of phase fluid. Therefore, the total mechanical energy will suddenly drop to a new value after the impact as shown in Figure 2.4 (c).

From the preliminary results of the simulation, and comparison with previous researches, the simulation model is valid. In the following sections, this model is going to be utilized to analysis the motions of biped robot with torso as well as the influence of different parameters on the characteristics of the gait.

Chapter 3

Gait Motion and Stable Orbit

3.1 Steady Gait

The detailed motion of gait will be discussed in this section. The steady gait on Figure 2.2 (a) can be separated into two different phases as shown in Figure 3.1. The trajectory of gait moves clockwise. From the point 1 to 2, it's swing phase, which means this leg is free from ground and not a supported leg. Until the trajectory moves to 2, the occurrence of impact and the algebraic equation (2.8) leads to the angular velocity of the swing leg jump to point 3, and becomes a stance leg.

From point 3 to 4, the trajectory represents the motion of a stance leg. Until the trajectory moves to point 4, the swing leg contacts with the ground and the impact force leads the trajectory jumping to point 1 and the stance leg switches to swing leg again. Then the trajectory moves forward to another cycle.

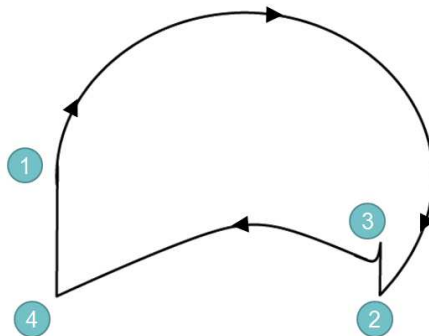


Figure 3.1: A typical limit cycle for the compass-like biped.

Figure 3.2 shows the motion of a biped robot with torso walking on a slope. The trajectory shown on Figure 3.1 is the leg of solid line in Figure 3.2. The red point means the contact between that foot and the ground. After the impact on point 1, the leg becomes swing leg and starts swinging forward. At the moment when the leg contacts the ground, point 2, both two legs contact with ground. And then the leg switches from swing leg to stance leg, in which a red point appears on the contact point between the leg and ground. Until another leg moves to contacts the ground, the leg switches back to be a swing leg after the point 4.

3.2 Motion of Torso

The motion of steady gait mentioned on the previous subsection are similar to biped robot without torso. The motion of torso is discussed, in this section. The motion of torso is different

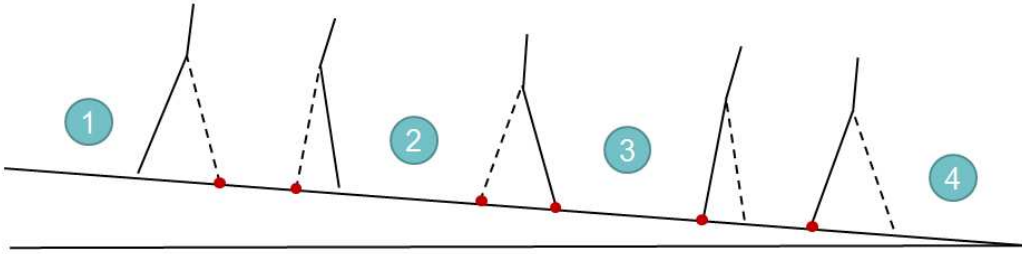


Figure 3.2: Steady gait on a slope in different phases.

if using different control law. The simple PD controller for torso, which has been used in [7, 8, 6], will be used in this project.

The motion of torso by PD controller is shown in Figure 3.3. The number of points in this figure are corresponding to the same points on Figure 3.1 and Figure 3.2. The motion of trajectory is clockwise. On a stable walking, the motions of torso in two sequential step have identical motion. On the comparison with Figure 3.2, the angular position will decrease and pass through the desired torso angle, while the swing leg located behind the stance leg. Until the swing leg overtakes the stance leg, the angular position of torso start increasing until the occurrence of impact. After the impact, the motion of torso will repeat again till the next impact.

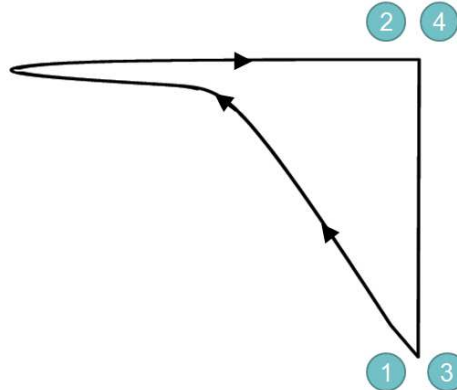


Figure 3.3: A typical limit cycle for the compass-like biped.

3.3 Definition of Characteristics

For the analysis of the biped robot with torso, there are some characteristics need to be defined first.

Step period: the gait period, defined by T , describes the period between the take-off of one foot from the ground and its subsequent landing.

Half leg angle: half leg angle, denoted by α , is the angle between both legs at the moment of impact, which is equal to the angular position of stance leg minus swing leg.

$$\alpha = \theta_1 - \theta_2$$

Step length: step length, L , is the distance between the tips of both leg in the moment of impact. It can be computed by

$$L = 2l\sin(\alpha)$$

Walking velocity: walking velocity, denoted by v , is defined by the moving velocity of the hip. The velocity is equal to step length divide by step period.

$$v = \frac{L}{T}$$

3.4 Stability of Poincaré Map

When considering the original nonlinear dynamic equations of the robot, the existence and the stability of passive gaits can no longer be investigated via analytical methods. Since the biped robot has periodic gaits, the idea of Poincaré map can be used. This project will refer to the method, using numerical simulations, in the report [4].

In this project, the Poincaré section has been chosen when the swing leg leaves the ground, which is the moment on point 1. The Poincaré map is denoted as F by

$$q_k = F(q_{k-1}) \quad (3.1)$$

Let q^* is the fixed point of the map. For a small perturbation δq^* around the limit cycle, the nonlinear mapping function F can be expressed in terms of Taylor series expansion by keeping only linear terms

$$F(q^* + \delta q^*) \approx F(q^*) + (\nabla F)\delta q^* \quad (3.2)$$

where ∇F is the gradient of F with respect to the state variables. Since q^* is a fixed point of the mapping, the equation (3.2) can be rewritten

$$F(q^* + \delta q^*) \approx q^* + (\nabla F)\delta q^* \quad (3.3)$$

The equation above can be rewritten by

$$(\nabla F)\delta q^* \approx F(q^* + \delta q^*) - q^* \quad (3.4)$$

where $F(q^* + \delta q^*)$ is the Poincaré map of the perturbed state $q^* + \delta q^*$. Since it is not practical to analytically calculate the matrix ∇F , it has to proceed by numerical simulation. The method is to perturb one state at a time by a small amount and observe its Poincaré map. Repeating this procedure at least six times (once for each of the six states), one equation can be obtained.

$$(\nabla F)\Upsilon = \Omega \quad (3.5)$$

where Υ is a 6×6 diagonal matrix that contains as its diagonal entries the perturbations of the state variables, δq_i^* . The Ω is a 6×6 matrix, whose i^{th} column is the difference from the fixed point to the first return states due to the perturbation of the i^{th} state variable. By assuming that Υ is nonsingular, ∇F can be computed by

$$\nabla F = \Omega \Upsilon^{-1} \quad (3.6)$$

The mapping F is stable if the Poincaré map of a perturbed state is closer to the fixed point. This property can be viewed as the contraction of the phase space around the limit cycle. Mathematically this means that the magnitude of the eigenvalues of ∇F at the fixed point q^* are strictly less than one.

Chapter 4

Parameter Study

The parameter study and analysis will be discussed in this section. In the following discussion, the parameters will keep the same as in Section 2.3 if there is no further definition. There are five different cases will be considered here. The variation in step period, half leg angle, walking velocity and step length related to the control parameter will be discussed as well.

4.1 Effect of Slope Angle with $\theta_3^d = -\psi$

The control parameter considered in the first case is the slope angle ψ while the desired torso angle is set by $\theta_3^d = -\psi$, which means the torso is vertical to the slope. The evaluation of gait characteristic under variation of slope angles are shown in Figure 4.1, and the different limit cycle are shown in Figure 4.2. In the simulation, it is found that the biped robot with torso can present stable symmetric gait for different scale of slope angle, approximately from 0.018 to 0.08 rad. As the slope angle increases, period-doubling bifurcation occurs in the gaits of biped robot with torso. It will be studied in the section afterward by the method, mentioned in Section 3.4.

Since the simulation results in [3, 4] using the same simulation parameters as in this project, except the presence of torso, the comparison between these two robot can assist to find out the influence of torso in the gait characteristics. The bifurcation point in the robot with torso is 0.08 rad, which is a little higher than the point in the robot without torso 4.37deg. Moreover, all the characteristics are higher in the case with torso than without torso. In Figure 4.2, the higher slope angle will cause higher kinetic energy before impact, thus the impact will result in a higher difference in velocity as shown in (a) steady gait as well as (b) torso trajectory.

The 2-period steady gait and torso trajectory are shown in Figure 4.3 at $\psi = 0.085$ rad. The symmetric limit cycle becomes asymmetric 2-period gait with a shorter and longer step. On further increasing the slope angle, the biped robot gait may experience chaotic gaits and torso trajectory, shown in Figure 4.4, where the slope angle is 0.096 rad.

4.2 Effect of Desired Torso Angle

In this section, the case that the slope angle is fixed to $\psi = 0.052$ rad with the desired torso angle as control is studied. The variation of gait characteristics as the desired torso angle increase from -0.291 rad to 0.25 rad are shown in Figure 4.5. The desired torso angle is vertical to the ground if it's zero. If the desired torso angle, θ_3^d , is negative, the torso inclines forward to the walking direction. And if θ_3^d is positive, the torso incline backward to the walking direction. It is obviously found out that only the step period is monotonic increasing. All the others three characteristics are monotonic decreasing, which means while the torso

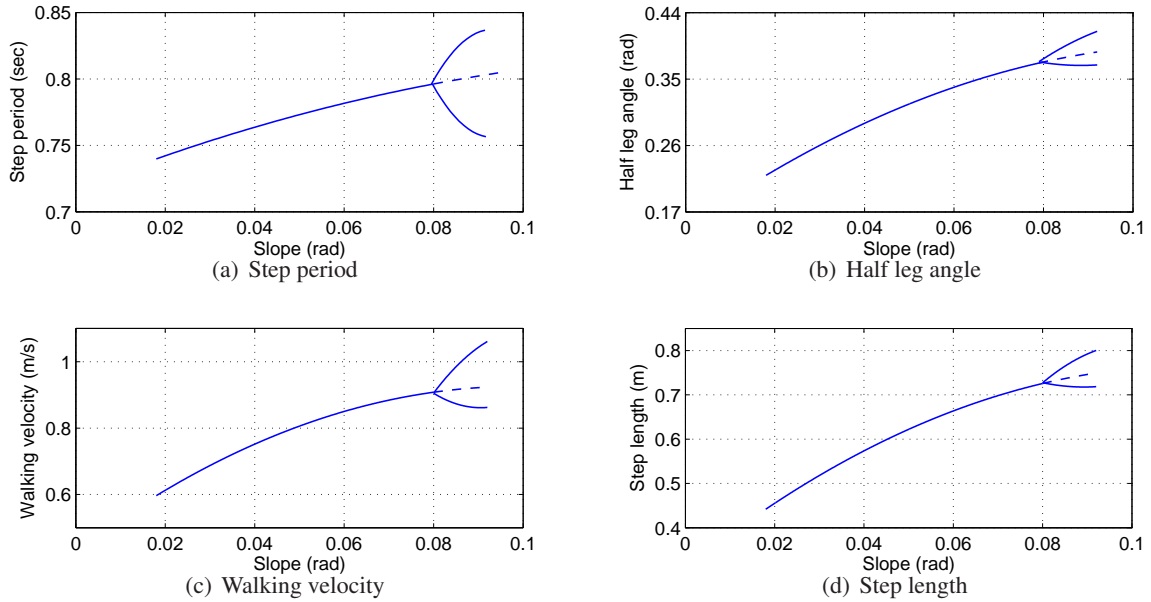


Figure 4.1: Bifurcation Diagram of Effect of Slope Angle with $\theta_3^d = -\psi$

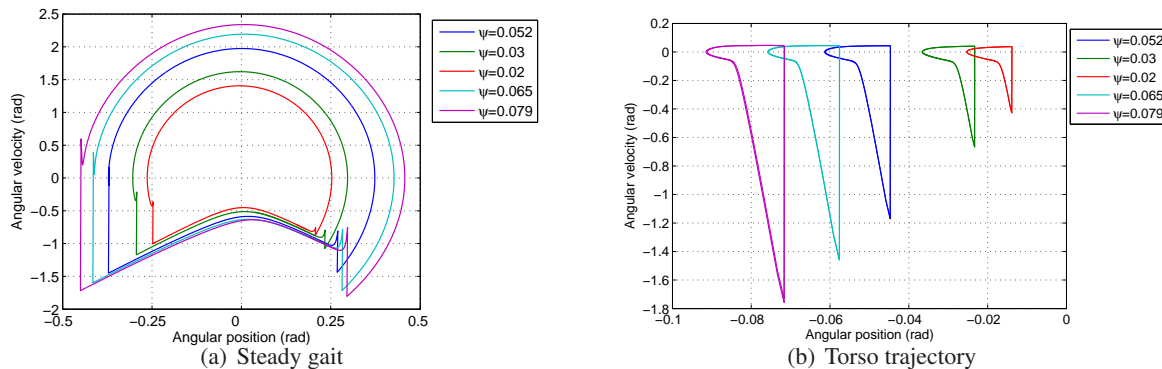


Figure 4.2: Gait and Torso Trajectory in Different Slopes.

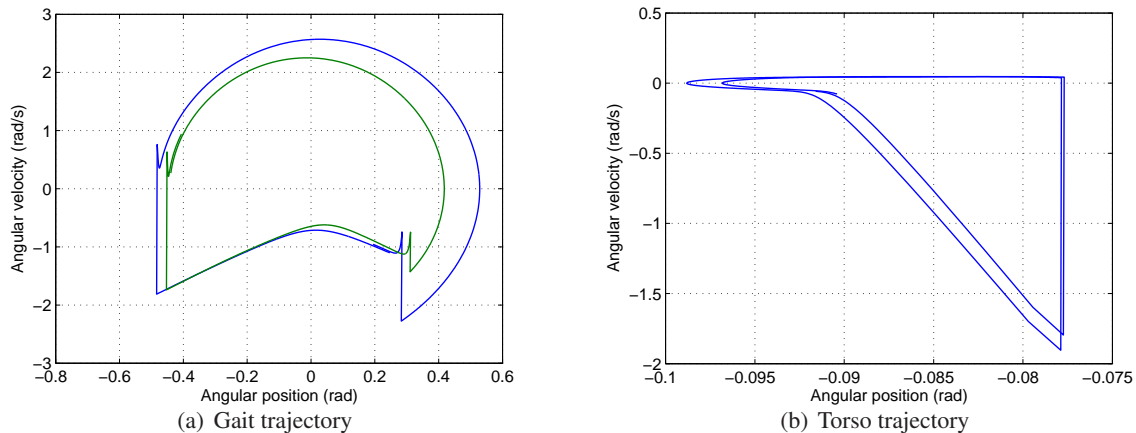


Figure 4.3: 2-periods Gait and Torso Trajectory, $\psi = 0.085$ rad.

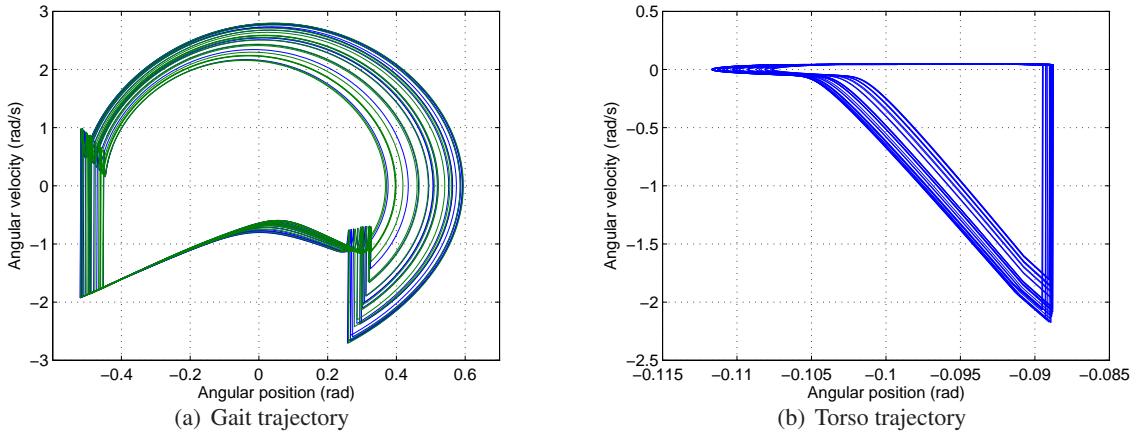


Figure 4.4: Chaotic Gait and Torso Trajectory, $\psi = 0.096$ rad.

incline forward, $\theta_3^d < 0$, the biped robot with torso will have higher half leg angle, walking velocity and step length in the same slope.

Figure 4.6 displays five different desired torso angles in this case. If the torso inclines forward, the robot has more energy to walk forward, so, the difference of angular velocity of torso during impact is higher than torso incline backward. Besides, if the torso incline backward with a higher angle, say 0.25rad, the gait becomes very small as well as the motion of torso. In this case, the highest desired torso angle while incline forward is -0.291 rad. If the absolute value of forward inclined torso angle is higher than the critical value, there is no stable gait.

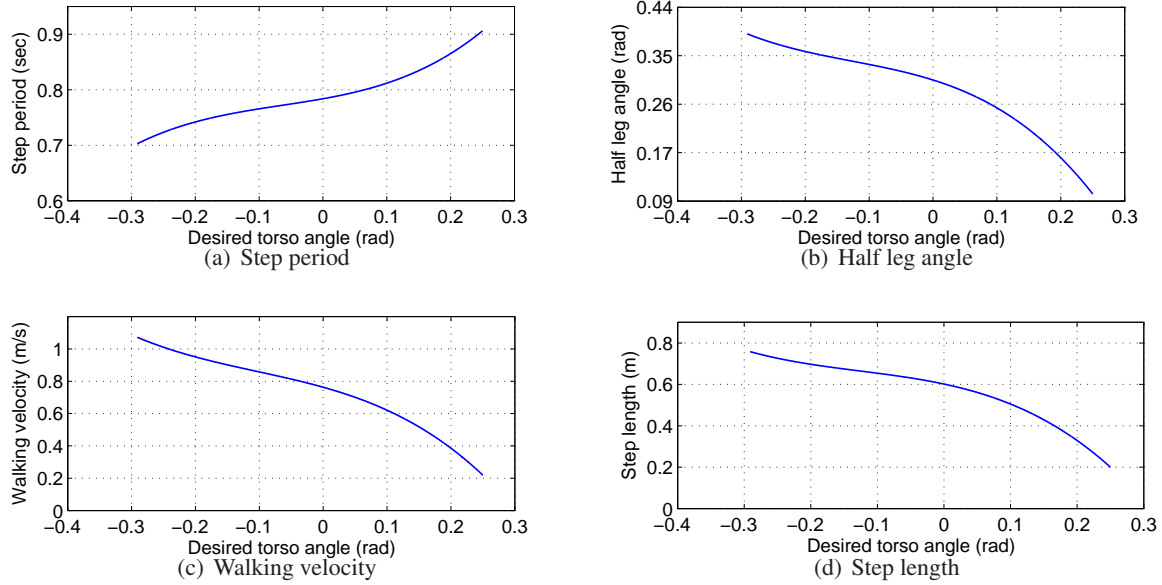


Figure 4.5: Bifurcation Diagram of Effect of Desired Torso Angle

4.3 Effect of Slope Angle with $\theta_3^d = \psi$

The case that torso inclines forward as the increasing of slope angle has been discussed in Section 4.1. In this section, the case that torso incline backward will be considered. The

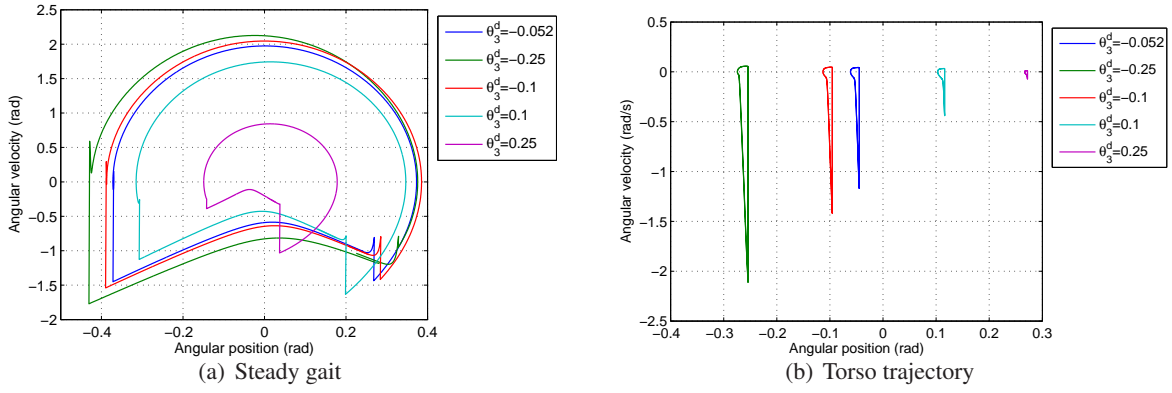


Figure 4.6: Gait and Torso Trajectory in Different Slopes.

control parameter is also the slope angle ψ . However, the desired torso angle for PD control changes to $\theta_3^d = \psi$, which means the torso is incline to the opposite of walking direction.

Figure 4.7 shows the bifurcation diagram in this case. The robot has steady one-period gait if the slope angle is less than 0.067 rad. The steady gait and torso trajectory in different slope angles are shown in Figure 4.8. It is the same that the higher the slope angle is, the higher the step length and the impact are. In comparison with the case that torso incline forward, the bifurcation point is earlier while torso inclines backward. On the slope angle equals to zero, which means walking on the level ground, the torque applied on torso will also be applied on stance leg that make the biped robot is capable to walk steady on level ground with a suitable initial conditions.

While the slope angle increases to a value higher than 0.067 rad, the period-doubling occurs. The figure of period-doubling is shown in Figure 4.9 as slope angle is 0.08 rad. The gaits become asymmetric with a longer and a shorter stable gait. If the slope angle keep increasing, say $\psi = 0.094$ rad, the phenomena of chaotic gait can be found and shown in Figure 4.10. There is no stable limit cycle can be found in chaotic gait.

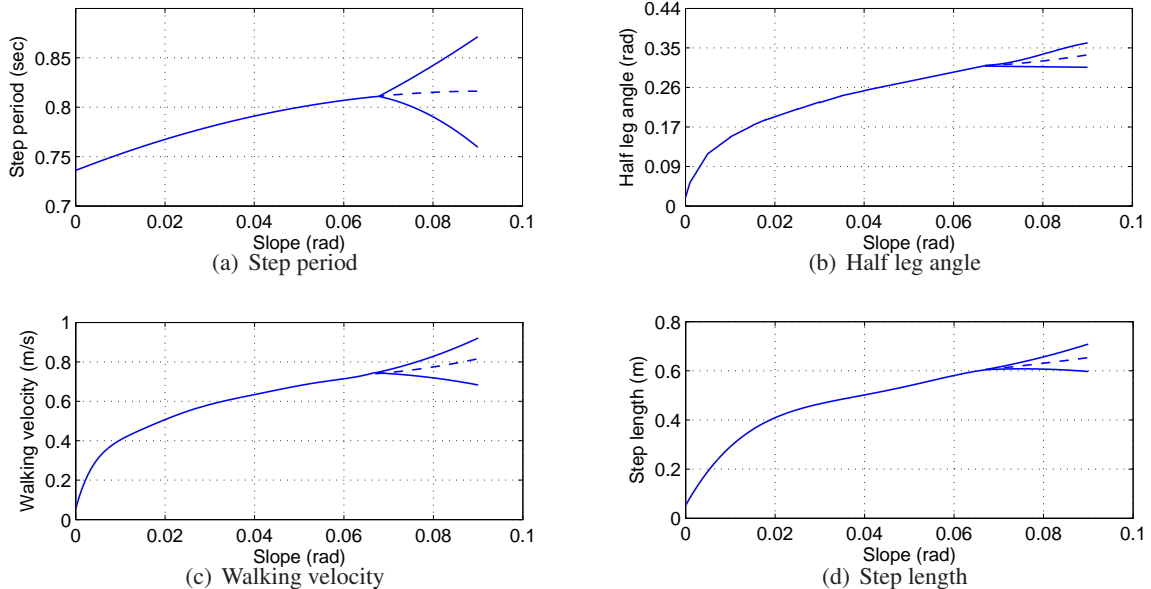


Figure 4.7: Bifurcation Diagram of Effect of Slope Angle with $\theta_3^d = \psi$

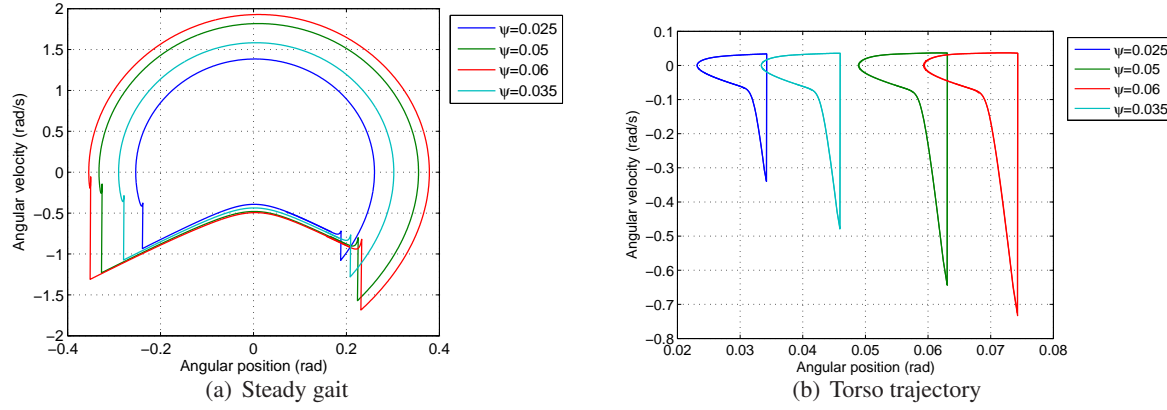


Figure 4.8: Gait and Torso Trajectory in Different Slopes.

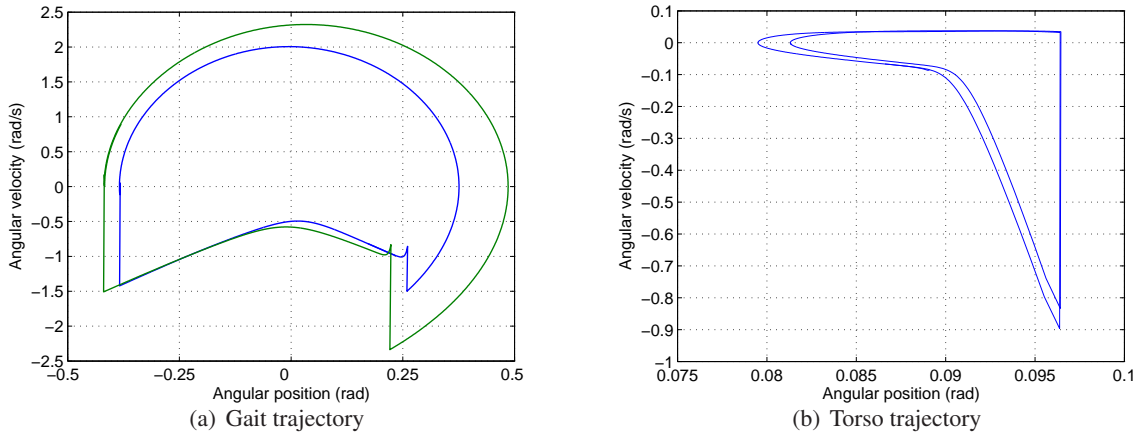


Figure 4.9: 2-periods Gait and Torso Trajectory, $\psi = 0.08$ rad.

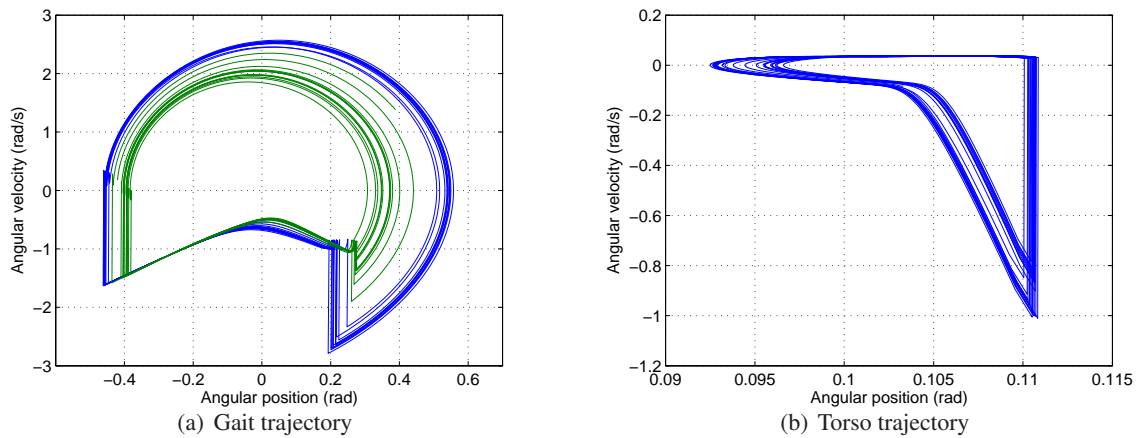


Figure 4.10: Chaotic Gait and Torso Trajectory, $\psi = 0.094$ rad.

4.4 Effect of Slope Angle with $\theta_3^d = -0.291$ rad

In Section 4.2, while the slope angle is 0.052, there is no stable gait can be found if the forward inclined torso angle is larger than 0.291 rad. In this section, the situation, whether the robot has stable gait or not while the increasing of slope angle with a higher forward inclined torso angle, will be studied. Therefore, in this case, the desired torso angle is fixed to -0.291 rad, and the control parameter is the slope angle, which is increasing from 0.052 to the occurrence of chaotic gait.

Figure 4.11 shows the bifurcation diagram of this case, and Figure 4.12 shows the steady gait and torso trajectory in different slope angle. The same as in the previous section, the increasing of slope angle will also increase the value of four different characteristics. The bifurcation point here is higher than the previous case, which means if the torso forward incline in a higher angle, the robot can stand in higher slope angle without the occurrence of period-doubling. In the comparison with the case no matter $\theta_3^d = -\psi$, or $\theta_3^d = \psi$, higher torso angle has higher half leg angle, walking velocity and step length but shorter step period in the same slope angle.

The period-doubling gait and torso trajectory are shown in Figure 4.13, while $\psi = 0.09$ rad, and the chaotic gait and torso motion are shown in Figure 4.14, while $\psi = 0.095$ rad.

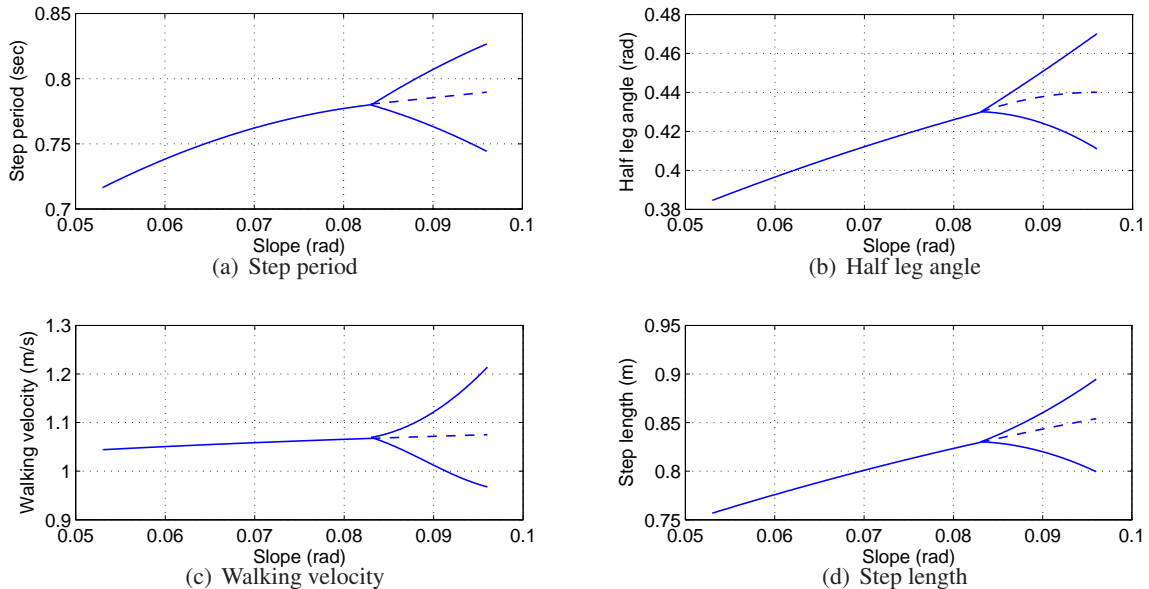


Figure 4.11: Bifurcation Diagram of Effect of Slope Angle with $\theta_3^d = -0.291$ rad

4.5 Effect of Torso Length

The last case discussed in the project is the influence of torso length on the characteristics of biped robot with torso. The control parameter is the length of torso. Figure 4.15 shows the variation of step period, half leg angle, walking velocity and step length with the change of torso length. The results here are similar to the case that changing desired torso angle in Section 4.2. The step period is the only characteristic that is decreasing while the torso length increases. The other three characteristics are all increasing with the length of torso. The stable gait and torso trajectory in different torso length are shown in Figure 4.16. The less the torso length is, the smaller the sway of torso and the higher the impact are. There is no period-doubling bifurcation as well as chaotic gait in this case.

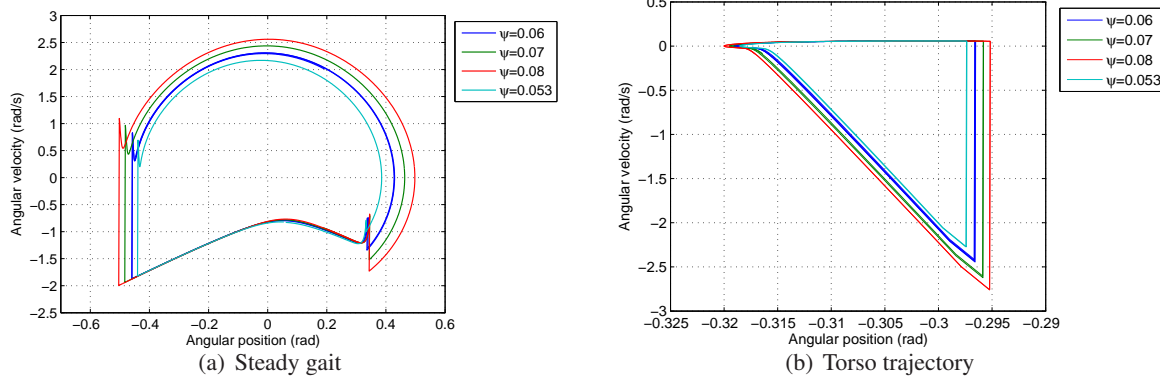


Figure 4.12: Gait and Torso Trajectory in Different Slopes.

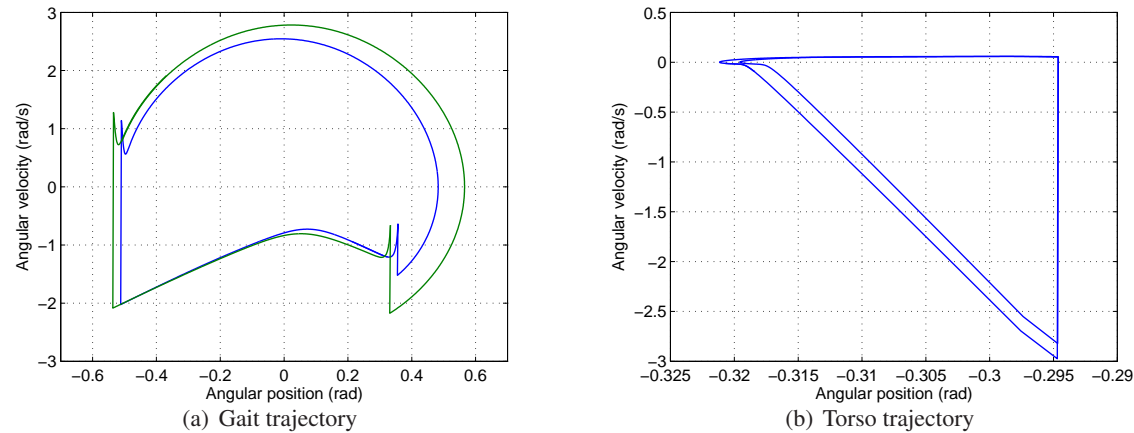


Figure 4.13: 2-periods Gait and Torso Trajectory, $\psi = 0.90$ rad.

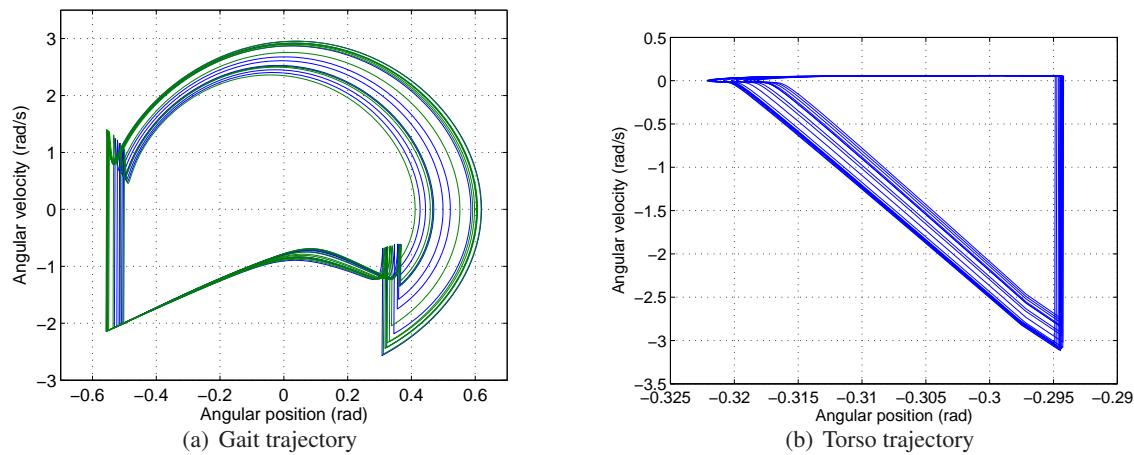


Figure 4.14: Chaotic Gait and Torso Trajectory, $\psi = 0.095$ rad.

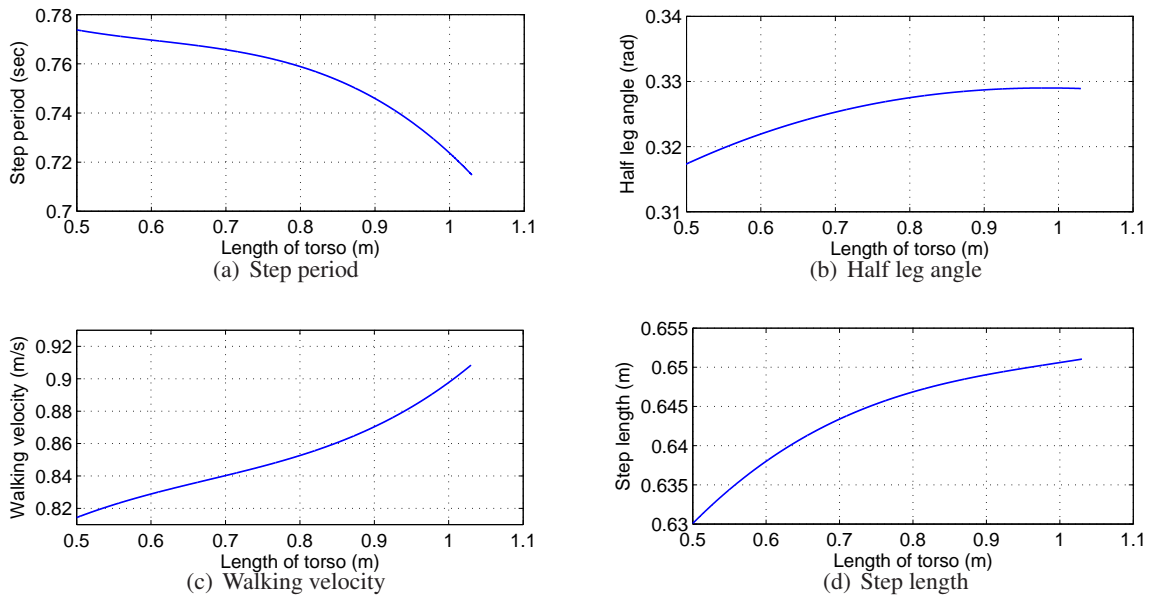


Figure 4.15: Bifurcation Diagram of Effect of Torso Length.

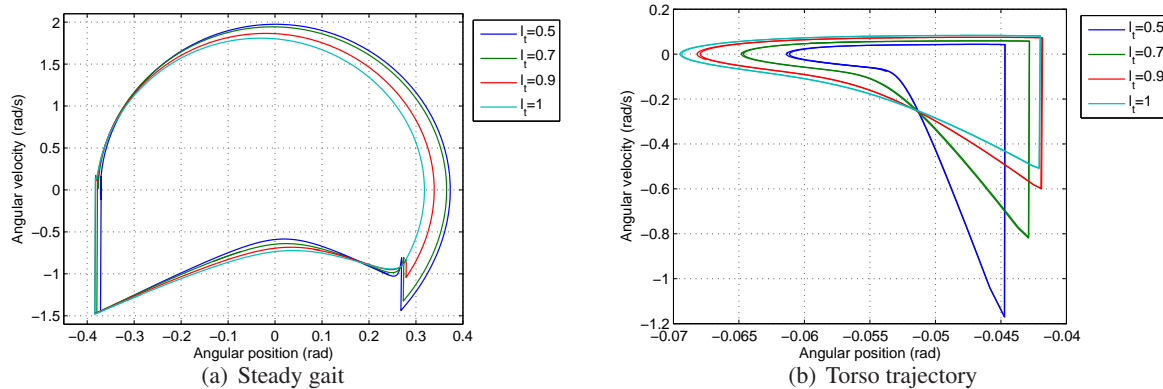


Figure 4.16: Gait and Torso Trajectory in Different Slopes.

4.6 Period-doubling Bifurcation

The occurrence of period-doubling bifurcation can be studied by the method mentioned in Section 3.4. Among the five cases discussed in this chapter, there are three cases, which are Effect of Slope Angle with $\theta_3^d = -\psi$ in Section 4.1, Effect of Slope Angle with $\theta_3^d = \psi$ in Section 4.3, and Effect of Slope Angle with $\theta_3^d = -0.291$ rad in Section 4.4, have period-doubling bifurcation. By the method mentioned in Section 3.4, the stable fixed point will be perturbed in all six states individually. By the utilization of numerical simulation, the difference between fixed point and the first return map with perturbation can be used to construct the matrix Ω . By the equation (3.6), where the Υ is a matrix whose diagonal term is the value of perturbation, the gradient of F can be obtained as well as the eigenvalues of ∇F .

Take the case that $\theta_3^d = -\psi$ while $\psi = 0.079$ as an example. The fixed point on Poincaré Map is

$$q = \{0.2904, -0.4444, -0.0707\} , \quad \dot{q} = \{-0.7584, 0.5738, -1.7029\}$$

On the discussion here, the fixed point on Poincaré Map has dimension 6, which does not match the need that Poincaré Map has dimension less than 6. However, since the Poincaré section has been chosen when the swing leg leaves the ground, which mean the sum of stance angle and swing angle will equal to negative of twice the slope angle.

$$\theta_1 + \theta_2 = -2\psi$$

If consider the relation between stance angle and swing angle, the Poincaré section has only 5 dimension, which is less than 6. Nevertheless, in this section, all the six states will be considered to follow the method mentioned on Section 3.4.

After six simulations of the first return map on perturbed all state individually, the eigenvalues of ∇F are

$$\begin{aligned} & -0.8300 + 0.5039i , \quad -0.8300 - 0.5039i \\ & -0.1594 , \quad -0.0019 \\ & 0.0724 + 0.0124i , \quad 0.0724 - 0.0124i \end{aligned} \tag{4.1}$$

The absolute value of the highest eigenvalue is 0.97, which is inside a unit circle, so this is not a bifurcation point.

Following the same method for all the three cases, the maximum absolute value of eigenvalues for each case are shown in Figure 4.17. Figure 4.17 (a) is the case in Section 4.1, the bifurcation point occurs while slope angle equal to 0.08. The eigenvalues of Section 4.3 is shown in Figure 4.17 (b), where the bifurcation point occurs at around 0.067 rad. And the last case that the effect of slope angle with $\theta_3^d = -0.291$ rad is in Figure 4.17 (c) with bifurcation point at around 0.0837 rad.

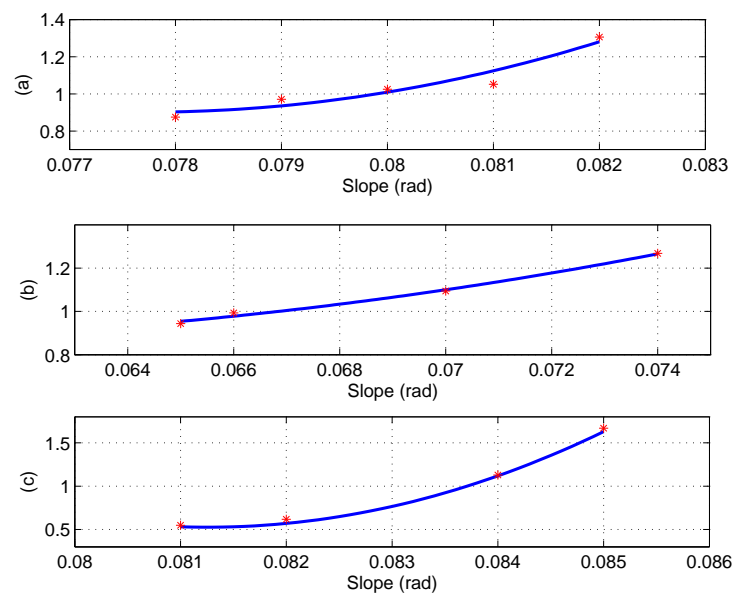


Figure 4.17: Eigenvalue.

Chapter 5

Conclusions and Further Works

Biped robot is superior to other robots because it is potentially suited to hazardous environments, such as moving on unpaved terrains. However, the most crucial issue that obstructs the application of walking robot is the lack of energy efficiency. In order to provide an efficient and broadly-used biped robot, the research on passive or passivity-based walking robot is important. The objective is to minimize the required energy in order to develop a biped walking robot that can walk on different slopes, terrains as well as ascending and descending the stairs in different walking speed, step period, and step length.

In this project, the parameter analysis on biped robot with torso by simple PD controller is studied. Using numerical simulation, the variation of the gait characteristic with different parameters is discussed. From the simulation results and discussion of project, the bifurcation only occurs in the cases that the control parameter is slope angle. It means that a higher slope angle will result in the phenomena of bifurcation. However, using other parameters as the control parameter, say desired torso angle θ_3^d or torso length l , only unstable gait can be observed if the control parameter is increasing instead of period-doubling bifurcation.

In the comparison between these five cases, the forward inclining torso will cause period-doubling bifurcation in a lower slope angle. Moreover, if the torso inclines forward with a larger angle, the biped robot can walk on a steeper slope than other cases. In addition, the length of torso and the desired torso angle can be utilized to control the biped robot on different gait characteristics. Therefore, the biped robot with torso can walk on the same slope angle in different walking velocity, step period, and step length by only control the angle of torso. Furthermore, if the biped robot wants to walk on a steeper slope, the torso can be controlled to incline forward, then the robot can still have stable symmetric gait.

Although this project studied some parameters that influence the gait characteristic, there are some other parameters that will influence the behavior of biped robot with torso, such as the mass of torso, and gain of controller. Moreover, the biped robot with torso has been verified that it is capable to walk on level ground. Thus, the study on different parameters, and the control on walking on level grounds and uphill should be studied in the near future. In order to make the robot more like human, for instance kneed biped robot with torso or kneed biped robot with ankles, the study of walking robot with applicable passivity-based should also be discussed in the future.

Bibliography

- [1] V. F. H. Chen. Passive dynamic walking with knees: A point foot model. Master thesis, Massachusetts Institute of Technology, Feb. 2007.
- [2] A. Goswami, B. Espiau, and A. Keramane. Limit cycles in a passive compass gait biped and passivity-mimicking control laws. *Autonomous Robots*, 4(3):273–286, 1997.
- [3] A. Goswami, B. Thuilot, and G. Espiau. A study of the passive gait of a compass-like biped robot: Symmetry and chaos. *International Journal of Robotics Research*, 17(12):1282–1301, 1998.
- [4] A. Goswami, B. Tuillot, and B. Espiau. Compass-like biped robot, part i: Stability and bifurcation of passive gaits. Research report, INTRIA, 1996.
- [5] J. W. Grizzle, G. Abba, and F. Plestan. Asymptotically stable walking for biped robot: Analysis via systems with impulse effects. *IEEE Transactions on Automatic Control*, 46(1):51–64, Jan. 2001.
- [6] J. K. Holm, D. Lee, and M. W. Spong. Time-scaling trajectories of passive-dynamic bipedal robots. In *IEEE International Conference on Robotics and Automation*, pages 3603–3608, Apr. 2007.
- [7] N. Khraief, N.K. M’Sirdi, and M.W. Spong. Nearly passive dynamic walking of a biped robot. In *European Control Conference*, 2003.
- [8] T. Narukawa, M. Takahashi, and K. Yoshida. Biped locomotion on level ground by torso and swing-leg control based on passive-dynamic walking. In *IEEE/RSJ International Conference on Intelligent Robots and Systems*, 2005.
- [9] M. W. Spong. Passivity based control of the compass gait biped. In *IFCA Truennial World Congress*, Jul. 1999.
- [10] W. M. Spong, J. K. Holm, and D. Lee. Passivity-based control of bipedal locomotion. *IEEE Robotics and Automation Magazine*, 14(2):30–40, Jun. 2007.
- [11] M. Wisse, A. L. Schwab, and F. C. T. van der Helm. Passive dynamic walking model with upper body. *Robotica*, 22(6):681–688, Nov. 2004.
- [12] P. Zhang, Y. Tian, and Z. Liu. Gait analysis of the passive dynamic walker with knees. In *First International Conference on Intelligent Robotics and Applications*, pages 992–1002, Oct. 2008.
- [13] P. Zhang, Y. Tian, Z. Liu, S. Yang, and R. Tian. Further research and comparison of gaits for compass-like biped and kneeled passive dynamic walker. In *First International Conference on Intelligent Robotics and Applications*, pages 1216–1226, Oct. 2008.